WARSAW UNIVERSITY OF TECHNOLOGY

Automatic Control, Electonics, Electrical Engineering and Space

Technologies

Engineering and Technology

Ph.D. Thesis

Athanasia Papanikolaou, M. Sc.

Portable Multimodal System for Measurement and Monitoring of Cultural Heritage Objects

Supervisor

Prof. Malgorzata Kujawinska, Ph.D., D.Sc. Eng.

WARSAW 2023

Acknowledgements

I would like to express my gratitude to all the people who supported me during the years of my PhD journey. First and foremost, I would like to express my deepest gratitude to my supervisor, Małgorzata Kujawińska for her guidance, dedication, and unwavering support during these years. I would also like to thank my co-supervisors, Prof. Sony George and Prof. Elizabeth E. Peackock from NTNU, as well as from Prof. Jacek Martusewicz from AFAW, for their suggestions, and encouragement, and assistance.

My sincerest gratitude to the Mechatronics Department academic and administration members for creating a favourable daily working environment and always being welcome to assist me with any difficulties, especially to Prof. R. Sitnik and Prof. M. Jozwik. I would also like to express my appreciation to M. Adamczyk for his vital role in the mechanical design of the developed device; the company SMARTTECH 3D, and A. Gebarska, for their guidance during the metrological evaluation stage and granting me access to their products. Additionally, I would like to express my appreciation to Prof. S. George, Prof. G. Trumpy and Prof. A. Suneel Sole, for their support in the development of the spectral imaging modality and the Colourlab members of NTNU for their warm welcome and assistance during my research stays in Norway. I would also like to thank Dzik-Kruszelnicka, L. Malkowska, and D. Kuakowska from AFAW for the excellent collaboration and providing their knowledge and objects for my research. Sincere acknowledgement also goes to every member of CHANGE program for providing me with a collaborative platform, networking opportunities, and the early researchers of the CHANGE project for their friendship and support.

Aside from academics, I want to thank my friends and family for their constant support and presence in my life. A big thank you to Stauros, Eirini, Evaggelia, Korina, Marina, and Vaggelis for their constant support in every possible way. Furthermore, I want to thank the friends I made during this journey, Sunita, Yash and Shashank, whose company made my stay in Warsaw unforgettable. Finally, I want to thank my partner, Charalampos, and my mother, Maria, for their endless love, support and encouragement through this journey's ups and downs.

Dedicated to...

my Mother, Maria,

for being a constant source of inspiration and role model throughout my life

Streszczenie

Głównym celem niniejszej pracy jest opracowanie metod i przenośnej aparatury naukowej do pomiaru obiektów dziedzictwa kulturowego (ODK) i monitorowania ich zmian wywołanych czynnikami zewnętrznymi. ODK, zgodnie z rekomendacjami konserwatorów, wymagają zastosowania technik nieinwazyjnych i często dających informację w całym polu widzenia. Wstępna implementacja wybranych polowych, optycznych metod pomiarowych wykazała ich przydatność badań ODK. W tym kontekście, zaproponowano połączenie trzech metod wykorzystujących światło niekoherentne i umożliwiających wyznaczanie kształtu (metoda światła strukturalnego, MS), pomiar przemieszczeń w płaszczyźnie, i pozapłaszczyznowych oraz odkształceń (trójwymiarowa metoda cyfrowej korelacji obrazu, 3D CKO) oraz barwy (obrazowanie wielospektralne). W ramach rozwoju i dostosowania tych metod do wymagań ODK zmodyfikowano barwną metodę 3D CKO (bCKO), tak, aby umożliwiała pomiary z wykorzystaniem naturalnej tekstury obiektu. W szczególności przeanalizowano wybrane metody demozaikowania barwnych obrazów pod kątem dokładności pomiarów przemieszczeń. Opracowano również uproszczony system obrazowania wielospektralnego (wS) poprzez zwielokrotnienie czułości spektralnej kanałów RGB kamer i widmowego rozkładu mocy oświetlenia projektora. Metoda umożliwia pomiar barwy w 5 dyskretnych pasmach spektralnych w zakresie 400-620 nm. Dla metod bCKO i wS opracowano specjalne scenariusze pomiarowe, które przetestowano na przykładzie analiz pergaminów historycznych i obrazów olejnych. Wdrożono metodę światła strukturalnego z wykorzystaniem projektora cyfrowego i dwóch kamer, zapewniając dokładne rejestrowanie kształtu (chmury punktów współrzędnych powierzchni) obiektu trójwymiarowego. W następnym etapie pracy zaprojektowano i zbudowano przenośny system optomechatroniczny wykorzystujący cyfrowy projektor i 2 barwne kamery, które umożliwiają pozyskanie danych pomiarowych dla wszystkich trzech modalności.

Opracowano zintegrowane procedury kalibracji systemu multimodalnego i metodę fuzji danych do jednego układu współrzędnych. Dla każdej modalności i dowolnych ich kombinacji zostały opracowane przykłady ścieżek pomiarowych oraz przetwarzania i analizy danych. Pełną funkcjonalność systemu zaprezentowano na przykładzie pomiarów i monitorowania historycznego pergaminu oraz makiety obrazu olejnego z defektami poddanych wpływom zmiennej wilgotności (współpraca z Akademią Sztuk Pięknych w Warszawie). System umożliwia szybkie, nieniszczące i ekonomiczne pozyskiwanie multimodalnych danych o ODK służących do archiwizacji, monitorowania zmian w tych obiektach i projektowania prac konserwatorskich.

Słowa Kluczowe: b adania obiektów dziedzictwa kulturowego, metrologia optyczna, przetwarzanie danych obrazowych 2D i 3D, cyfrowa korelacja obrazu, metoda światła strukturalnego, obrazowanie multispektralne; obrazowanie multimodalne

Abstract

The main objective of this thesis is the development of methods and portable scientific instrumentation for measuring and monitoring of cultural heritage objects (CHOs) exposed to external loadings. CHOs, according to conservation recommendations, require noninvasive techniques. Initial implementations of the selected full-field optical measurement methods have indicated their high suitability for CHOs investigations. Within this framework, a combination of three incoherent imaging techniques have been proposed, namely Structured Light method (SL) for 3D shape determination, 3D Digital Image Correlation (3D DIC) for in plane, out of plane material investigations. As part of development and adaptation of these methods to CHOs requirements, the colour 3D DIC method (cDIC) was modified to enable the measurements based on a natural, colour CHOs texture. In particular a wide range of image demosaicking methods have been tested and evaluated with respect to the displacements accuracy. Also, a simplified MSI system has been developed by multiplexing the RGB camera channels sensitivities and the projector spectral power distribution. The spectral system consists of five discrete bands across the visible wavelength spectrum of 400-620nm. For cDIC and MS methods special measurement scenarios were developed and tested by examples of a historical parchment and paintings on canvas investigations. The structured light method with two cameras was also implemented for high accuracy registration of 3D CHOs shape (cloud of points (x,y,z)). At the next stage of work a portable opotmechatronics system has been designed and built. It is based on a digital light projector and two colour cameras, which enable capturing data for all three modalities. The integrated procedures for multimodal system calibration and data fusion in a common co-ordinate system were developed. Example measurement and data processing pipelines were presented for each modality and their arbitrary combinations. The full functionality of the system was presented by example

of measurements and monitoring of a historical parchment and painting mock-ups with defects exposed to humidity. The system enables a quick, non-invasive, non-destructive and low cost way to capture multimodal data for documentation, monitoring of 3D CHOs and planning conservation works.

Keywords: C ultural Heritage Objects; Full-field optical metrology; 2D and 3D data processing; Digital Image Correlation; Structured Light; 3D colour Digital Image Correlation; Multispectral Imaging; Multimodal Imaging

Contents

1

Introduction

1.1 Background

Cultural heritage objects (CHOs) undergo continuous changes and deterioration over time. In order to preserve them for future generations, it is essential to monitor, evaluate, and comprehend these changes as precisely as possible without damaging their surface. Therefore, methodologies that allow for the impartial assessment of changes in CHOs are necessary and can impact the cultural appreciation of the objects and their long-term preservation. Such methods can assist conservators in planning essential treatments and preventing certain stages of degradation. Change in CH objects can be caused by various factors that impact locally or globally the materials, and therefore they result in complicated physicochemical and structural processes. It is generally accepted that such changes are unavoidable and they need to be identified, measured, quantified, and monitored. This can be challenging as it requires developing and deploying innovative measurement instrumentation and methodologies or adapting the existing tools for CHOs' needs. Recently, the most popular methods are

optical, machine-vision based approaches which allow for nondestructive, quick and simple capture of CHOs' images in digital form, followed by archiving and/or analysis of an entire object (full-field methods). Recent advancement in high-resolution imaging technology (CCD/CMOS cameras), combined with the state-of-the-art data analysis, has made the accurate detection of CHOs' changes in shape, displacements/strains, reflectivity in the function of wavelength (colour) possible. Due to their non-contact and non-invasive character, they are indispensable tools for characterising materials, detecting degradation, condition assessment, and digitising and monitoring the objects response and processes through time.

Extensive digital documentation of CHOs using imaging methods has started at the end of the 20^{th} century [1, 2, 3, 4], especially in digitization and geometrical surface reconstruction with high precision and accuracy. Good documentation provides valuable information for researchers, curators, or conservators and can be vital for the future preservation of the object. However it is crucial to select a correct optical measurement method (in respect to spatial and temporal resolution, accuracy, measurement range) for an identified task. Researchers can choose among multiplicity of optical measurement methods based on coherent (lasers) and incoherent light sources. Coherent light methods (CLM) based on interferometry including holographic and speckle interferometry as well as shearography are mainly applied for highly sensitive nondestructive testing of paintings and sculptures [5, 6]. Other methods using lasers include: Terahertz imaging [7], optical coherence tomography [8, 9, 10] , IR thermography [11], photoacoustic imaging [12, 13] and laser scanning [14, 15]. These methods aim at structural in-depth analysis of the artwork or the retrieval of its three-dimensional shape [16, 4] and most of them require sophisticated equipment. Incoherent light methods (ILMs) are in general more widespread in CH documentation, preservation and conservation applications. ILMs includes all kinds of technical photography [17], multi- and hyper-spectral imaging [18, 19], photogrammetry [4, 20, 21, 22], 3D shape retrieval (structured light) [4, 23, 24, 25, 26, 27], reflectance transformation imaging [3, 28, 29], bidirectional reflectance distribution function imaging [30] and digital image correlation [31]. They often employ low-cost hardware (comparative to coherent light methods), require less stabilized conditions (when compared to interferometric methods), have flexible acquisition parameters (typically a Field-of-View (FoV) and recording settings are user determined), and require less specialized knowledge from an operator (minimal hazard). All these features make ILMs practical tools in hands of conservation scientists [32] for mul-

tiplicity of tasks including: documenting sequential stages of conservation, characterising materials, detecting degradation, condition assessment, and digitising and monitoring the objects response and processes through time. These are the reasons why in my work I focus on the solutions based on ILMs which provide quantitative imaging of CHO's surface and its changes. It should be mentioned that the problem of full-field monitoring of CHOs' changes is not well addressed through the commercial offer of measurement instrumentation. Currently a significant challenge is to link the retrieved shape and appearance of an object with other important data such as reflectance, displacements/deformation, strains [33, 34], that can provide vital information on the nature of the materials and their change over time. Therefore, there is a need to collect precise information on multiple quantities to understand the mechanisms leading to degradation. A common practice is to apply multiple complementary imaging modalities during various stages of conservation, depending on the measurement objectives. The simplest form of multisensory acquisition comprises data recorded using multiple methodologies and equipment, meaning that the datasets span across different types and contexts (e.g. 3D shape, Reflectance Transformation Imaging, Hyperspectral Imaging). This way, acquiring multimodal data by utilizing already existing individual setups is possible. However, post-processing registration methods are required to integrate and fuse the data with values of different scales and distributions into a common global world co-ordinates [35, 36]. This option offers the highest resolution for each independent modality, but also integrates registration and interpolation errors and practical restrictions associated with the measurement itself. The need for integrating heterogeneous information of the object's conservation condition within a spatially referenced 3D information system is discussed across multiple research articles [37, 38, 39, 40]. In other words, multimodal information must be subjected to data fusion to gain spatial coherence. Manual data integration is also a possibility, but time-consuming and includes multiple error sources that compromise the achievable resolution; hence, hardware solutions for multimodal measurements are required, or automatic methods based on image processing need to be developed. Other restrictions related to using individual modalities are transferring the object into multiple locations for the data recording or transferring multiple devices in situ. Both of these scenarios can be facilitated in the case of CH artefacts with significant value but can be impractical for everyday conservation practices.

1.2 Motivation

As discussed in the previous section it is clear that there is a need for portable, non-contact and non-invasive imaging set-up that conservators and conservation scientists can utilise for multimodal, quantitative imaging and structural health monitoring of CHOs. Recording information using a single imaging modality cannot provide all necessary information about the object's condition, while the study of changes in the structural integrity of CH artefacts has not been adequately addressed so far. Keeping these in mind, the motivation behind this work lies in providing multimodal approach for both the acquisition and processing of imaging data delivered by a relatively low-cost measurement device that can be used in situ. The selected modalities should be able to record the 3D shape and spectral (reflectivity) information as well as monitor in full field of view displacements and strains through measurement sessions distributed in time. Along these lines, a methodology should be also proposed to assess and monitor changes that selected groups of CHOs face during their exposure to environmental changes or conservation treatments. What's important, the methodologies must fulfill all specific requirements related to interaction with cultural heritage objects. In particular no modifications of an object surface/texture is allowed. In this work the selected CHOs include paintings on canvas and parchments, as the examples which are very sensitive to the very common environmental variations such as relative humidity and temperature. Following the outcome verification, the change detection task from surfaces is accompanied by many challenges. The following are the three highlighted particular challenges:

Challenge 1: Low cost, portable measurement system (PMS) which delivers three modalities: shape, displacements and reflectance

Currently there is no portable, multimodal imaging system (MIS) that integrates measurement of shape, structural integrity in terms of displacements and strains and reflectance information for the measurement and monitoring of CHOs. To meet the requirements of low cost and portability, the multimodal system should combine machine vision based methods. Also the data delivered for all three modalities should be provided in a common coordinate system, so that the information can be easily correlated and interpreted.

Challenge 2: Full-field displacements and strains measurement of objects with natural texture

The method for displacement and strain measurement, which can meet Challenge 1 is 3D digital image correlation (3D DIC). However traditional realization of 3D DIC measurement requires the presence of a random pattern (speckle) at an object's surface. Such treatment is prohibited for CHOs, therefore substantial modification of 3D DIC is required to allow measurements of objects based on their natural texture.

Challenge 3: Reflectance measurements with portable multimodal system

There are multiple systems which perform measurements of CHOs reflectance in the function of wavelength. Most of them (multispectral and hyperspectral cameras) rely on spectrometric measurements and therefore are costly devices. They also cannot be directly integrated into the PMS (as defined in Challenge 1). Therefore a method which simultaneously fulfills metrology requirements at least for a few selected wavelengths and use the equipment available in the PMS should be proposed and implemented.

1.3 Objectives of the thesis

The main scientific objective of this thesis is the development of a portable and low cost multimodal quantitative imaging device for surface measurement and monitoring of changes in CHOs. The objective of the work is broken down into three subsequent goals, each of which is briefly detailed below:

Obj. 1: Development of portable multimodal imaging system

This objective address the first challenge and it is focused on the development a functional, relatively low cost demonstrator of multimodal, quantitative imaging system. The demonstrator to be developed should have the capability of recording data for determination of (1) 3D shape, (2) reflectivity (for selected wavelengths), (3) displacements and strains. The CHOs under consideration have scattering or quasi-scattering surfaces. The results of measurements provided by the three modalities have to be spatially and temporally coherent for every captured instance.The assumed imaging modalities are : the structured light method (SL for shape), three-dimensional digital image correlation (3D DIC for 3D displacements and strains) and multispectral imaging (MSI for reflectivity). They should

be integrated into a single, multimodal imaging system, which requires appropriate utilization of hardware as well as development of data recording, processing and merging processing paths in order to provide all results in a common coordinate system. To assure low cost of MIS it is assumed that the main hardware will include two colour CMOS cameras, a digital light projector and a computer.

Obj. 2: Modification of 3D DIC method to assure measurement of objects with natural texture and its metrological assessment

This objective addresses the second challenge and aims on such modification of 3D DIC method that it provides displacement measurements based on a natural texture of CHO. It is assumed (in agreement with the 1^{st} objective) that images will be captured by colour cameras and 3D DIC will utilize data available, after demosaicking, in all three colour channels (R,G,B). The modified 3D colour DIC (3D cDIC) should significantly extend the range of CHOs, which displacements can be measured utilizing their natural texture. However the accuracy of 3D cDIC may be strongly dependent on the proposed colour image preprocessing (demosaicking procedures). For this reason, the modified 3D cDIC method has to be metrologically tested and the most efficient colour images processing paths have to be determined.

Obj. 3: Development of simplified measurement method of CHOs' spectral reflectance in MIS

Having decided for low cost hardware configuration (Objective 1) of MIS, it is necessary to propose a simplified approach to measurement of CHOs spectral reflectance. We assume that for initial (out-of laboratory) documentation it is sufficient to capture information about the actual CHO's reflectance just for a few selected wavelengths, however we also require that this information should be as accurate as possible and that the changes in this reflectance can be monitored. The new method will be utilizing colour cameras and digital light projector supported by proper spectral calibration procedures.

Obj. 4: Measurement and monitoring of Cultural Heritage Objects

The last objective is focused on functional verification of the suggested measurement and monitoring procedures using the proposed quantitative imaging modalities in two scenarios: separately each modality and merged multiple modal-

ities. Data processing protocols and methodologies have to be developed, which can provide insights to open questions in conservation science related to selected CHOs behaviour under environmental influence or related to conservation methods. Therefore, mock-ups or/and real objects have to be monitored in situ with the aim to :

- Document and archive the current object condition;
- Determine the scale of changes in terms of shape, displacements and strains;
- Monitor the global and local spatio-temporal response of the object under changing conditions;
- Correlate known object features with the detected response;
- Evaluate conservation methods with respect to their effect on the structural integrity of the object;

1.4 Structure of the Thesis

The work is organized as follows: after a brief introduction and motivation behind the work (Chapter 1), Chapter 2 contains a summary of theoretical background and the state of the art of of the imaging modalities that will be used in the multimodal system. Chapter 3 presents the design and specifications of the developed optomechatronics system, while in Chapter 4 the detailed overview of the development and implementation for each modality and their merging into a single coordinate system is provided. Chapter 5 describes experimental results and monitoring sessions involving CHOs (paintings, parchments and a globe) performed with the separate modalities, while in Chapter 6 the results of multimodal measurement and monitoring of a painting on canvas and a historical parchment are presented. Chapter 7 concludes the work and discusses possible future directions .

1.5 Funding

The research leading to the results described in the present thesis has been financially supported by the project CHANGE:Cultural Heritage Analysis for New Generations - Innovative Training Network", that has received funding from the European Unions Horizon 2020

Research and Innovation program under the Marie Skodowska-Curie grant agreement No. 813789. The project has received additional financial support by the Scientific Council of the Discipline Automation, Electronics and Electrical Engineering, of Warsaw University of Technology, under the grant agreement No 504/04542/1143/43.020004.

2

Background and State of the Art

Optical methods provide powerful tools for capturing, tracking and documentation of changes in CHOs [3]; however, monitoring the entire object is possible only with the appropriate utilization of vision based and computational methods. This chapter presents the current state of 3D imaging techniques as applied to documenting cultural heritage objects and their changes resulting from exposure to environmental conditions and mechanical loads. I focus here on the selection of incoherent light, full-field optical methods providing information about such important measurands as: the surface geometry (3D scanning/Structured Light method), 3D displacements/strains (3D Digital Image Correlation method) and spectral reflectance (multispectral/hyperspectral imaging). All these methods rely on the proper calibration of cameras (CCD/CMOS) capturing the images that carry information about an investigated object. Therefore, the principles of camera and stereocamera setups are explained first. At the end of the chapter, a general overview of multimodal 3D imaging methods (MMI), which combine imaging modalities to capture different aspects of an object's structure and composition, is presented.

2.1 Calibration

Camera Calibration

Precise calibration of cameras plays a crucial role in obtaining accurate 3D measurements. Consequently, we will address this subject,before delving into the individual imaging modalities of the MIS. The reliable reconstruction of the scene's 3D structure relies on precise calibration. Through calibration we can retrieve both the intrinsic and extrinsic parameters of the two cameras and projector of the MIS. Intrinsic parameters include lens distortion, focal length, and image sensor characteristics, while extrinsic parameters define the spatial relationship between the utilized hardware. Accurate determination of these parameters enables the system to compensate for lens distortion and other optical effects, leading to more precise depth measurements. Stereo matching algorithms rely on finding corresponding points between the left and right camera views, or camera and projected patterns in the case of SL with single camera, to estimate the depth. Precise calibration reduces errors in correspondence matching and enhances the accuracy of the depth estimation. Therefore, it is crucial for both SL and 3D DIC modalities of the MIS, while lens distortion correction improves also the quality of the images recorded for MSI.

Pinhole camera model

The calibration techniques commonly employed for cameras and 3D space rely on the pinhole camera model [41, 42]. The pinhole camera model is a good approximation of how light rays pass through a small aperture to form an image on a sensor, and using a perspective projection it is possible to map the 3D world points and the 2D image points. It is the basis for understanding the principles of geometry projection used in traditional cameras and computer vision systems. Assuming the geometry of Fig. 2.1), where the projection center is located at C, the principal axis is parallel to z axis, and the image plane is located at distance equal to the focal length f, away from C.

A perspective transformation can be used to map a 3D world point $P_w = (X, Y, Z)^T$ onto the camera's image plane at the coordinate $P_c = (u, v)^T$. The point position at the image plane based on euclidean geometry is $(\frac{f}{Z} = \frac{u}{X} = \frac{u}{Y})$, which yields $u = \frac{fX}{Z}$ and $v = \frac{fY}{Z}$. The image points are represented using homogeneous coordinates,$P_c = (u, v, w)^T$, where typically w=1, and by also introducing homogeneous coordinates for the word points as well P_W

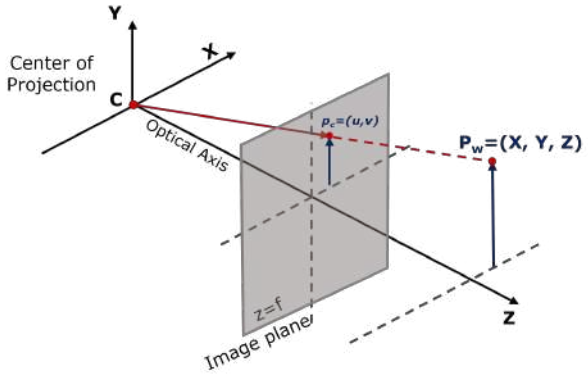

Figure 2.1: Pinhole camera model. The camera center C represents the projection center. Optical axis is the perpendicular line passing from the C. Principal point is the intersect of the optical axis and image plane. Pc is the point in the camera's image plane and Pw is the point in the 3D world.

becomes $P_w = (x, y, z, 1)^T$.Assuming zero offset, the central projection can be written in the form of a linear mapping as:

$$\begin{bmatrix} u \\ u \\ 1 \end{bmatrix} = \begin{bmatrix} f & 0 & 0 & 0 \\ 0 & f & 0 & 0 \\ 0 & 0 & 1 & 0 \end{bmatrix} \begin{bmatrix} X \\ Y \\ Z \\ 1 \end{bmatrix} \tag{2.1}$$

Introducing also the offset of the point from the principal axis u, v becomes:

$$u = \frac{fX}{Z} + t_u, and\, v = \frac{fY}{Z} + t_v \tag{2.2}$$

and therefore turns Eq.2.1 into:

$$\begin{bmatrix} u \\ v \\ 1 \end{bmatrix} = \begin{bmatrix} f & 0 & t_x & 0 \\ 0 & f & t_y & 0 \\ 0 & 0 & 1 & 0 \end{bmatrix} \begin{bmatrix} X \\ Y \\ Z \\ 1 \end{bmatrix} \tag{2.3}$$

Taking into account the camera resolution (pixel/unit length in inches or millimeters) and assume rectangle pixels of $m_u and m_v$ resolution, then u and v become:

$$u = m_u \frac{fX}{Z} + m_u t_u, and\, v = m_v \frac{fY}{Z} + m_v t_v \tag{2.4}$$

Thus, Eq. 2.3 can be written as:

$$\begin{bmatrix} u \\ v \\ 1 \end{bmatrix} = \begin{bmatrix} m_u f & 0 & m_u t_u & 0 \\ 0 & m_v f & m_v t_v & 0 \\ 0 & 0 & 1 & 0 \end{bmatrix} \begin{bmatrix} X \\ Y \\ Z \\ 1 \end{bmatrix} = \begin{bmatrix} a_x f & 0 & u_0 & 0 \\ 0 & a_y & v_0 & 0 \\ 0 & 0 & 1 & 0 \end{bmatrix} P_w = KP_w \tag{2.5}$$

The first matrix on the right side of Eq. 2.5 is the camera intrinsic matrix, which generally is written as:

$$K = \begin{bmatrix} a_x & s & u_0 & 0 \\ 0 & a_y & v_0 & 0 \\ 0 & 0 & 1 & 0 \end{bmatrix} \tag{2.6}$$

Sometimes K also has a skew parameter s, used when the axes of the image plane are skewed and defined as $s = \alpha cot\theta$, with α the pixel magnification factor and θ the skew angle which is equal to $\pi/2$ for most cameras. This matrix depends on the intrinsic camera parameters (focal length, principal axis) and thus represents the intrinsic parameters of the camera. In the case that the camera's center of projection is not located at the origin C=(0, 0, 0) and is randomly positioned, then it becomes necessary to apply a rotation and translation in order to align the camera's coordinate system with the center of projection. In the case that the camera's center of projection is not located at the origin (0, 0, 0) and is randomly positioned, then it becomes necessary to apply a rotation and translation in order to align the camera's coordinate system with the center of projection. Assuming that the translation and rotation needed to bring the camera coordinates to C, is represented as T(T_x, T_y, T_z) and a 3 by 3 rotation matrix R. Therefore the P_c can be expressed as:

$$P_c = KR(I|T)P_w = C_M P \tag{2.7}$$

where C_M is the camera matrix that includes both the rotation and translation for bringing the camera at (0,0,0) and the intrinsic parameters.

There are multiple approaches for the determination of the camera matrix parameters, with the most common based on known calibration points [42, 43, 44]. In practice multiple images of a known planar target are recorded by the camera, with either the camera of target moving between frames. By detecting location of the target points between frames and using the direct linear transformation method it is possible to obtain an estimated projection

matrix, which accompanied by the Zhang method allows for extracting the complete camera matrix.

Stereo calibration

Stereo calibration determines the intrinsic and extrinsic parameters of a stereo camera setup, meaning the geometry of two perspective views, acquired simultaneously as in a stereo rig. It involves finding the relative positions and orientations of two or more cameras to accurately estimate the 3D structure of a scene from stereo images. Stereo calibration is linked to the pinhole camera model by estimating camera parameters. For the purposes of this work, the stereo system consists of two cameras, the approach is similar for more.

Stereo calibration computes the geometrical correspondence between two cameras and the respective world points. Assuming the geometry of Fig. 2.2, where two cameras are observing the same scene, each camera has the corresponding camera matrix C_1 and C_2 and P is a point in the 3D world. Then $x_1 = C_1 P$ and $x_2 = C_2 P$ describe the projection of the points in the image plane to the world scene. The geometry that relates the cameras, the world points in 3D, and the corresponding positions in the image plane is referred to as the epipolar geometry of a stereo pair. The points of the image, the cameras and the 3D world point are coplanar, and rays back projected from the camera points x_1 and x_2 intersect at P. The epipole (e1 and e2) is the point of intersection of the line joining the baseline with the image plane, and the epipolar line (l1 and l2) is the intersection of the epipolar plane with the image plane. The epipolar plane intersects the left and right image planes at the epipolar lines, and defines the correspondence between the lines. This geometry is described by the fundamental matrix, which gives the stereo correspondnce between a pair of images. The fundamental matrix is the unique 3 by 3 homogeneous matrix which satisfies the condition that for any pair of corresponding points:

$$x_2^T F x_1 = 0 \tag{2.8}$$

The essential matrix is the specialization of the fundamental matrix to the case of normalized image coordinates. It is a 3 by 3 matrix which can be described by:

$$E = K_2^T F K_1 = 0 \tag{2.9}$$

Both the Essential and Fundamental matrices describe the geometric relationship between corresponding points of a stereo pair of cameras. The difference between the two is that the essential deals with calibrated cameras, while the fundamental deals with uncalibrated cameras. The Essential matrix contains five parameters (three for rotation and two for the direction of translation - the magnitude of translation cannot be recovered) and has two constraints: (1) its determinant is zero, and (2) its two non-zero singular values are equal. The Fundamental matrix contains seven parameters (two for each of the epipoles and three for the homography between the two pencils of epipolar lines) and its rank is always two.

The correspondence between the calibration patterns in the 3D world and their projected image coordinates is identified by capturing calibration images with known patterns. After each camera is calibrated with a pinhole camera model, external parameters are calculated to determine the relative position and orientation of the camera, meaning the fundamental and essential matrices, in the stereo system. The detected patterns of the calibration target, are utilized to retrieve both the intrinsic and extrinsic parameters of the stereopair. Stereo calibration returns a single rotation and translation matrix (R, T) that relates the coordinates for the left and right cameras in the real world. In addition, through the calibration it's possible to compensate for lens distortion and align the epipolar lines of the recorded images. The retrieved matrices and information can be utilized further for accurate triangulation of 3D points. Therefore, it is a crucial step both for the SL modality with two cameras and the 3DIC modality [45, 41] of the MIS, as it determines the achieved accuracy.

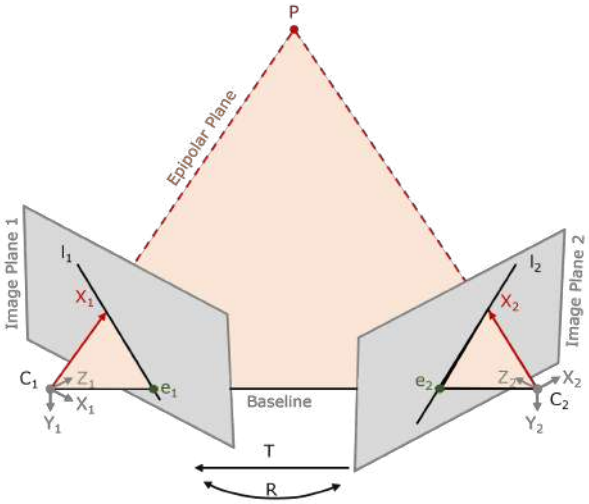

Figure 2.2: Stereo camera model. C1 is the origin of left camera coordinate system, C2 is for the right. P is the point in the real world coordinates, while P1 and P2 are the projections of P in the left and right camera planes respectively.

2.2 3D Scanning

2.2.1 3D scanning techniques

3D scanning techniques can be divided into active and passive [46]. In active techniques, the measurement system emits a beam of a specific type of radiation towards the object to be measured. A detector (usually in the form of a digital camera) records the beam's interaction with the surface. Information about the surface coordinates (x, y, z) is obtained based on image analysis. Passive techniques, on the other hand, only use ambient lighting, usually natural or artificial lighting that mimics sunlight. Most of the techniques discussed here work well with diffuse surfaces. Some of them allow the reconstruction of partially reflective surfaces. Transparent surfaces on the other hand are difficult to image with typical 3D techniques and they are not considered here. The Table 2.1 summarises the main techniques and their features.

Table 2.1: 3D Scanning Methods

Technique	**Active/-Passive**	**Suitable for Reflective Surfaces**	**Equipment Cost**	**Accuracy**	**Comments**
Photogrammetry (recently: structure from motion)	Passive	No	Low	Reasonable, variable	Variable accuracy across an object, low human effort
Laser triangulation	Active	No	Average	High	Considerable manual effort
Time of Flight	Active	No	High	Low	Large volume
Structured Light	Active	No	Average	High	Small to medium volume, detail reconstruction

Photogrammetry

Photogrammetric computer vision approach derives originally from photogrammetry [47] but have been automated using computer vision in the last two decades [48]. They belong to the passive methods. They are also often referred to as the Structure from Motion (SfM) pipeline. They have gained popularity in recent years mainly due to their wide availability, relatively low cost, ease of use and automation of the 3D model generation process. To produce a basic 3D digital model of a CH object, all that is required is a digital camera and reconstruction software from photographs and in principle there is no restriction on the object's dimension [49]. On the other hand, the main disadvantage is that it is based on surface feature points identifiable in the recorded images. As a result, the final model's resolution and accuracy depend on the object surface's variation. In addition, in the process of dense reconstruction, points with much larger reconstruction errors are added, which results in variable representation quality in different parts of the surface.

Laser triangulation

Laser triangulation (LT) [50] is the longest-used active technique for three-dimensional imaging. Unlike passive techniques, it is characterised by a uniform distribution of measurement points with (x, y, z) coordinates on the objects surface. A typical laser triangulation system is built with a laser source rigidly connected to a camera. The laser source system is usually accompanied by a beam-forming module that allows the projection of a point, line or set of lines onto the objects surface to be measured. Based on the knowledge of the geometric relationship between the projected beam and the camera calibration, the coordinates (x, y, z) of the CH object surfaces are determined [51]. A typical measurement field of an LT scanner ranges from several centimetres to several meters with a measurement uncertainty of 1/10,000 to the dimension of the field. The main advantages of the LT technique are the uniform sampling of the 3D geometry of the surface under investigation regardless of its colour variation, the constant and known uncertainty of measurement at each point (x, y, z) and the possibility of use in strong illumination (e.g. sunlight). The main disadvantages include the difficulty of imaging small surface details due to the cross-dimension of the laser beam (approximately 0.6-0.8mm) and the need to scan the beam through the analysed surface, which increases measurement time and requires costly precision engineering.

Time of Flight

The time-of-flight (ToF) method [52] is used to measure the 3D surface geometry of large objects or areas, typically ranging from several metres to several kilometres. The system implementing a ToF measurement consists of a laser that can generate very short light pulses, a radiation detector, an optical system and a mechanical system. The laser emits a short light pulse in the direction of the surface to be surveyed. The pulse scatters on it, and part of its energy is imaged on the detector, equipped with spectral filters adapted to the wavelength of the radiation from the laser. The detector records the time elapsed between the emission of the pulse and its return and from this, the distance to the surface under investigation is determined. The mechanical scanning system allows the laser beam to sweep in two perpendicular axes, thus enabling nearly omnidirectional imaging. More modern solutions additionally use sinusoidal modulation [53] of the emitted pulse and multiple registrations of the returning beam to achieve higher accuracies in distance measurement using phase shift methods. Given a much larger measurement field, the advantages of the ToF technique overlap with those of LT. The main disadvantages include the need to scan the beam, which increases measurement time and requires costly precision engineering, and relatively large measurement errors (of the order of a few millimetres).

Structured Light

The structured light (SL) method [54], although known since 60-ties of 20^{th} century, had become widespread with the development of digital light projection technology. This technique allows a uniform sampling of the surface to be surveyed, resulting in measurement points with (x, y, z) coordinates that are also uniformly distributed over the objects surface. A typical structured illumination system consists of a rigidly connected digital raster projector and a detector or multiple detectors. The digital raster projector projects one or more images onto the surface to be surveyed. After each image is projected, the detector captures an image of the raster deformed on the objects surface. A typical measurement volume of an SL scanner ranges from several millimetres to several metres with a measurement uncertainty of 1/10,000 to the dimension of the volume. The advantages of SL technology are the same as those of LT, considering the absence of mechanical components, which increases the failure-free time of this type of solution. The main disadvantages include the limitation in terms of lighting conditions due to the need to illuminate the entire field of the measured area (high

contrast of the projected raster is required). As shown in the Table 2.1 and discussed above the selection of the 3D scanning method depends on the requirements set by the user based on the knowledge of an object and the final goal of the measurements. It is first necessary to define technical parameters which directly impact the time and cost of the entire process [55, 56], including: measurement volume, spatial resolution, measurement uncertainty, final data format (usually a point cloud (x, y, z) or triangle mesh format). In addition, factors that affect the 3D scanning process should be considered, such as: external illumination, stability of temperature and humidity, cooperation with conservators including the requirement to perform measurement in laboratory or in open space, interference with the object and of course the cost of equipment.

Taking into consideration the technical assumptions presented in Ch. 1.3, below the structured light method is presented in more detailed as the method which provides high resolution 3D measurements of a medium-sized objects with scattering surfaces and requires the relatively low cost and highly reliable hardware.

2.2.2 Structured Light

As mentioned in the above section structured light systems [54] operate by projecting on an object a pattern with varying intensity and capturing the deformation of the pattern caused by the objects height variations using a 2D sensor. They are preferred for scanning objects that do not have highly reflective surfaces or dark colours. SL imaging systems work by analyzing the deformation of projected pattern(s) (Fig. 2.3 by using various structured light concepts and algorithms [57, 54]

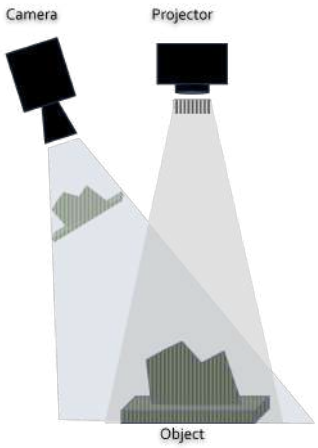

Figure 2.3: The principle of the SL method.

The most commonly used modern technique from the family of methods with structured light is the hybrid projection technique (HP) of sinusoidal fringes and binary codes (called Gray codes) [58]. This method allows to calculate the absolute phase of an object with arbitrary (even very high or step-like) gradients as well measure a 3D scene with several separate objects. The phase of an object Φ, which after calibration of a measurement volume is recalculated to the object co-ordinates (x,y,z), is represented by:

$$\Phi(i,j) = (N_i + N_f)2\pi \tag{2.10}$$

where N_i - integer number of fringe , $N_f = \frac{1}{2\pi}\Phi(i,j)mod(2\pi)$ fractional fringe number; (i,j) are the pixel co-ordinates.

In HP the integer fringe number N_i is provided by the Gray code method. In the Gray code [57] method n patterns are projected in order to encode 2^n stripes, The pattern associated with each pixel is a sequence of zeros and ones obtained from the n patterns. The 0 corresponds to black, while the 1 corresponds to a fully illuminated scene, which ensures there is in large intensity differences between adjacent stripes. The number of stripes increases by a factor of two for each consecutive pattern, while vertical stripes are used for the columns and horizontal for the rows. The maximum number of patterns that can be projected is equal to the pixel resolution of the projector. Gray code ensures that there is only one bit of difference between consecutive patterns. Each pixels value needs to be clearly distinguished (0 or 1) and in order to achieve this the inverse colour patterns are also projected on the surface. To overcome this limitation, it is recommended to project a pattern and its colour-inverted version, which helps in easily determining the intensity value of each pixel (Fig. 2.4).

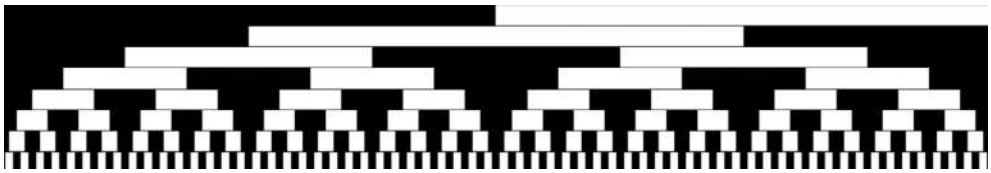

Figure 2.4: Graycode pattern sequence for projector 1024pixels.

The resulting projection sequence encompasses the Gray-encoded column and row patterns, along with their corresponding inverted patterns, as well as two solid colour images, each representing a distinct colour employed in the sequence. The integer number of fringe is calculated independently for each pixel and therefore it can be correctly identified even for step-like objects. The fractional number of fringe N_f is calculated from the phase shifted

fringes with sinusoidal variation of intensity projected on an object:

$$I(i,j) = B(i,j) + M(i,j)cos(\Phi(i,j) + \delta_k) \tag{2.11}$$

where B is the average intensity and M the intensity modulation of the fringe pattern respectively, and δ_k is the phase shift (usually $2\pi/3$ for 3 step phase shift methods) [59, 57]. The phase $mod(2\pi)$, whose value ranges from 0 to 2, is calculated according to one of the phase shifting algorithm method for fringe pattern analysis [59, 57] and is combined with the $N_i 2\pi$ phase values obtained from the Gray codes analysis. The use of sinusoidal fringes and phase shifting method allows for so-called sub-pixel measurement resolutions. It is possible to determine the position of structures projected from the projector with a resolution of less than one pixel in the detector coordinates. In refined solutions, a resolution of one-twentieth of a pixel dimension with respect to the objects surface is achieved. The phase function calculated this way have unique values across the volume in of the camera and it codes information about the distance along the optical axis. After calibration of the measurement volume, which is achieved by measuring a known model (target) in several positions, the (x; y; z) point coordinates of the object in the 3D space are calculated. This process helps in the resolution of any uncertainties or inaccuracies present in the initial estimation of depth. Processing all pixels with properly registered fringes results in a point cloud representing the surface of the scanned object.

2.2.3 Structured Light scanning in CH

Structured light method is popular methodology employed in the field of cultural heritage for a variety of reasons. The use of SL enables the precise and non-destructive digitization of cultural artifacts, artworks, and historical sites, ensuring a high level of accuracy [60]. The creation of detailed three-dimensional models serves as a means to safeguard cultural heritage by recording it in a digital format, thus ensuring the documentation and accessibility of significant artifacts and sites for the generations to come [61]. Furthermore, it serves as a basis for actions aimed at conserving and restoring CH. It enables the remote examination of the CHO or site by professionals [62], allowing for an in-depth evaluation that includes the detection of damages or deterioration [63, 64, 65, 66]. This information serves as a valuable resource for guiding the conservation process and supporting decision-making in relation

to restoration projects or the virtual reconstruction of the CHO [67, 68]. 3D models can be utilized for the purpose of comparing with subsequent scans in order to effectively monitor any alterations or degradation that may occur over a period of time [63, 66]. This data facilitates the formulation of preventative measures and conservation strategies aimed at mitigating risks and ensuring the long-term preservation of resources. SL method is employed for the purpose of monitoring objects or sites throughout the conservation/restoration processes [69] or aging [70, 63] and even for development of safe packaging strategies [71]. The utilization of 3D models allows to conduct measurements, comparisons, and analysis associated to a range of factors, such as shape, dimensions, material composition, and surface details. The provided information serves as an asset to scholarly research, as well as efforts connected with cataloging and documentation. The digitized 3D models are core for the creation of virtual exhibitions, and interactive presentations [72, 73, 74, 75]. This facilitates the dissemination of cultural heritage objects and sites to a broader audience through museums, cultural institutions, and educational platforms. The process of scanning and digitizing cultural objects plays a crucial role in the assessment and mitigation of risks associated with their preservation.

2.3 Digital Image Correlation

The structural health of CHOs and their response The influence of environmental conditions on CHOs results in changes in their physical and mechanical properties. To measure and monitor these changes, a method capable of tracking local and global displacements is required. Hence, such a method should combine a large field of view with sub-millimeter resolution and accuracy for in plane and out of plane displacements determination. Full-field optical measurement methods are best suited for performing such tasks as they perform measurements in non-contact and non-invasive manner [76, 77, 78].Among these methods , the most practical and versatile, machine vision based technique is the DIC [41]. DIC is a versatile, full-field optical metrology technique with applications mainly in mechanical and civil engineering. This method is extensively used in monitoring of deformation, vibration, and strains on almost any material in static as well as dynamic conditions. The applications vary from structural monitoring of buildings and membranes up to open heart surgery, ranging from macro to micro level of resolution. With such a wide spectrum of applications, DIC

is an important full field, non invasive tool with numerous potential applications in the field of Cultural Heritage.

2.3.1 Digital Image Correlation working principle

Digital Image Correlation is implemented in one of two basic setups: 2D DIC and 3D DIC. 2D-DIC uses one camera to determine in plane displacements U(x,y) and V(x,y), while 3D DIC uses two cameras for in plane and out of plane W(x,y) displacements and shape (x,y,z) (Fig.2.5a,b). The 2D DIC measurement procedure requires acquiring a set of images of an object subjected to mechanical or environmental load. The object has to exhibit a random, high contrast texture (a unique pixel intensity pattern) on its surface (Fig.2.5a). The best results are obtained for a black and white pattern which is adherent to an object surface firmly, but without changing its chemical and physical properties. In addition, the pattern is expected to follow the surface response to any loading and it should not dissolve under the presence of high humidity or temperature [41].

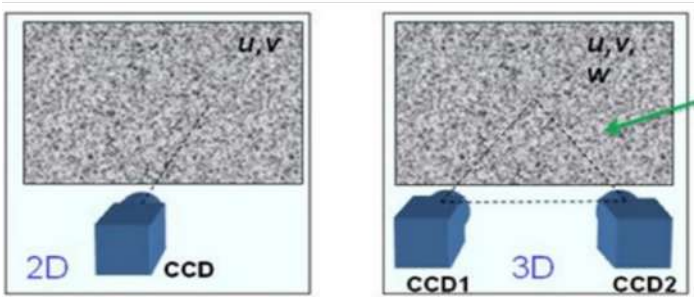

Figure 2.5: DIC configurations: a) 2D DIC , b) 3D DIC and c) example random texture.

The first captured image is selected as a reference image (in most cases, the image captured before the load is applied), and the remaining images are subjected to correlation analysis. The reference image is divided into small subsets. The subsets are subsequently matched against similar subsets in images acquired at different load states. Repeating the procedure for all subsets with a selected step yields in plane displacements maps (Fig. 2.6 2D DIC path), which in the following steps can be used for calculations of strains [41].

The metric which evaluates the successfulness of the subset tracking is called correlation coefficient (Sigma) and its basic representation is given as:

$$Sigma^2_{SSD} = \sum [G(p_i) - F(p_i)]^2 \tag{2.12}$$

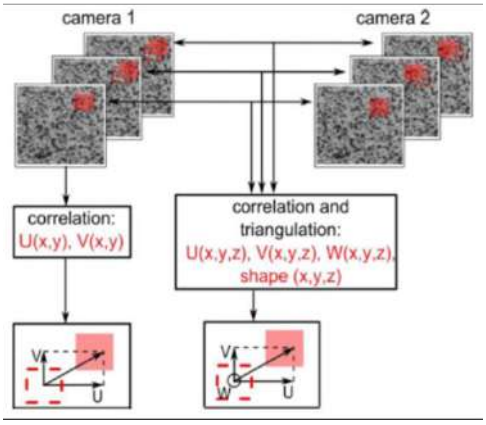

Figure 2.6: The processing paths for 2D DIC and 3D DIC.

where $G(p_i)$ represents the intensity values at in the subset pi of the deformed image and $F(p_i)$ the intensity values in the subset at the reference one. For perfect correlation $F(p_i) = G(p_i)$ and the sigma factor is equal to zero. Accurate template matching criteria are required even when changes in the lighting conditions occur between the reference and deformed images and subsets. Therefore a set of more advanced correlation criteria have been proposed [41]], which are insensitive to uniform (offset) and linear intensity light (scale) changes, as summarised in Table 2.2:

Table 2.2: Correlation coefficient criteria.

Name	Formula	Light intensity change
SSD	$\sum [G(p_i) - F(p_i)]^2$	none
ZSSD	$\sum [(G(p_i) - \overline{G}) - (F(p_i) - \overline{F})]^2$	offset
NSSD	$\sum (\frac{\sum_i G(p_i)F(p_i)}{\sum_i G(p_i)^2} - F(p_i))^2$	scale
ZNSSD	$\sum_i ((\frac{\sum_i \overline{G}(p_i)\overline{F}(p_i)}{\sum_i \overline{G}(p_i)^2} G(p_i) - \overline{G}(p_i)\frac{\sum_i \overline{G}(p_i)\overline{F}(p_i)}{\sum_i \overline{G}(p_i)^2}) - F(p_i) + \overline{F})^2$	scale + offset

In the table $\overline{F}(p_i)$ and $\overline{G}(p_i)$, and represent the intensity of pixel i(x,y) within the given subset after subtraction of the average intensity of the subset and are defined as $\overline{F}(p_i) = F(p_i) - \overline{F}$ and $\overline{G}(p_i) = G(p_i) - \overline{G}$ for the reference and loaded images, respectively. The average value of the reference and loaded images over the corresponding subset n_{th} = N x N number of discrete pixels is given by $\overline{F} = \frac{\sum F}{n}$ and $\overline{G} = \frac{\sum G}{n}$. It should be noted that for perfect correlation the factors $Sigma_{NSSD}$ and $Sigma_{ZNSSD}$ are equal to 1.

In 2D DIC basic configuration the resolution of displacement measurement is equal to the dimension is transferred (and often enhanced) of one pixel in the object plane, so it depends on the camera magnification and the number of pixels in the camera. In order to achieve sub-pixel displacement accuracy in DIC, the intensity of the image needs to be

estimated for sub-pixel positions. This is achieved using interpolation methods in combination with iterative optimisation procedures. The interpolation method used for the grayscale intensity values of the pixels has a significant impact on the accuracy of the calculated displacements and strains. This error is commonly referred to as interpolation bias and has been the subject of extensive research [41, 79, 80, 81, 82, 83]. As reported in [41] the amplitude of the interpolation error follows a sinusoidal pattern and is dependent on two factors, the interpolation algorithm and the sub-pixel position (Fig. 2.7).

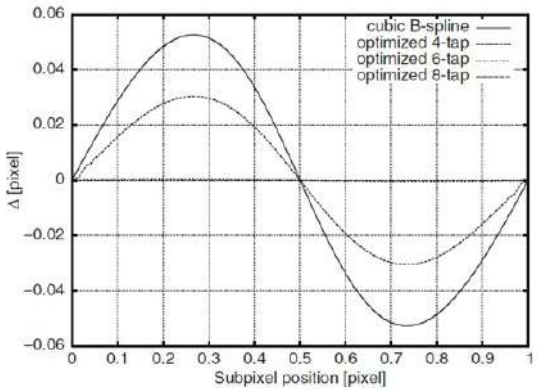

Figure 2.7: Amplitude of interpolation bias as a function of sub-pixel positions [41].

The interpolation procedures using higher order splines are minimizing the error associated the sub-pixel displacement determination. However it should be kept in mind that this error occurs in in plane displacement maps (U and V) and it transfers (and enhances) in the strain maps. The strain maps in 2D DIC are calculated based on differentiation of U and V displacements according to the equations (Eq. 2.13,2.14 ,2.15)[84]:

$$\epsilon_{xx} \cong \frac{\partial u}{\partial x} + \frac{1}{2}[(\frac{\partial u}{\partial x})^2 + (\frac{\partial v}{\partial x})^2]^2 \tag{2.13}$$

$$\epsilon_{yy} \cong \frac{\partial v}{\partial y} + \frac{1}{2}[(\frac{\partial u}{\partial y})^2 + (\frac{\partial v}{y})^2]^2 \tag{2.14}$$

$$\epsilon_{xy} \cong \frac{1}{2}(\frac{\partial u}{\delta y} + \frac{\partial v}{\partial x}) + \frac{1}{2}[\frac{\partial u}{\partial x}\frac{\partial u}{\partial y} + \frac{\partial v}{\partial x}\frac{\partial v}{\partial y}] \tag{2.15}$$

The user determines the length of a virtual extensometer (δx and δy) in pixels depending on the character of displacement maps (local gradients in displacements).

However the 2D DIC method can be used only in the case of flat objects which do not undergo significant out of plane displacements. In general case when 3D objects are investigated, the use of 3D DIC method is advised. 3D DIC technique overcomes the measuring

limitations of 2D DIC, using two synchronised cameras (Fig. 2.5b and Fig. 2.6 3D DIC path). Based on the principle of binocular stereovision, 3D DIC accurately measure full-field 3D shape and in plane and out of plane displacements of both planar and curved surfaces. In 3D DIC, the cameras capture sequential image pairs of a sample under varying loadings. A reference pair of images is selected, and the subsequent ones are used for the correlation analysis. In 3D DIC, the correspondence of the projection of physical points in the left and right images must be established using correlation algorithms (stereo matching). Together with the calibrated parameters of the stereo rig, 3D coordinates of measurement points are recovered with the classic triangulation method. Further, by subtracting the 3D coordinates of the same physical points at the initial state from those of deformed states, three displacement components (U, V, W) caused by external loading can be computed. This is done by temporal matching in which the same physical points in the consecutive images recorded by the same (left or right) camera at different times or states are tracked. Temporal matching can be directly implemented using the subset-based 2D DIC algorithm which was discussed above. Once the displacements U,V,W are calculated the strain maps can be calculated from Eq. 2.13,2.14 ,2.15 or in the case of significant out of plane displacements the relations taking into account W are implemented:

$$\epsilon_{xx} = \frac{\delta u}{\delta x} + \frac{1}{2}[(\frac{\delta u}{\delta x})^2 + (\frac{\delta v}{\delta x})^2 + (\frac{\delta w}{\delta x})^2] \tag{2.16}$$

$$\epsilon_{yy} = \frac{\delta v}{\delta y} + \frac{1}{2}[(\frac{\delta u}{\delta y})^2 + (\frac{\delta v}{\delta y})^2 + (\frac{\delta w}{\delta y})^2] \tag{2.17}$$

$$\epsilon_{xy} = \frac{1}{2}(\frac{\delta u}{\delta x} + \frac{\delta v}{\delta y}) + \frac{1}{2}[(\frac{\delta u}{\delta x}\frac{\delta u}{\delta y})^2 + (\frac{\delta v}{\delta x}\frac{\delta v}{\delta y})^2 + (\frac{\delta w}{\delta x}\frac{\delta w}{\delta y})^2] \tag{2.18}$$

Currently there are plenty of available solutions for performing 3D DIC analysis, both proprietary and open source. The main software used in this thesis is VIC from Correlated Solutions[1] [85], a licensed software that allows fast calculations through a user friendly interface. The downside of this software is the high cost (couple of thousands of euros), but it is a complete and reliable solution which allows also data exporting in multiple formats for further processing. The latest versions of this software have the option of batch programming through VICPy a free library of scripts written in the Python programming language, but this is not an option in the version (VIC-3D 7) used within this work. Another licensed

[1] https://www.correlatedsolutions.com/

software is Istra4D by Dantec Dynamics[2], which seems to offer similar capabilities with VIC, but is not tested in the context of this thesis. A hybrid solution, is DuoDIC an open-source toolbox, which comes under the proprietary MATLAB programming environment, written by Dana Solav's research group at Technion and released in 2022 [86, 87]. The downside of this software is the limited amount of data that can be processed, as everything is stored into a single output file, which can be slow to use. Two open source solutions also exist in C++ and Python languages. The first one is DICe is an open source DIC tool intended for use as a module in an external application or as a standalone analysis [88]. DICe was first released in 2015 with the latest update being in 2020. Last but not least, iCorrVision-3D has recently released a python-based open-source 3D DIC software for both in plane and out of plane full-field measurements. This software includes an integrated stereo grabber for image acquisition, stereo calibration, numerical stereo correlation and post-processing modules [89].

2.3.2 colour Digital Image Correlation

In the context of DIC analysis, it is generally preferred to use monochrome cameras rather than colour cameras with comparable resolution [41, 90]. Nevertheless, several research groups have explored the potential of employing colour cameras for DIC analysis [90, 91, 92]. When colour cameras are utilised in the process of DIC, it is referred to as colour digital image correlation (cDIC). Current colour cameras operate in either full-colour or interpolating mode. Cameras that capture full-colour images are called true-colour or three-CCD cameras. The acquisition of colour components for each pixel is typically achieved by splittilng the spectrum into three components (red, green, and blue) using a prism and recording information using three CCDs [93, 94]. The collected data can be utilised in its original form, with all channels (R, G, and B) being preserved at their full resolution, thereby eliminating the necessity for any interpolation techniques. These solutions have the potential to achieve the highest possible colour depth and spatial resolution while effectively mitigating the issues and distortions commonly encountered in the process of image demosaicing. Nevertheless, it should be noted that the true-colour cameras are expensive, and their availability is limited.

Cameras that operate in interpolation mode, called colour filter array (CFA) or Bayer cameras [95], employ a regular grid to sample each colour component and then estimate

[2] https://www.dantecdynamics.com/

the missing ones by interpolation. The colour filter array (CFA) configuration utilised in the colour camera is the Bayer pattern [95]. The pattern typically has a ratio of two green photodetectors to one red and blue photodetector, with a repeating unit of 2x2 pixels. Implementing this concept involves installing a matrix of colour filters arranged in the Bayer pattern and positioned in front of the monochrome (CCD). CFA cameras are more commonly used for various reasons, including the widespread accessibility of consumer-grade digital cameras that offer high-quality, high-definition imagery with a wide dynamic range [90]. Additionally, the relatively low cost and popularity of these cameras make them a favourable choice in various activities in the field of cultural heritage (ranging from digital photography to documentation). Unless the data is captured and stored in a raw format, the interpolation process occurs inherently within the camera system. The additional post-processing steps of interpolation or demosaicing can be employed when the raw format is chosen. Demosaicking algorithms are employed to reconstruct the absent colour components within an image, thereby enabling the acquisition of full-resolution RGB colour channels. Upon achieving complete resolution of the colour channels, they can be utilised individually or in combination to generate a monochrome image. This monochrome image serves as the input data within the traditional processing pipeline in the context of digital image correlation [41]. However it has been shown that the demosaicing methods can have a significant effect on the DIC output [96, 97].

2.3.3 Digital Image Correlation in CH

The influence of environmental conditions on CHOs results in changes of their physical and mechanical properties. DIC, which is capable to track local and global displacements, can be used to reveal discontinuities or inhomogeneities in their structure, monitor geometrical and strength (strains/stresses) changes while exposed to environmental changes or to assess the compatibility of primary and added materials used in conservation. However the basic DIC requirement to work with a random texture at the surface of CHOs surfaces limit its applications to two cases: (i) investigations of CHOs mock-ups which surfaces can be modified by adding an artificial texture and (ii) measurements of CHOs which natural texture fulfils DIC requirements. In the second case the accuracy of displacements may significantly vary across the field of view. Despite of the above mentioned restrictions, DIC has gained considerable attention and recognition within the heritage science community, as it deliv-

ers valuable information about the structural health of CHOs and supports conservators in assessing restoration techniques and evaluating the stability of repaired structures, as well as in implementation of suitable preservation and storing tactics to mitigate the possibility of damage or deterioration and assure the long term preservation of an object. DIC applications span from monitoring of displacements and strains in parchments [98, 99], historical tapestries [100, 101], wooden structures [102] and paintings on canvas [103, 104, 96] in reaction to fluctuations in the environment, such as changes in temperature and humidity as well as mechanical loadings [105]. As the typical sensitivity of DIC is in the order of several micrometers it is useful for monitoring CH artefacts which are flexible and sensitive to loadings such as parchments, paintings, textile or wooden structures, while it is difficult to implement for materials like stone or ceramic.

2.4 Spectral imaging for reflectance measurement

Spectral imaging methods include a wide range of techniques that can be used to collect and analyse data related to the spectral characteristics of an object across a broad spectrum of wavelengths. These techniques are extensively employed across several scientific disciplines, including remote sensing, astronomy, medical imaging, and materials science. Spectral imaging enables the collection of detailed spectral information for each of the pixels (points within an image), thereby offering significant insights into the composition, chemical attributes, and physical properties of the objects being analysed. Among the most popular spectral imaging methodologies in the field of CH are multispectral (MS) and hyperspectral (HS) imaging.

2.4.1 Multispectral and hyperspectral imaging

MS and HS imaging techniques are well known and thoroughly utilised for the field of cultural heritage. MS and HS imaging combine digital imaging with spectroscopic analysis to recover spatial and spectral information about an artefact. Their implementation produces a sequence of images, each one acquired at a defined spectral band for every pixel of the camera/detector for wavelengths in the range from ultraviolet to the near infrared region of the electromagnetic spectrum. The outcome of this technique is a set of successive images, one spectral image for each spectral band, called spectral (or hyperspectral) cube. Processing

of the spectral cube enables the extraction of useful information on the materials comprising the object under study.

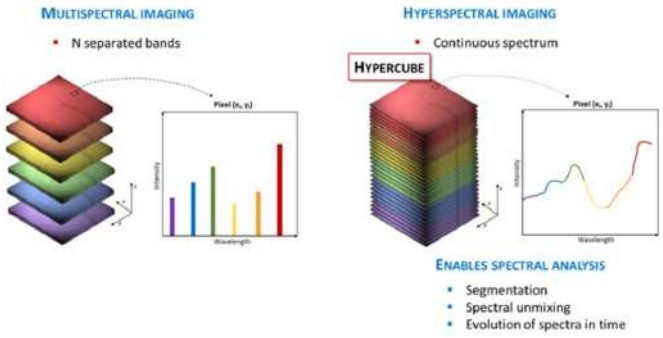

Figure 2.8: Schematic representation of multispectral and hyperspectral cubes[3].

The wavelength of the incident radiation, as well as, the absorption properties of the object are the main factors that determine the penetration depth into a material. Typically, shorter wavelengths interact with surface layers while higher wavelengths penetrate deeper into the materials, providing thus stratigraphic information about the object. MS and HS imaging techniques are not clearly distinguished but the main factors that can differentiate them are the spectral resolution, the number of spectral bands, the band width and the continuity of the recorded spectrum. MS imaging refers to capturing in limited number of bands of the electromagnetic spectrum, while HS imaging usually refers to the recording of more bands and the acquisition of a quasi-continuous spectrum. Typically, an MS system may have from three up to a few tenths spectral windows, with a common bandwidth being in the range of 10-50 nm. A HS system starts from a few dozens of spectral bands and can go up to a few hundreds with a bandwidth of a few nanometers. A set of MS or HS images can be used in a variety of ways depending mainly on the needs of the application. The main operations performed for cultural heritage objects are comparison between images of different bands to enhance or reveal features based on their reflectance response, mathematical operations such as ratio and subtraction methods, composition of false colour images to emphasise and better visualise areas of interest, statistical analysis and spectral identification of components. There are a number of scientific publications dedicated on post processing methodologies that concern either general guidelines or specific case studies using HS and MS imaging [106, 107, 108, 109].

In general, spectral imaging techniques require an illumination system to illuminate the

[3] http://www.nireos.com/what-is-hyperspectral-imaging/

object to be depicted, focusing optics, an imaging sensor to capture the light back-scattered from the object and a means of wavelength selection (dispersive element). Those factors determine the final configuration, the illumination that will be used and the scanning strategy that will be followed. There are a number of different configurations that can be used for MS and HS imaging systems and various workflow schemes Fig. 2.9. Spectral calibration is required in all cases for the accurate recording of the reflectance values and the minimisation of reconstruction errors. The calibration process involves the removal of dark current and the correction of the data using a target with known reflectance (most popular are Spectralon targets) for the variability in illumination because of the sensors spectral response, the positioning of the illumination source and the involved optics. MSI is easier to implement in comparison to HS as it requires simpler, faster and cheaper equipment. Typically, MS imaging systems consist of a monochromator interfered in the light path in front of the imaging sensor or in front of the illumination system. The most common configuration for MS is the use of a filter wheel equipped with appropriate optical band-pass filters in front of a monochromatic camera. Of course, appropriate illumination must also be used, with emission that covers the entire sensors spectrum, such as tungsten and halogen lamps. Sequential images of the object for the whole scanning area are then recorded for each filter that correspond and produce the spectral cube [108, 110]. Usually the filtering system is placed between the lens and the detector, along with a motorised wheel controlled by a computer. Due to the fact that different wavelengths follow different optical paths the focus needs to be adjusted for every sequential frame along with the exposure time. This results in small variations to the field of view and misalignment among the spectral images along with a mechanically unstable system. Therefore prior to the extraction of the spectral data appropriate image registration methods are typically applied [111]. The aforementioned apparatus provides a good solution for MSI as it is relatively low cost, acquires data from large field of view, is easy to position anywhere around an object and generates relatively good quality results. The main disadvantages of this method is the limited and specific amount of filters in the filter wheel, and the low spectral resolution and the low mechanical stability which makes it necessary for registration methods to be applied.

Following another approach, it is possible to produce multispectral images by varying the wavelength of the illumination source (Fig. 2.9a). In this case, an image is captured for every projected wavelength by the camera and the spectral cube is produced. The most pop-

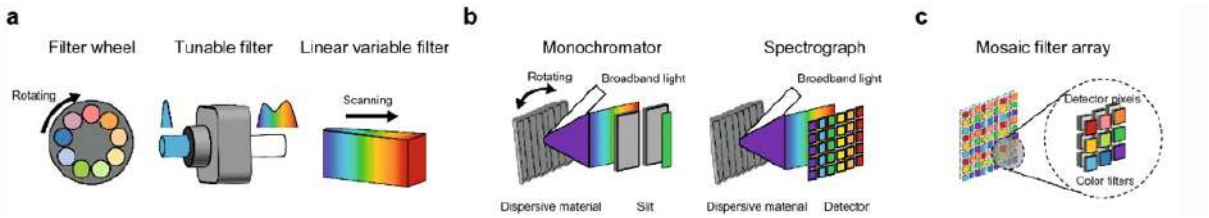

Figure 2.9: Schematic representation of Multispectral and Hyperspectral configuration principle. The figure shows a) multispectral camera with filter wheel, b) HS system in pushbroom and whiskbroom modes, c) MS camera with spectral filter array [112].

ular solution is based on the use of LED illumination, which can provide a low cost, fast and efficient method for retrieving the generally accepted minimum of five spectral bands [113, 114, 115]. In such cases, the MS system is based on multiplexing of the sensors spectral sensitivity and the spectral power distribution (SPD) of the illumination. There is a very broad range of LED sources at different spectral bands that can allow for a high quality multispectral imaging output by combining them with monochrome or colour camera sensors. Nevertheless, attention must be paid to the background illumination as it can compromise the accuracy of the spectral outcome, since no filters are used in front of the detector. In addition, under this configuration its not possible to perform UV-fluorescence imaging as again there is no filter at the camera. Under the same principles the use of RGB cameras for performing MSI under varying LED illumination (Fig. 2.9c) has also been investigated [114].

2.4.2 Multispectral and hyperspectral imaging for CH documentation

Multispectral and hyperspectral imaging techniques have wide-ranging applications in the field of cultural heritage [108]. They are employed for material identification [116, 117], detection of hidden features such as underdrawings [116], pigment mapping [118, 119, 120, 121, 122, 123] and monitoring deterioration processes or cleaning interventions [107, 124, 125, 126], enhancing the visibility of faded text [127, 128], authenticating artworks [129, 130], and recording information for documentation and conservation purposes. The utilisation of such imaging techniques enables the acquisition of comprehensive spectral data, which assists in the identification of different materials, enhancing understanding of artistic techniques, revealing hidden historical information, developing preservation strategies, and identifying authentic artworks from counterfeit ones. Multispectral and hyperspectral imaging techniques offer valuable non-invasive, scientifically robust data that greatly assist the analysis and preservation of CH artefacts.

2.5 Multimodal Imaging

Combining multiple imaging modalities towards the examination of the same CH object is a quite common practice in multiple scientific imaging fields. Multimodal imaging refers to the simultaneous recording of signals for more than one imaging modality, obtaining thus simultaneously a variety of information/quantities related to the target object. The majority of multimodal imagery comes from the field of biomedical imaging, with the most popular clinical applications involving combination of MRI, PET and CT imaging methods [131], and opthalmological applications [132]. Other applications include robotics [133], urban traffic analysis [134], indoor spaces navigation through localization [135], face recognition [136], additive manufacturing [137] to name few. It has also been the subject of EU funded projects such as MUMMERING [138], dedicated to the development research tool that encompasses 3D imaging modalities for applications in materials engineering, and Scan4Reco [139], focused on the development of a multimodal scanning mechanical arm for the collection of photogrammetric, IR, RGB-Depth, Ultrasound, FTIR, Raman, Profilometric, RTI, UV-VIS and acoustic microscopy datasets for multi-layered analysis towards the generation of digital surrogates of CHOs.

Multimodal imaging methodologies are also pretty widespread as diagnostic among the heritage science community [28, 140, 141, 142, 143, 144, 145, 146]. Quite often a single imaging modality is not enough to provide all the needed structural or diagnostic information, and therefore a combination of modalities is preferred. The easiest approach to multimodal imaging is to use multiple individual methods for the characterization, documentation and diagnosis of a single object. For example, in [143] the authors combined hyperspectral with XRF imaging to uncover an ancient paint production technology. In another study, researchers scanned an easel painting with a spectral-domain optical coherence tomography and a terahertz time-domain imaging system [144]. The VERONA (Van Eyck Research in OpeN Access) project is an open library of multimodal imaging for selected artworks, and in specific X-radiography, Infrared Photography, Infrared Reflectography, visual light photography in normal and raking light, as well as macrophotography [145]. Another example is the application of geospatial technologies for the 3D documentation of CH buildings, using laser scanning and photogrammetry [146]. In another approach the authors combined RTI with multispectral imaging using varying LED illumination [29]. Tonsho at. al. [147] developed a

goniophotometric solution which provides spectral reflectance along with specularity information of a surface. They use a setup with a 5-band camera and seven tungsten light sources distributed around the scanned object and a triangulation laser scanner to register 3D shape of the scanned object.

In most of the above examples, each modality is recorded separately and registration protocols are applied to bring the datasets into a common and single world coordinate system. This can be the source of errors both from the registration (including the object repositioning) as well as the interpolation of data with different size. In the recent years research interest has shifted towards achieving multimodal imaging through integrated prototype devices. In this way, registration is simplified and data fusion errors are eliminated as all of the modalities are recorded by the same sensor using the same experimental configuration. Under this umbrella, we will review the latest literature related to the imaging modalities investigated in this thesis.

One popular approach in this direction is the combination of 3D shape measurement, through structured light method, and spectral imaging. Along these lines Bianco et al. [24] combined structured light imaging for shape retrieval with a multispectral camera with a filer wheel. In another approach Mansouri et al. used a custom set up in for the multimodal 3D shape and spectral recording which comprised of a CCD, motorized filter wheel and an LCD projector [148]. Sitnik et al. proposed an integrated SL, BRDF (Bidirectional Reflectance Distribution Function) and MS imaging system using a custom made setup. The prototype consisted of a grayscale camera, Digital Light Processing (DLP) projector for the SL measurement with the addition of filter wheel for the MS part and a grid of LEDs for the BRDF measurement [149].

More recently, a multimodal approach with integrated fringe projection and 2D DIC has also been proposed as a low-cost alternative to 3D DIC [150]. Zhang et al [151] proposed an integrated DIC and multispectral system using a 3 CCD camera and varying illumination for the correction of heatwave distortion. An alternative DIC application is the use of UV- DIC (ultraviolet -DIC) for displacement and strains measurements in high temperatures [152, 153]. In this case UV illumination in combination with CCD sensor(s) provide the opportunity to inspect structures deformation in high temperature, where it would not be possible under normal white light conditions.

2.6 Conclusions

In this chapter the individual imaging modalities, which provide measurements of shape, displacements, strains and reflectivity have been described and their importance to CH preservation and documentation was evidenced. However the specific gaps within the existing solutions were also identified. This refers specifically to 3D DIC for which investigations of CHOs with natural texture are limited and to MSI, which is still lacking a low cost solutions. It was also shown, that despite the numerous examples of multimodal systems (or rather quasi-multimodal as most of the examples utilize separate measurement system for each modality), a solution which incorporates shape, displacements/strains and reflectivity does not exist. Therefore in the next chapters the integrated measurement system with the enhanced SL, 3D DIC and MSI modalities will be presented. The minimum hardware required for each of the modalities is well defined, and can is summarized in Fig. 2.10.

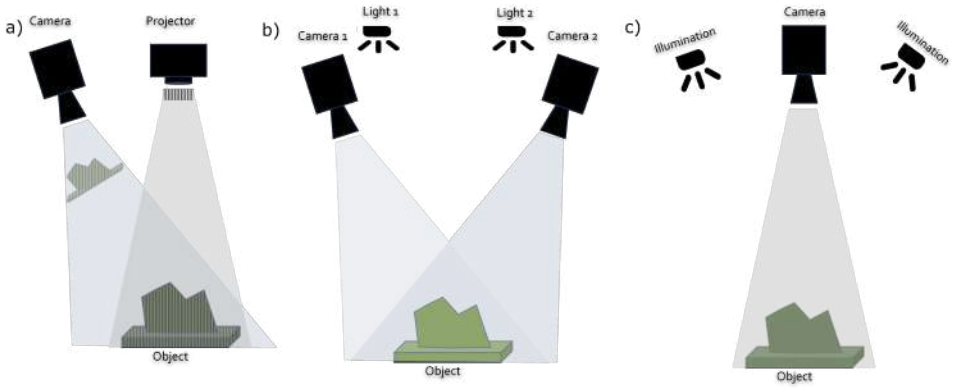

Figure 2.10: Schematic representation of the minimum hardware necessary for a) shape (SL), b) displacements and strains (3D DIC) and reflectance (MSI) measurement.

Currently, there is lack of a single measurement solutions that include multiple modalities in this direction. Therefore, within the scope of this thesis it is aspired to create an integrated measurement solution which can be used in-situ by conservators for the acquisition of multimodal and multitemporal data. To achieve this, a demonstrator device is proposed and presented which utilizes a stereo vision approach for the generation of data in a single coordinate system utilizing SL, cDIC and MSI. The proposed solution is based on the utilization of the minimum hardware requirements for the individual modalities and development of data capturing and data processing methodologies.

3

Optomechatronics design and prototype development

3.1 The concept of Multimodal Imaging System

The main objective of this thesis is to develop an integrated measurement solution that can be utilized on-site by conservators to gather multimodal information about a CHO and it's spatio temporal changes in shape, displacements and spectral reflectivity . In order to accomplish this objective, the basic concept of Multimodal Imaging System (MIS) is presented. This device consists of a relatively simple hardware and employs a stereo vision configuration to generate SL, 3D cDIC, and MSI data within a unified world coordinate system. The schematic representation of the MIS configuration, along with the imaging modalities and output quantities is presented in Fig. 3.1.

Based on the background knowledge and the initial tests performed using each modality of the system separately, as well as multiple consultations with conservators and con-

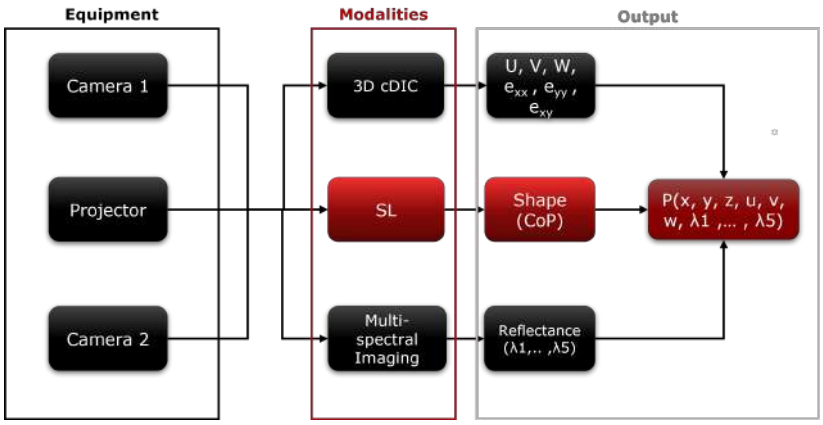

Figure 3.1: Schematic representation of the equipment and modalities of the MIS.

servation scientists several technical requirements were considered prior to the selection of system commercial modules and the optomechatronic design. They include restrictions on the CHOs features, field of view (FoV) and resolution, portability and frequency of monitoring, as shown in Table 3.1. In order to provide flexibility in the data acquisition resolution, depending on the selected measurement task, the system allows for replacing cameras and lenses and changing its relative position (changing the base dimension and base angle), within reasonable distances which do not compromise its mechanical stability. The minimum baseline was chosen based also on limitations set by the dimensions of the selected modules (projector and cameras), while the maximum distance was selected with the aim to ensure mechanical stability of the optoelectronic modules as well as the final weight of the system.

3.2 The optomechatronics design

MIS is composed of specially designed mechanical support structure and commercial components, selected to fulfill both technical and cost requirements for the multimodal portable system. The main commercial modules of the system are listed in Table 3.2. Additionally to the system modules listed in the table, MIS requires a computer equipped with software for data recording, processing and visualization (proprietary DIC software, camera and projector manufacturer software, termite communication port, and scripts developed in the scope of this thesis for data processing, merging, and analysis). The main computer used for this system has Intel 82579LM Gigabit network adapter, processor Intel(R) Xeon(R) CPU E5-2687W 3.10GHz, 8 Cores, RAM 32GB, operating in Microsoft Windows environment. Other

Table 3.1: System Requirements

Requirement	Solution
CHOs Restrictions	General : scattering or partially scaterring surfaces Modalities: • SL: surfaces with arbitrary texture, cannot work on black surfaces; • DIC: surfaces with prominent texture, homogeneous colour surfaces cannot be analyzed; • MSI: the spectral reflectivity analysis can be potentially performed in all types of surfaces but best results are expected on scattering surfaces; Objects with high shape gradient might require multiple positioning of the object, which would compromise the accuracy of the results. Also, the object should be positioned in an environment that is mechanically stable (vibrations)
FoV and resolution	The objects selected to be studied/ analysed are of middle size which refers to measurement volume smaller than 50*50*30cm. In the case of larger object, either a smaller area of interest should be selected or multiple scans are required. Expected accuracy in shape is 0.2mm (SL) and expected accuracy in displacements app. 0.1 pixel size in the object plane (DIC)
Portability	The system should not weight more than 10 kg and be easy to transport. It should fit into a transportation case with standard and acceptable dimensions for commercial flights and transportation providers
Data capturing frequency	Slowly varying changes are assumed, and therefore it is sufficient to implement a frame rate of up to 8fps. For experimental data the capturing frequency will be defined based on the studied phenomena.

computers can also be used, and of course the data recording and processing time will vary depending on the specifications of the pc.

The mechanical structure of the demonstrator is designed with the usage of carbon fiber composites, invar rods, and a 3D printed case. During the conceptual stage of the design, it was decided on an upside-down design. It directly resulted from the asymmetrical projection of the used projector. We provided a fully functional system demonstrator by turning the projector upside down, with the center of gravity (COG) aligned with the point used for connecting the scanner to a tripod (Fig. 3.2).

The main supporting structure/board of the system is made from carbon fiber. The distance between cameras is determined by the set of 4 holes on both sides of the board. The pattern for holes allows for changing the camera base distance: 586.40 mm, 546.40 mm, 443.80 mm, and 403.80 mm (Fig. 3.3 a). Each camera is attached to the aluminum camera plate which is equipped with the central threaded hole that connects it with the leveling head MagicBalance MBAL20 (Fig. 3.3 b). This design allows for convenient access to each camera and adjusting its position to the projector and the second camera.

Table 3.2: System Modules

Model	Description	Details
Basler aca4112- 8gc	CFA cameras, 4096*3000 pixels	Area Scan Camera, 4096 px x 3000 px, resolution 12 MP, Frame rate 8fps, bit pixel depth 10 or 12 bits
TexasInstruments LightCrafter 3010emv LC	DLP DMD projector, LED based with synchronization board	DLP .3 720p DMD; DLPC3478- Digital Controller for the DLP3010 DMD; DLPA2005- PMIC/LED Driver for the DLP3010 DMD and DLPC3478 controller; RGB LED optical engine from Eprotech
Akurat LL2120hp	White LED photography lamp	Two standard colour temperatures: daily (approx. 5600K) and artificial (approx. 3200K), potentiometer for brightness adjustment
Netgear GS110TP PoE	Gigabit-Ethernet Switch	Network Architecture :Gigabit Ethernet, PoE 802.3af (PSE) up to 15.4W, Number of PoE/PoE+ ports 8, Bandwidth 20Gbps
Mounting	Camera head, Akurat LL2120hp	Novoflex Magic-Balance leveling dome Ø60, inclination 20ř, 3D printed mount for the Akurat LL2120hp
Cables & others	Basler Power-I/O Cables; Ethernet cables; USB cables: microUSB cable angled 20cm and Mini usb cable angled 25cm; Sockets	Basler Power-I/O Cable, HRS 12p/open, twisted, I/O / Power Cables; Gigabit Ethernet Cable; USB cables commercial; USB sockets, power sockets, fuse for power connector
Camera tripod	Tripod Manfrotto Compact	Or any other tripod, designed for professional photography
Camera lens	16mm	Experiments presented in the upcoming chapters are done with 16mm lenses equipped on the cameras. They can be exchanged with any c-mount lens

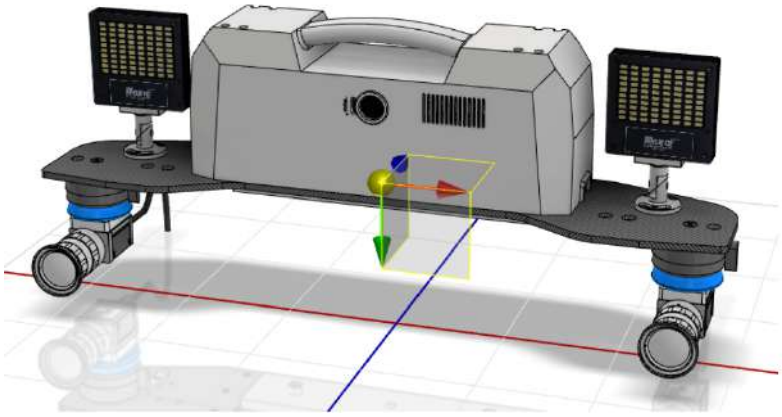

Figure 3.2: The upside-down design allowed to align the COG point with the point of mounting the scanner to a tripod.

The projector is attached to the board (Fig. 3.4 a). The projector board is elevated from the main plate level as the projector lighting aspect is not symmetrical (Fig. 3.4 b). The two boards and rood design ensure the parallelism of the main board and projector board. Roods for stabilization are made from invar (Invar36) bar a material with a very low coefficient of thermal expansion. The carbon boards ensure an unchanged mutual position between cameras and the projector in various ambient temperatures.

The invar roods are fixed to the main board directly and the projector plate is fixed to the roods indirectly by four bolts, and the corresponding holes in the 3D printed housing (Fig. 3.4 b). This connection is designed so that the thermal deformations of the housing should

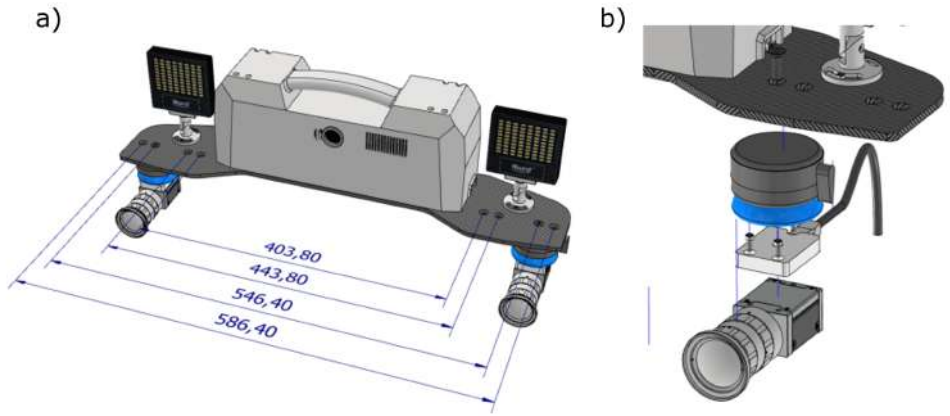

Figure 3.3: a) The base distances in MIS with four alternative base distances and b) the assembly of a single camera mount. The camera is fixed to the camera plate attached to MagicBalance ball head, which in turn is fixed to the carbon plate.

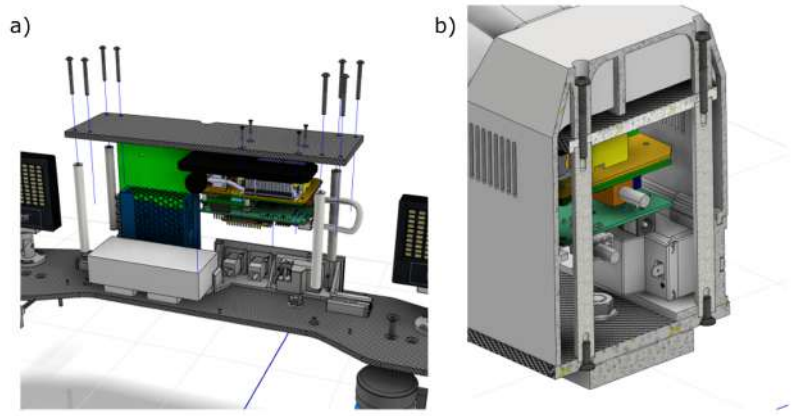

Figure 3.4: a) The assembly of the projector board and the projector and b) the mechanical connection between the invar roods and the 3D printed case.

not affect the supporting structure (plates and invar roods). The power supply (Meanwell LRS-75-12) is fixed to the main board at the back left of the system prototype. The projector power supply (Chieftec CDP 090ITX) is located front left, and two 3D printed pads support it. Its position is also aligned with the socket panel's geometrical features.

The housing of the system prototype is composed of two separate parts. The first part is the socket panel, located on the backside (two USB sockets and the power supply socket (230VAC)). The main housing is connected with the panel by the grove-and-wing connection. It ensures their proper relative position and also compensates for any defects or deformations that might cause during the 3D printing process. The housing has vent slots in the front and back walls; their position ensures proper airflow forced by the projector fans. There is a projection window on the front wall, and close to it is an additional kidney-shaped slot for adjusting the focal length of the projector lens. The housing is also equipped with a

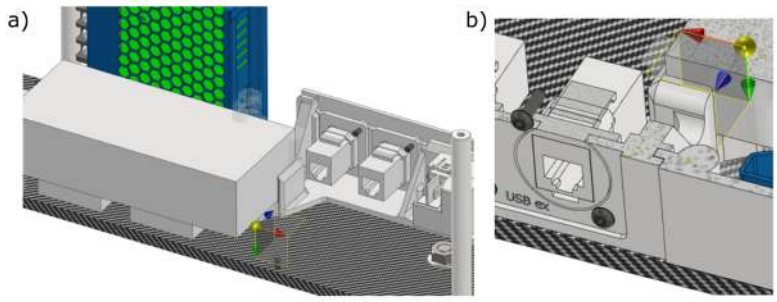

Figure 3.5: a) The position of the projector power supply unit on two 3D printed pads and b) the grove-and-wing connection between housing and the panel for sockets.

handle on the top which allows for easy transportation.

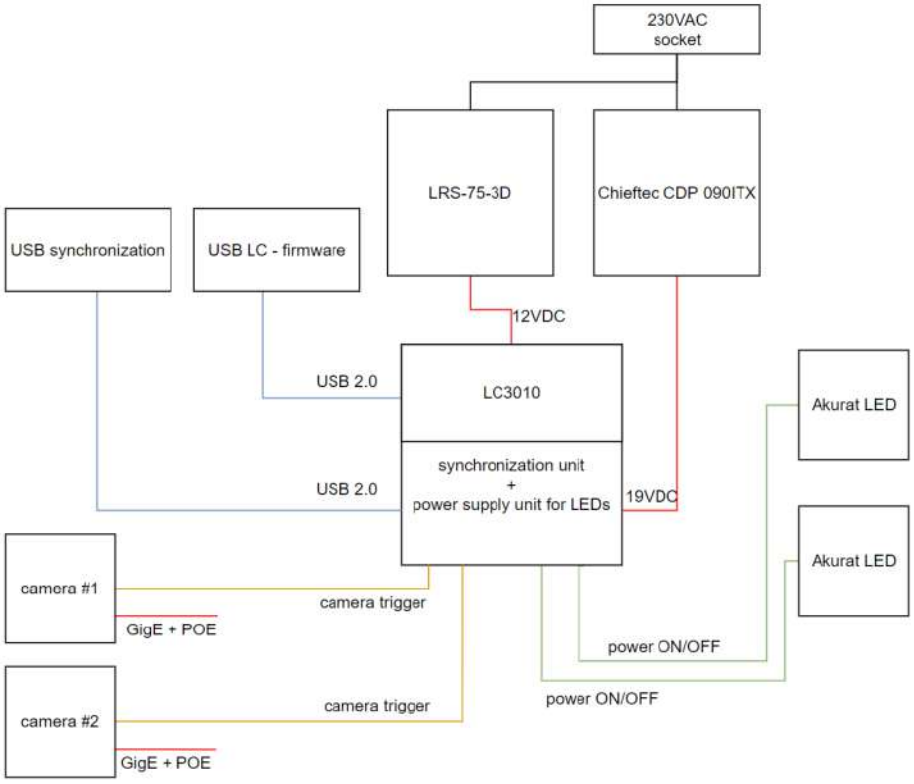

Figure 3.6: Electronic connections layout.

The electronic connection layout is presented in Fig. 3.6. The trapezoidal plug provides the 230VAC power supply. Cameras are powered by the POE switch and synchronized with the projector. The additional PCB on the projector, responsible for the synchronization and control of the LED panels, is powered by the external power supply Meanwell LRS-75-12. The power supply socket is equipped with a fuse (Fig. 3.5).

3.3 Multimodal Imaging System Prototype

The final prototype of the MIS system can be found in the following figure (Fig. 3.7). Its final weight is below 4kg and outside dimension: width: 620.00 mm, height: 246.50 mm and depth: 174.30 mm, the electric current supply: 230V AC. Additional components required for the operation which are not presented at the photos are the PoE switch and the computer. Control of the device for data acquisition can be achieved using any computer with Gigabit Ethernet compatible network adapter card, along with the operating software provided by the manufacturer of the projector and cameras and Termite serial port. Regarding the data acquisition procedure, the light patterns are stored into the memory of the projector, and then the acquisition parameters are configured through the serial port and camera software. The final trigger for the acquisition is sent via the cameras software. The total cost of the system (as for December 2021) is approximately 7000 euro including the purchase of the commercial components, electronics, and 3D printed parts. The developed MIS optomechatronic setup fully satisfies the requirement of portability and low cost and with this minimized hardware, it is ready to capture data required for SL, DIC and MSI modalities (Objective 1).

Figure 3.7: The photo of the MIS prototype.

This chapter contains parts of the paper Metrological evaluation of the demosaicking effect on colour digital image correlation with application in monitoring of paintings published in Sensors 2022 [92].

4 Imaging modalities

4.1 Imaging Modalities

This chapter presents the implementation of the selected modalities of the MIS for recording the surface appearance of 3D objects that exhibit scattering and mixed scattering/partially reflecting properties. The hardware configuration of the demonstrator has been thoroughly established in the preceding chapter. Consequently, this section is focused on the development and adaptation of the imaging modalities regarding the steps involved in data processing and merging. This chapter provides a detailed description of each modality's implementation, processing pipeline, and specifications, presented individually. The final section of this chapter is devoted to the methodology employed for merging the data.

4.1.1 Structured Light

This section is dedicated to the development of the SL modality of the MID. Using this modality allows for the retrieval of 3D shape of an object with high accuracy. The hardware config-

uration, along with the data capturing, has been described in Ch. 3.2, therefore this section is dedicated only to data processing implementation for the generation of the CoP. The SL modality allows for the acquisition of shape for scattering and quasi scattering objects with high accuracy in the form of point clouds.

Hybrid Projection Method

The implementation of this modality has been achieved for two methods, HP for single camera SL system, and graycode for stereo SL system. The HP method has been implemented using the OGX software of WUT, treating each camera-projector pair as an individual system, which comes with a user interface for the initialization of the calibration procedure and CoP generation. The multiframe recorded data, 16 frames in total which consist of the temporal phase shifting and graycode patterns, are required both for the calibration and the measurement procedure. The calibration is performed using a circular grid target (Fig. 4.1b), which is placed in six positions within the measurement volume (Fig. 4.1a). For every position, images are recorded for the full set of phase shift and graycode patterns. This process, needs to only be done once and then it can be used for multiple measurements, assuming that the geometrical configuration of the system and object is not changed.

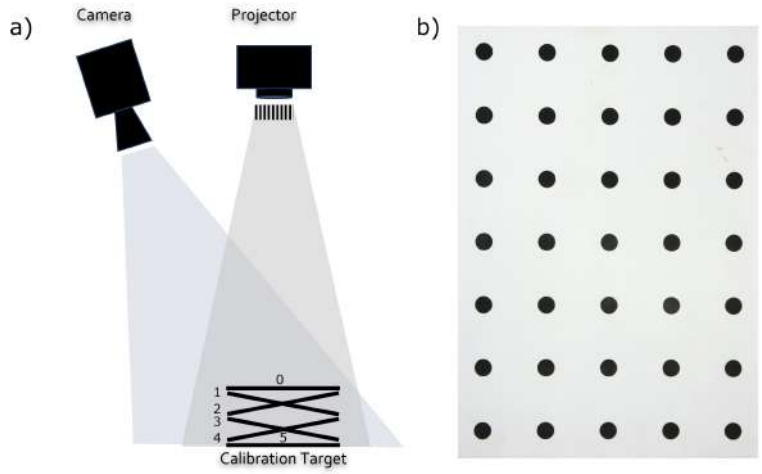

Figure 4.1: a) Schematic representation of HP calibration method, b) calibration target with symmetric circular grid.

For each camera- projector pair one calibration file is created, which contains all the necessary information regarding the calibration model and retrieval of the xyz coordinates from the phase and graycode images. Then, the measurement data can be uploaded to the

program for the generation of the 3D point clouds. This process is repeated for each camera-projector pair and two clouds are generated for the object (one from the left camera-projector SL system and one for the right). These clouds are not perfectly aligned and require the use of ICP method for fine registration, which can be done in a post processing step (i.e. in CloudCompare). This method can provide the maximum accuracy in terms of shape calculation, requires smaller amount of images and therefore results into faster measurements and it is also the most popular implementation utilized in academic and industrial SL systems.

Graycode Projection Method

The single camera-projector implementation with the HP method, is well established software written in C++ created over years of development in WUT for a variety of applications in CoP processing [154, 155, 156]. The accuracy of shape using this method is much better in comparison to graycode, nevertheless in the context of this thesis, it was not further modified to incorporate both of the system's cameras in a stereo mode and for the merging of the datasets. Instead, the graycode method was implemented utilizing both of the system's cameras, which also provides good coverage of the object's surface, by using available modules of OpenCV [157]. Within open source libraries, exist well-described solutions written in C++, while the necessary modules from the OpenCV contributions library are also available in Python. Therefore, the tutorial of stereo SL (sSL) written in C++ [158], was mainly followed for the Python implementation of the sSL graycode. The merging of the modality has been realized for the graycode method, and it remains for future work to extend the hybrid method into stereo mode.

Similarly to the hybrid method, a calibration file must be generated prior to the data processing. This is performed using a target with checkerboard pattern and multiple image pairs recorded within the MIS's measurement volume. The implementation is done in PyCharm environment using the available camera calibration OpenCV modules [157]. The calibration information is saved into a file, which contains the camera matrices for the left and right cameras, the rotation, translation, fundamental, and essential matrices, along with the distortion coefficients, the maps for the joint undistortion and rectification transformation of the data and the disparity to depth mapping matrix. The user input required for this script is the adjustment of the world scaling parameter, which denotes the size of the checkerboard squares, along with the number of checkerboard corners and the folder paths for the

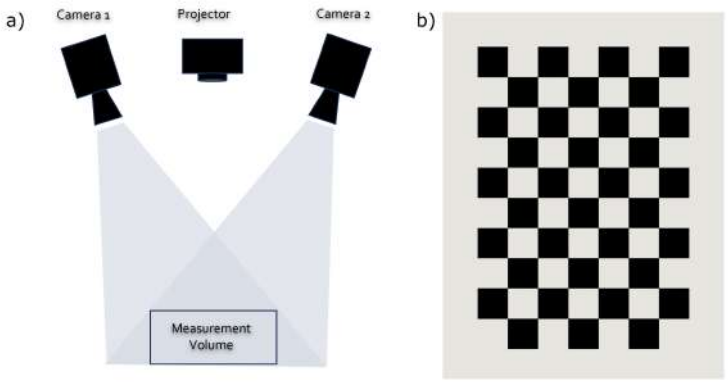

Figure 4.2: a) Schematic representation of stereo calibration setup, b) calibration target with checkerboard pattern.

calibration images captured by the left and right cameras. The transformations for achieving the undistortion and stereorectification of the SL data are also applied to the rest of the modalities datasets for the data merging process.

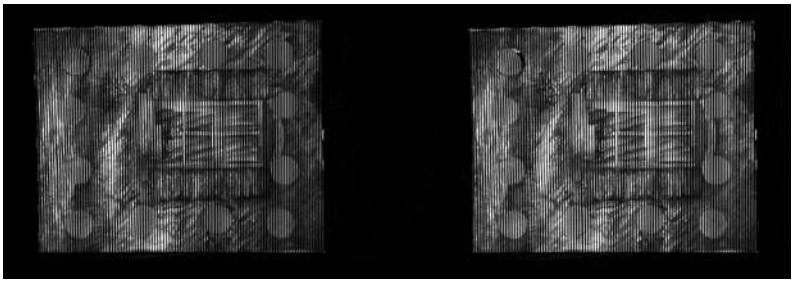

Figure 4.3: Exemplary stereo rectified data.

The graycode sSL implementation is in the form of a script that requires the user to specify the complete file path for the calibration file. Additionally, the user has to provide the directory that contains the recorded data for both cameras. The data should be separated into two folders named *right* and *left* and the image names should include the image number in the position preceding the file extension.

For the graycode method, 42 patterns are needed along with two images of homogeneous colour (black and white) for masking the analyzed area. Both cameras are recording the projected patterns simultaneously. The captured images from both cameras are processed to decode the Gray code. In the implemented script, the stereocalibration information are utilized for the undistortion and stereorectification of the images prior to the decoding of the patterns to achieve alignment of the epipolar lines. Additionally, the camera- projector correspondence is established both for the left and right sensors. Decoding involves identifying the position and correspondence of each projected pattern in the images. By comparing the

differences between adjacent patterns, the depth information can be derived. Once the Gray code decoding is performed, the depth information for each point on the object's surface can be calculated. Then the disparity map can be generated Fig. 4.4 and points are triangulated for the generation of the point cloud object, which is saved in *ply* format. Each point in the point cloud represents a point on the object's surface, with its (x, y, z) coordinates in the 3D space.

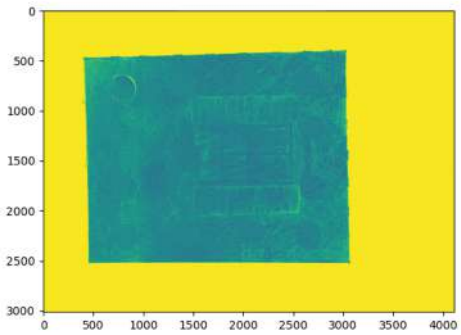

Figure 4.4: Exemplary disparity map.

The colour layer of the CoP comes from mapping the image recorded under white light illumination (using the Akurat LEDs of the MIS) on the CoP data based on their pixel position. To improve the colour representation, white balance correction is applied using the passport colourchecker and a custom script implemented in MATLAB. In order to minimize the data noise, an initial filtering process is employed. This involves the removal of statistical outliers, defined as points that significantly deviate from their neighbors in terms of distance compared to the average value within the point cloud. The outliers are determined taking into account the number of neighbours and the standard deviation of the average distances across the point cloud. The user can adjust these parameters in the Python script to either increase or minimize the extent of data filtering. In terms of the hardware and geometrical specifications, the system utilizes a 16mm lens and a minimum baseline of 40.3 cm, as illustrated in Fig. 3.3. The measurement volume is 43*35*20 (cm) (Fig. 4.2a) and the average point to point distance for the CoP data corresponding to Fig. 4.4 is approximately 0.14mm.

System Specifications VDI/VDE

The characterization of the system accuracy has been achieved following the VDI/VDE 2634 standards [159]. The guideline defines acceptance and reverification tests as well as artifacts

for the evaluation of optical 3D measuring systems regarding its accuracy. The guideline applies to optical 3D measuring systems based on area scanning, whose function is based on triangulation and applies to the measuring of three-dimensional objects in multi views. The artifact used for the accuracy determination, guidelines and processing software was provided by SMARTTECH3D measuring company. The calibration artifact consists of two spheres with known radius and center distance Fig. 4.5a. In order to determine the accuracy of the system the target was measured in seven positions within the measurement volume (Fig. 4.5b).

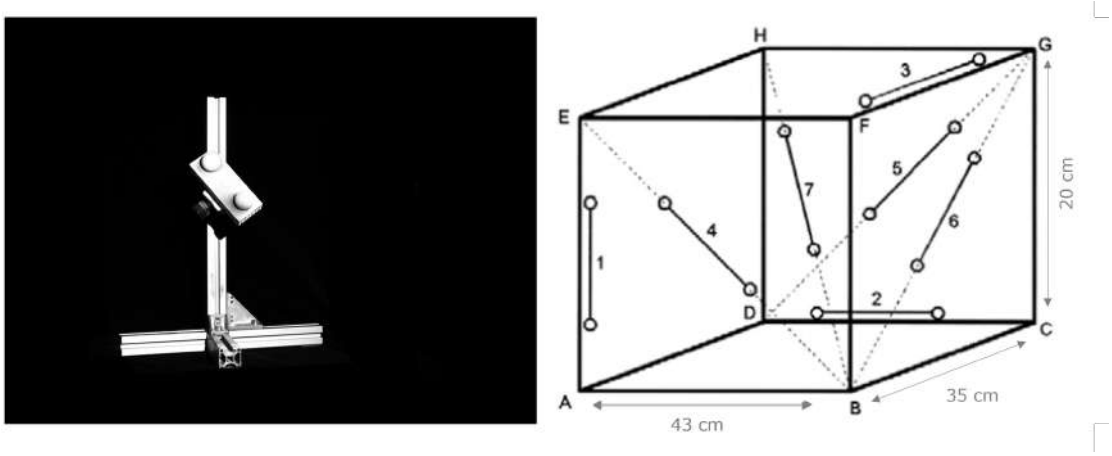

Figure 4.5: a) The SL calibration target with the holder and b) localizations of the target as required by VDI/VDE 2634 standard.

For each position and sphere the best fitting sphere has been estimated using SMARTECH 3Dmeasure software. From the cloud only the background information was removed, while the spheres were not subjected to any additional point elimination. For the purposes of these measurements filtering and outlier removal during the CoP generation was also eliminated. Once the cloud is obtained, the points corresponding to the sphere are selected and the best fitting sphere is calculated from the recorded partial shape Fig. 4.6. In this way, the radius (R) and the center of each fitted sphere is retrieved for every position within the measurement volume. From the radius the deviation from the certified sphere diameter is calculated (ΔD), which for the target used herein is 25.0017 mm ±0.0001 mm. Similarly, the distance between the center of the spheres is calculated (L), along with it's deviation (ΔL) from the known center distance, which is 68.6142 mm. The system accuracy is determined as the maximum recorded error among (ΔL) and ΔD) for all 7 positions, therefore for the MIS developed it is 80 μm.

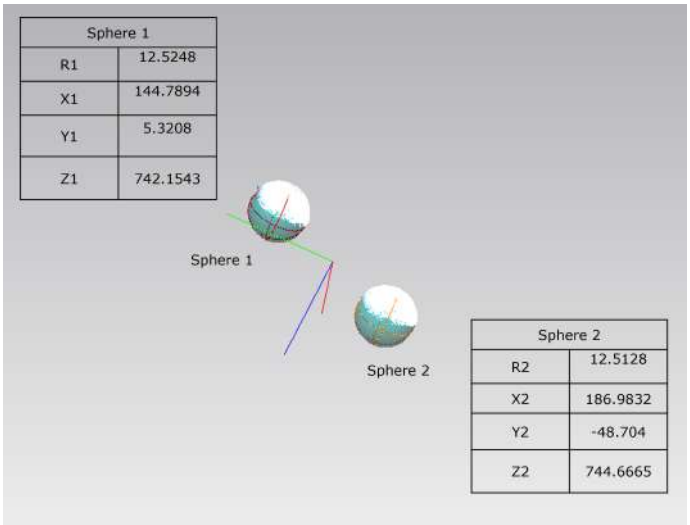

Figure 4.6: Exemplary sphere fitting from position 4.

Table 4.1: The results obtained from the MIS's sSL accuracy tests

Pos.	R1 (mm)	D1 (mm)	ΔD1 (μm)	R2 (mm)	D2 (mm)	ΔD2 (μm)	L(mm)	ΔL(μm)
1	12.5247	25.0495	47.7900	12.5292	25.0585	56.7980	68.6937	**79.5000**
2	12.5022	25.0043	2.6200	12.4763	24.9525	49.1940	68.5502	63.9666
3	12.4771	24.9542	47.4560	-	-	-	-	-
4	12.5248	25.0496	47.8980	12.5128	25.0257	23.9560	68.5952	18.9602
5	12.5124	25.0249	23.1880	12.5102	25.0204	18.7480	68.5714	42.7755
6	12.5015	25.0030	1.2680	12.4989	24.9979	3.8100	68.6379	23.6567
7	12.5028	25.0056	3.8820	12.5409	25.0817	80.0100	68.6689	54.6835

4.1.2 3D colour Digital Image Correlation.

3D DIC Calibration and analysis

For the realization of 3D DIC measurements a pair of cameras in stereo configuration is required as described in Ch. 2.3, which has been implemented using hardware of Fig. 3.3 (16mm lens, 40.3 cm baseline). Similarly to SL prior to any measurement or monitoring session, calibration of the system is needed. The calibration target depends on the software used for the DIC analysis, which for the purposes of this thesis is VIC 3D-7 from Correlated Solutions [85].The calibration is achieved using a circular grid target with 3 distinct markers, required by the VIC software, and capturing pairs of images within the measurement volume.

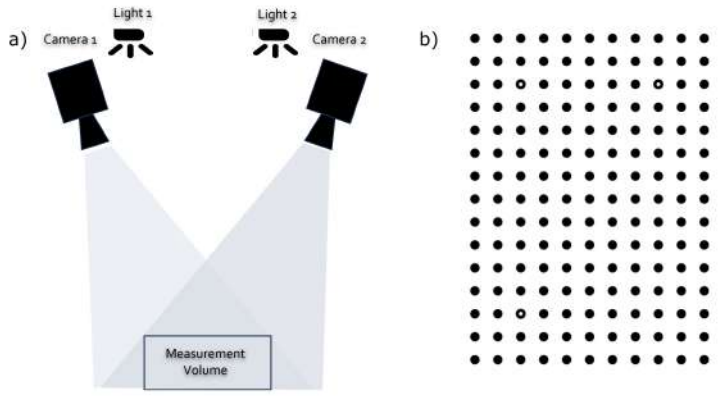

Figure 4.7: a) Schematic representation of DIC stereo calibration setup, b) calibration target with circular grid and special markers needed for VIC 3D-7 software.

A good calibration can be achieved with minimum 15 pairs of images but it is generally advised to capture around 30. The same target is compatible with the open source DICe software, while the DuoDIC of MATLAB requires checkerboard target. Pairs of images must be recorded simultaneously by both cameras for the analysis to be feasible and accurate, both for the calibration and the monitoring session. The input data naming must be zero padded and in the format ImNumber_CamNumber.extension, with compatible extensions being *tiff*, *png*, *bmp*. For the analysis the user must select subset and step size in pixels, thresholding options, correlation coefficient criterion and spline interpolation number. For the calculation of strain the virtual extensiometer gauge needs to also be selected in the form of pixel size. The output data contain for the AOI are the real world coordinates (X, Y, Z), the displacements (U,V, W) in mm, the disparity map with respect to the reference image as well as between the two cameras, the correlation coefficient value and the strains (exx, eyy, exy). The preferred output format in this work is mat file, and the data are sampled within a regular grid using the step size selected for the analysis. By default everything is calculated for the coordinate system of the left camera of the MIS.

3D colour DIC

As mentioned in Ch. 2.3.2 the classical implementation of 3D DIC requires covering of a surface with artificial, random texture. In some cases, the natural inherent texture of an object formed, i.e., by brush strokes and discolourations or intensity and colour variations, might be sufficient. While in other cases this far from the ideal speckle pattern is making the application of DIC a challenging, or impossible, task. Therefore, this section is dedicated to

the developed of a novel processing path which utilizes the colour information to increase the cDIC metrological performance for the measurement of objects with natural texture. In addition, multiple demosaicking algorithms have been evaluated in terms of metrological accuracy both for traditional and the developed processing pipeline. The analysis and experiments presented herein, in contrast to the other works devoted to cDIC, are dedicated to the monitoring of objects with natural colour texture, which fulfil the requirements posed for cultural heritage objects. The best approach is selected based on the minimisation of the calculated displacements errors in order to have the maximum possible accuracy.

Presently, there are three approaches in the DIC analysis of images originating from CFA cameras. For a single channel output (monochrome), the correlation and displacement maps are directly calculated (Fig. 4.8, grey path). colour images are typically converted into grayscale using linear conversion and then used as input data for DIC analysis (Fig. 4.8, green path). An alternative is to analyse each colour channel separately. In this case best results are expected from the green channel (Fig. 4.8, orange path), due to the double pixel number compared with red and blue channels. However it was noticed that the red and blue colour channels can provide additional information in the case of natural texture objects, which in turn can enable higher local correlation accuracy. Therefore the modified cDIC method was proposed, which utilizes simultaneously R, G, B channel data. Additionally, the influence of the demosaicking methods used for the interpolation of the full colour channels should be taken into account, as it has also a direct impact to the correlation quality [90, 91, 97, 160]. For this reason an extensive list of demosaicking methods has been tested along with the proposed processing pipeline in terms of metrological accuracy.

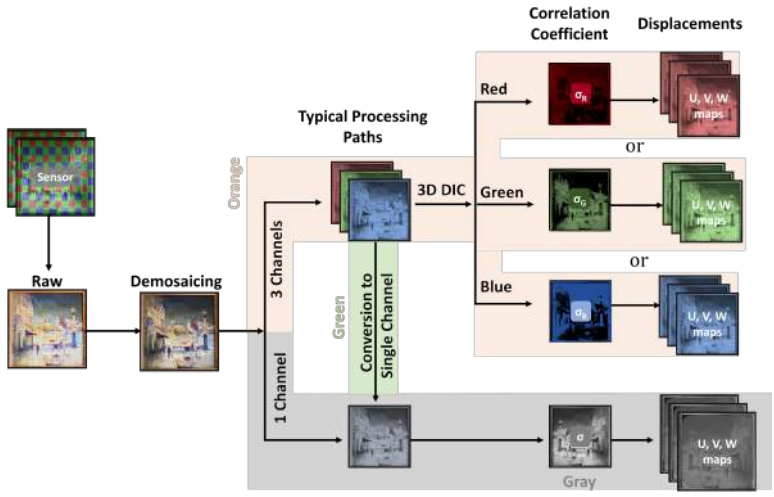

Figure 4.8: Schematic representation of different options for data processing path for cDIC.

Modified colour DIC

colour digital images are made of pixels, corresponding to one of the three primary colours red, green and blue. Each channel is the grayscale representation of a single primary colour and therefore is contains different speckle pattern distribution. This is attributed to the local scattering phenomena connected to the material properties, which varies as a function of the incident illumination wavelength. Fig. 4.9 illustrates well the different colour texture in the R, G, B channels.

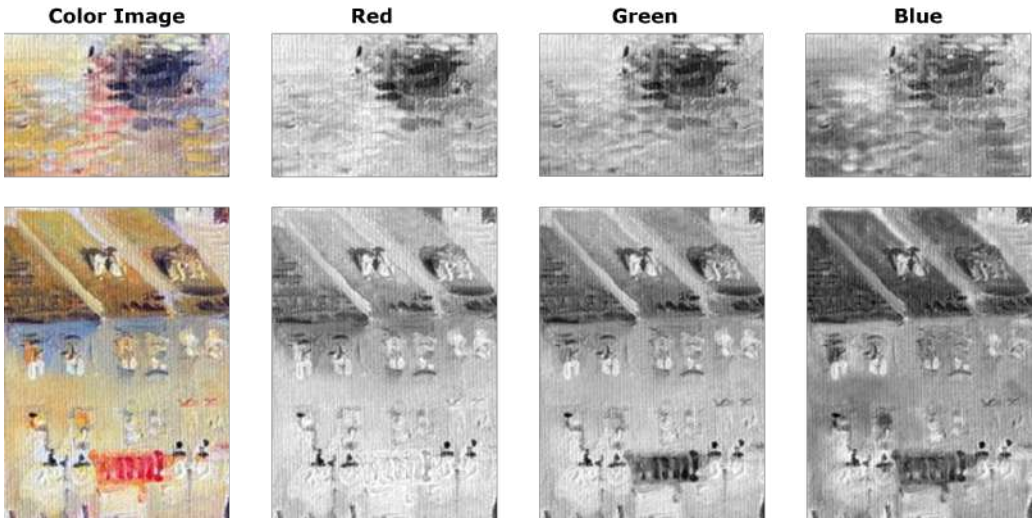

Figure 4.9: colour Image (left) and primary channels for object with natural texture.

This feature creates the basis for the modified processing path proposed for cDIC (Fig. 4.10). With the aim to utilise the information from all the colour channels, and subsequently to locally improve the results, an alternative processing approach was developed. Initially each colour channel is analysed using the standard processing path for monochrome data.

Then the local optimum sigma values at each pixel position are combined to construct a merged sigma map (σ_M) and merged U_M,V_M,W_M displacement maps according to Equations (4.1) and (4.2).

$$\sigma_M(x,y) = min(\sigma_{R \vee G \vee B}(x,y)) \tag{4.1}$$

for each (x, y) pixel position and the displacements are

$$U_M(x,y) = U(x_k,y_k), \quad V_M(x,y) = V(x_k,y_k), \quad W_M(x,y) = W(x_k,y_k) \tag{4.2}$$

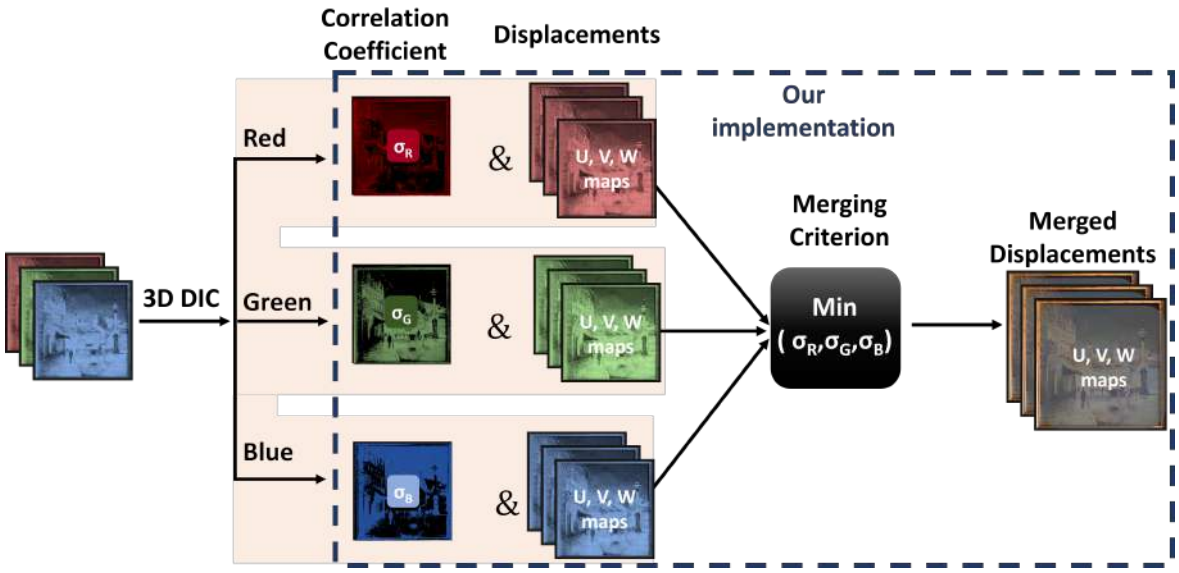

Figure 4.10: Schematic representation of the developed merged data processing path for cDIC.

where

$$k = \begin{cases} R & \text{if} \sigma_M(x,y) = \sigma_R(x,y) \\ G & \text{if} \sigma_M(x,y) = \sigma_G(x,y) \\ B & \text{if} \sigma_M(x,y) = \sigma_B(x,y) \end{cases}$$

The merged maps with the minimum sigma value (and therefore with the best quality of texture) are generated by combining the retrieved information from the channel with the optimum correlation at each analysed pixel position.

Regarding the implementation, each colour image is separated to the primary colour channels and analysed using VIC 3D-7 using the same parameters (subset, step size, thresholds, AoI) [85]. The data are then exported to *mat* format, using the letter r,g, b at the beginning of the filename to denote the origin channel. Finally, the data merging pipeline has been developed in Matlab in the form of script and requires from the user to declare the folder containing the output 3D DIC files.

Demosaicking Methods

Colour image demosaicking plays a crucial role in producing high-quality colour imagery from a single-sensor camera. The demosaicking processing aims to reconstruct a full-colour image from the acquired mosaicked image by estimating the values of the two missing colour components at each pixel position. Subsequently, demosaicking quality influences directly the DIC analysis and under this context a number of demosaicking approached were inves-

tigated with the aim to select one that enables high quality DIC analysis. Based on the existing research [97, 161, 96] two approaches of demosaicking algorithms were investigated: a general two-dimensional interpolation and specialised algorithms developed for colour reconstruction from Bayer pattern. These approaches are represented by five groups of demosaicking methods (Table 4.2). The methods representative for these approaches and selected for further investigation are listed in detail in Table 4.3

The data processing path varied depending on the number of output channels for each method. Single channel data did not require processing outside the typical DIC pipeline (Fig.4.8, grey path). Multichannel data were analysed using the modified procedure for the merged displacement fields based on the optimum of local correlation (Fig. 4.10). The only exception is Basler PGI method, which despite being a colour image was additionally converted to monochrome one for the analysis (referred to as rgb2gray Basler for the single channel and merged Basler for the multichannel data). The reason behind this deviation in the processing approach is purely ergonomically as this would be the typical path for fast cDIC calculations.

The evaluation of the demosaicking performance in cDIC is performed at two stages of data processing:

- at the level of correlation Coefficient (Sigma) analysis through (i) the local distribution and (ii) the mean value (<sigma>) and its standard deviation (<std>)

- at the level of evaluation of demosaicking influence through the RMSE, mean value and P/v amplitude of residual displacement maps obtained by subtraction of the best fitted linear plane

Samples

For the purposes of this analysis three sample were prepared. The first one is a mock-up painting ('*Mock-up*' for the rest of this chapter), and two oil paintings named '*Flower*' and '*Street*' (Fig. 4.11). *Mock-up* represents random DIC speckle pattern, while the paintings objects with natural texture. *Mock-up* was prepared on a white canvas at which a texture was created by the application of acrylic colours from Liquitex. The average surface roughness (local shape) is 0.003 mm for the *Mock-up*, 0.012 mm for the *Street* and 0.023 mm for the *Flower*.

Table 4.2: Demosaicking Groups

Group No.	Method	Description
G0	Baseline	The monochrome baseline method [162] involves estimating the luminance of a pixel by utilizing colour information from the nearest pixels on the colour filter array. It is referred to as Monochrome throughout the remainder of this document. At the colour baseline format the pixel data are processed using the method listed in [163]. Then, linear interpolation is used for the conversion to monochrome images (referred to as rgb2gray Basler for the remaining of this work to differentiate it from Monochrome).
G1	Bilinear Combined with Dimensionality Reduction	Separate colour channel bilinear interpolation. The simplest way to restore the missing values is to interpolate each channel separately using neighbouring values. This method is efficient, but images would have colour artefacts at the edges [164]. Two dimensionality reduction operations were performed in methods belonging to G1 and G2 utilizing: • Principal components analysis (PCA) which is a statistical technique that identifies the vector along which the variance is maximized.; • Independent component analysis (ICA) which is a computational method used to identify and extract the vectors that correspond to mixed signals.
G3	Homogeneity in decision procedures and directed interpolation	These algorithms generate two or more estimation candidates for each missing component, and the best one is chosen a posteriori. Adaptive homogeneity interpolation (AHD) and adaptive residual interpolation (ARI) are two of the well-known methods [165]. A trio of approaches are used by AHD to reduce errors in colour reconstruction. Aliasing is reduced by the the filter bank approach. Colour artifacts are minimized by the adaptive selection of the interpolation direction . Finally, a homogeneity matrix which combines vertical and horizontal interpolation is utilized for the elimination of interpolation artifacts. Two residual interpolation-based techniques are combined adaptively by ARI, which also modifies the number of iterations for each pixel [166]. Although undocumented, the PPG, AAHD, DHT, and DCB algorithms all belong to the same group[167].
G4	APN (Attention Pyramid Network)	This approach is based on a single pyramid attention mechanism [168]. In this approach two main processes are utilized for the minimization of artifacts. The first process addresses the impact of the aliasing effect using non-local attention. The second mechanism is improving the quality of the detail reconstruction by scale-agnostic attention. The pyramid attention is implemented using convolution and deconvolution operations. The patches are extracted from the transformed feature map to a deconvolution over the matching score.

Experimental Details

For the feasibility of the metrological evaluation of the developed approach controlled displacements were introduced on the objects in the form of linear shifts in the x (in plane)

Table 4.3: Demosaicking methods

Group No.	Method	Interpolation Type	Channel No.	Computational Complexity
0	Baseline monochrome-Basler (Monochrome)	Nearest neighbour	1	Small
	Baseline demosaicking-Basler	PGI	3	Small
1	Bilinear ICA	Bilinear	1	Mid
	Bilinear PCA	Bilinear	1	Mid
2	EA ICA	Edge adaptive bilinear	1	Mid
	EA PCA	Edge adaptive bilinear	1	Mid
	VNG ICA	Gradients + bilinear	1	Mid
	VNG PCA	Gradients + bilinear	1	Mid
3	PPG	Adaptive	3	High
	AHD	Adaptive	3	High
	AAHD	Adaptive	3	High
	DHT	Adaptive	3	High
	ARI	Adaptive	3	High
4	APN	Deep learning	3	High

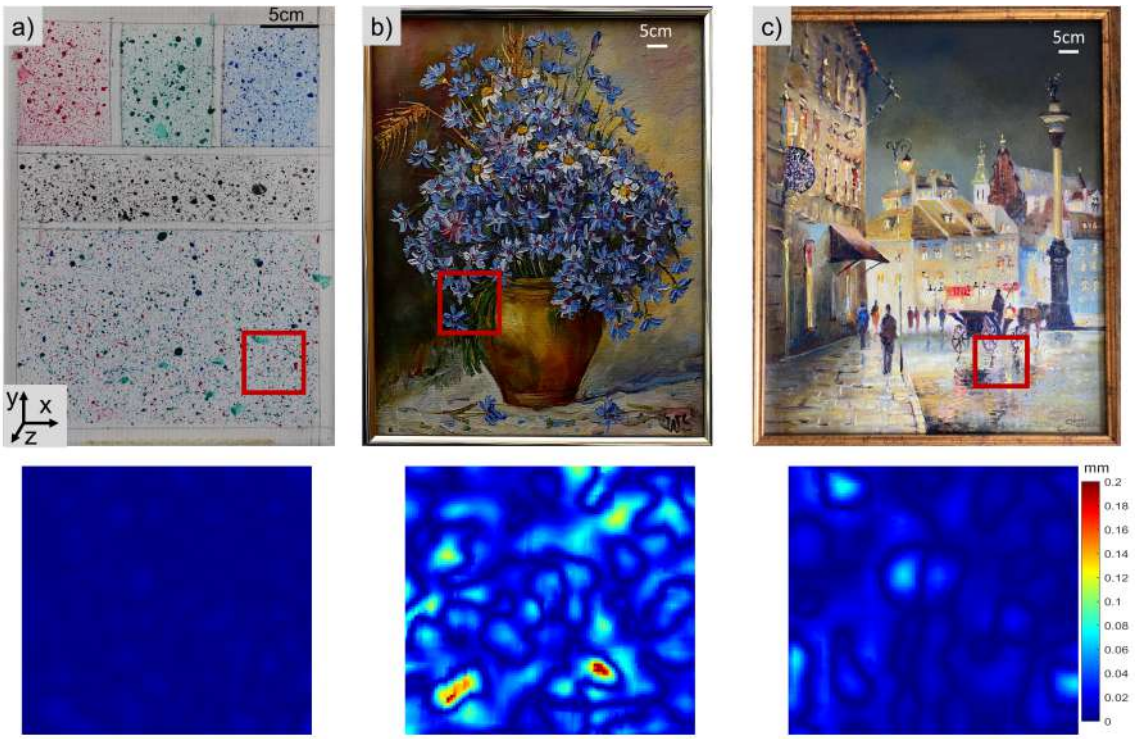

Figure 4.11: Samples (a) Mock-up with random artificial texture, and the oil paintings (b) Flower and (c) Street; (d) the local maps of roughness in the example areas denoted at the samples with red rectangles.

and z (out of plane) axes. For that purpose the objects were positioned on a linear translation stage. A sequence of images was acquired subsequent to mechanical translations that corresponded to a displacement in the x-direction with a step size of 1 mm. Following the completion of 10 sequential x-shifts, the samples were additionally shifted in the z-direction for 5mm, again with step size of 1 mm. Data were recorded using Basler RG8 pixel in raw & tiff format. DIC analysis was conducted using subset of 105 pixels, and step size of 7 pixels in

VIC 3D-7 software for all objects. Finally, the selected DIC threshold values were : 0.02 pixels for the consistency threshold, 0.05 pixels for the confidence margin and a 0.1 maximum pixel margin.

Correlation Coefficient Analysis

Sigma values are linked with the accuracy of the calculated displacements and therefore can reveal the propagation of the combined errors originating from the demosaicking and correlation processes. Correlation errors should be in principle equal across the demosaicking methods as the analysis parameters are the same, therefore any deviation can be attributed to the demosaicking process. Therefore, the mean sigma and it's standard deviation obtained for demosaicking methods listed in Table 4.3 are compared. In Fig. 4.12 these values are presented for two known translations of the *Mock-up*. The first graph corresponds to $X5 = (5 \pm 0.1)$ mm, while the second one to a combined shift in the x and z directions $XZ5 = X5 + Z5$, where $Z5 = (5 \pm 0.1$ mm). As indicated in Fig. 4.12 the merged APN method (G4) provided the minimum sigma values, while acceptable were also results from Baseline methods of G0 (monochrome and rgb2gray) considering the low computational complexity. These cases represented both a potential improvement and the option of performing cDIC fast and with a low computational complexity. It is also confirmed in Fig. 4.13a-c, where the maps of sigma values for different demosaicking methods are presented.For the methods with high sigma (Merged AHD, VNG ICA and PCA) correlation was locally lost, resulting in non-homogeneous displacement maps (Fig. 4.13d).

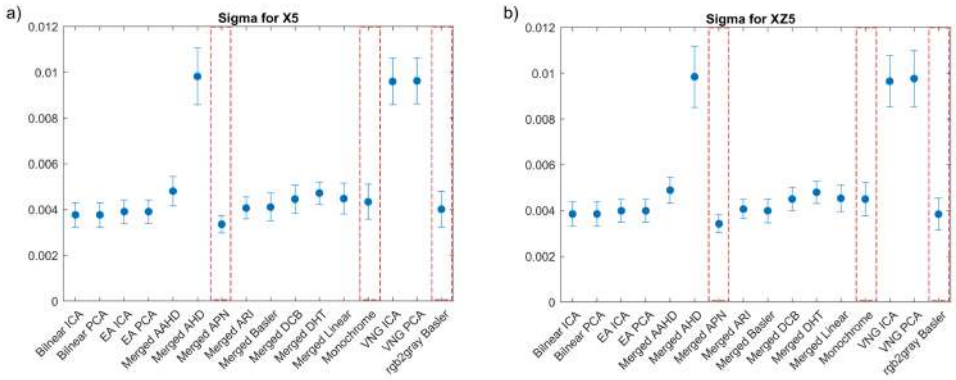

Figure 4.12: Mean correlation coefficient (sigma) and standard deviation values as calculated for (**a**) X5 shift and (**b**) XZ5 shift. Red boxes indicate the selected methods.

The paintings were utilized to determine the methods which require further investigation for metrological evaluation. As depicted in Fig. 4.14, both paintings exhibit an increase in the

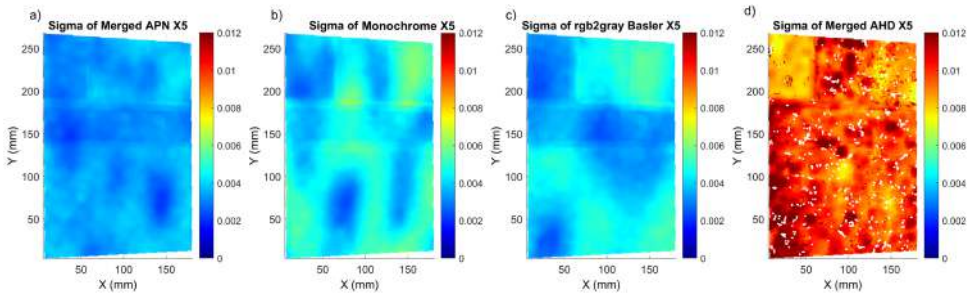

Figure 4.13: Correlation coefficient (sigma) maps corresponding to X5 shift for: (a) merged APN, (b) Monochrome, (c) rgb2gray Basler and (d) merged AHD methods.

mean sigma and its standard deviation values.

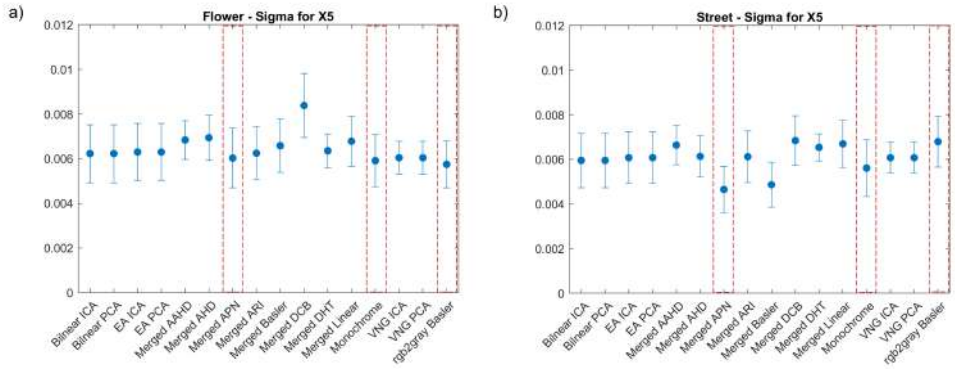

Figure 4.14: Mean correlation coefficient and standard deviation values as calculated for: (a) *Flower* and (b) *Street* paintings. Red boxes indicate the selected methods.

The observed increase can be attributed to the local variation in texture quality, as evidenced by the sigma distribution maps depicted in Figs. 4.15 and 4.16. The merged APN method yielded optimal outcomes, characterized by the lowest standard deviation, for the Street variable. In relation to the *Flower* dataset, it was observed that the rgb2gray Basler and the monochrome method exhibited the lowest sigma values. Additionally, the merged APN method resulted in an outcome that was comparable to the aforementioned techniques.

Low sigma values are detected in the center of *Flower* where the natural texture is more prominent (Fig. 4.15). *Street* is the painting showing bigger sigma variations for the tested demosaicking methods, with the best results detected for the merged APN method. For the comparison of the developed pipeline with the classical approach, the sigma maps of merged Basler method are also presented (Fig. 4.17). The sigma distribution of the merged Basler compared to rgb2gray Basler (Figs. 4.13, 4.15, 4.17) is improved for *Mock-up* and *Street*. For the *Flower* the optimum correlation map is detected for rgb2gray Basler, probably due to it's high surface roughness. Therefore, the developed approach in combination with the APN

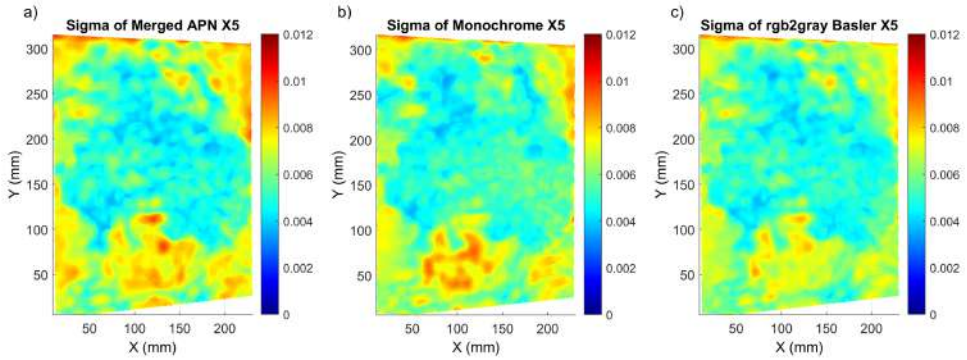

Figure 4.15: Sigma distribution for the *Flower* painting corresponding to the X5 shift for the (a) merged APN, (b) Monochrome and (c) rgb2gray Basler methods.

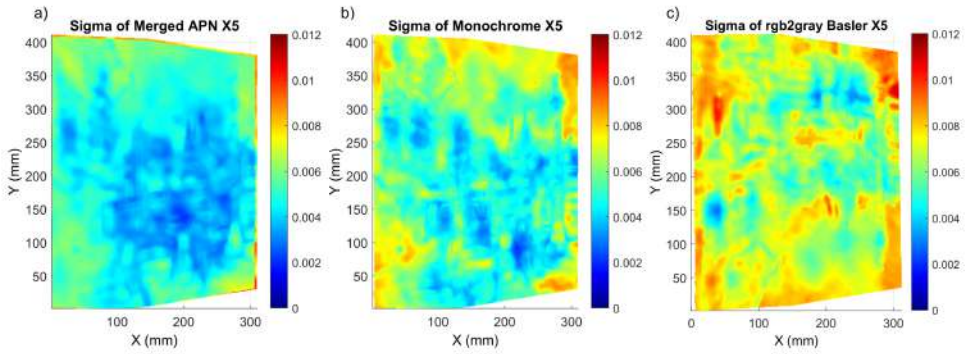

Figure 4.16: Sigma distribution for the *Street* painting corresponding to the X5 shift for the (a) merged APN, (b) Monochrome and (c) rgb2gray Basler methods.

method, is the one improving the correlation the most.

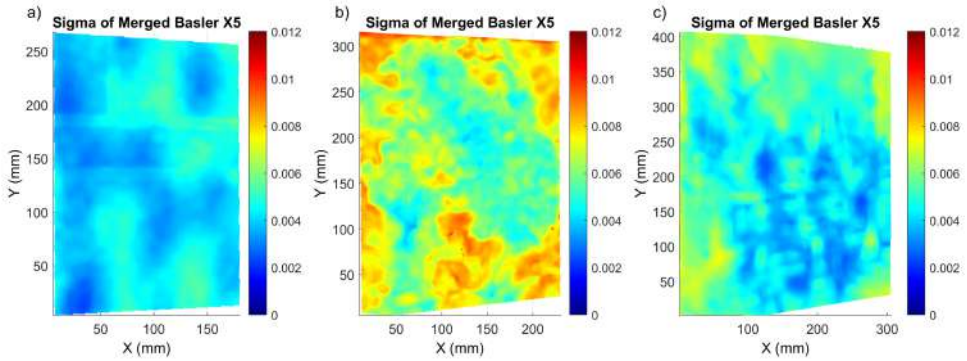

Figure 4.17: Sigma distribution for the merged Basler method for a) *Mock-up*, b) *Flower* and c) *Street* corresponding to the X5 shift.

Evaluation of Demosaicking Influence on Displacement

The influence of demosaicking methods on sigma directly and of course on the distribution of the image intensity, will generate errors in the resultant displacement maps. To inves-

tigate distribution of theses errors in the field of view the residual error maps of selected displacements were calculated. Given that the controlled displacements introduced on the objects were linear, displacement maps were plane fitted using linear regression method. The constant (mean displacement) and linear (tilt) terms were subtracted from the actual displacement map the residual evaluation was performed for the displacements calculated for the demosaicking methods that yielded the best results (merged APN, Monochrome and rgb2gray Basler). For consistency purposes the maps for displacements steps X5 and XZ5 and the addition of $X10 = (10 \pm 0.1)$ mm.

Mock-up is the first object to be examined towards the metrological evaluation of the proposed cDIC processing path. In Fig. 4.18 the residual displacement error (referred to as Residual for the rest of the chapter) is presented for step X5 of the selected methods. Minimization of the residual amplitude is achieved for Merged APN method, while it's maximized for the Monochrome. Further proof for the efficiency of the proposed method is provided in Table 4.4, where the evaluation metrics corresponding to the selected methods for 3 steps are presented. In specific merged APN results into minimum average sigma and P/V amplitude of the residual for all the steps, thus achieving the minimum propagation of the combined interpolation and bias error. RMSE and mean of residual are comparable between the investigated demosaicking methods. The quasi-sinusoidal modulations present at the residual maps are attributed to errors associated with interpolation bias. The periodicity and amplitude of the interpolation bias errors varied across the methods due to the different quality of demosaicking and associated artifacts.

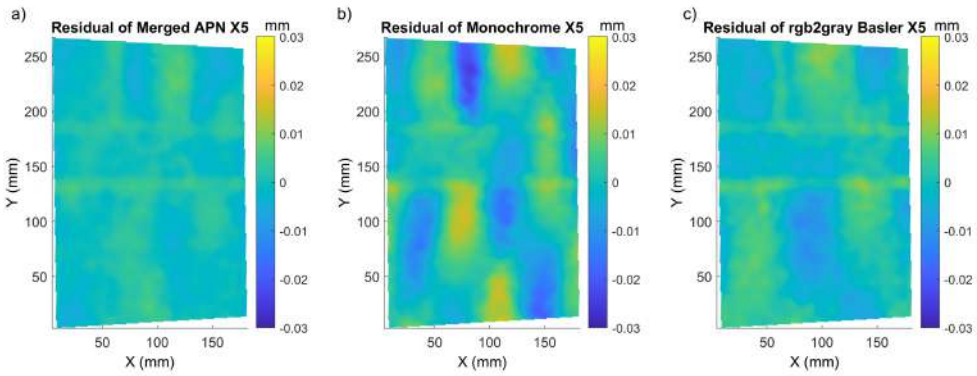

Figure 4.18: X5 residual displacement maps of *Mock-up*, for: (a) merged APN, (b) Monochrome and (c) Basler converted to monochrome.

The evaluation approach followed for the *Mock-up* was repeated for the *Flower* and *Street* paintings. Again the P/V residual amplitude is minimum for the Merged APN method,

Table 4.4: Demosaicking evaluation for *Mockup*

Method and Shift	<Sigma> (NN)	RMSE Res. Disp. (mm)	<Res. Disp.> (mm)	P/V Res. Disp. (mm)
Merged APN X5	0.0034 ±0.0004	0.0203	0.00005 ±0.00246	0.009
Mononochrome X5	0.0043±0.0008	0.0215	-0.00020 ±0.00725	0.031
rgb2gray Basler X5	0.0040 ±0.0008	0.0164	-0.00002 ±0.00221	0.02
Merged APN X10	0.0033±0.0004	0.0311	0.00003 ±0.00226	0.007
Mononochrome X10	0.0044 ±0.0008	0.0319	0.00001 ±0.00713	0.033
rgb2gray Basler X10	0.0038 ±0.0007	0.0304	0.00004 ±0.00199	0.018
Merged APN XZ5	0.0034±0.0004	0.0322	-0.00006 ±0.00182	0.009
Mononochrome XZ5	0.0045 ±0.0007	0.0329	-0.00006 ±0.00666	0.034
rgb2gray Basler XZ5	0.0039 ±0.0007	0.0320	-0.00001 ±0.00379	0.019

as confirmed both by the residual maps in Figs. 4.19 and 4.20 and the P/V residual amplitude (Tables 4.5 and 4.6). The residual modulation is not similar for all paintings, which can be the result of the different natural texture of the object affected further both from the interpolation bias and the demosaicking method. For the *Flower* the lower correlation values are recorded for Monochrome but the RMSE and the P/V residual amplitude are lower for merged APN. In the case of Street painting the minimum overall values are recorded for merged APN, which further enhances the claim that this method improves the cDIC calculations for CHOs with natural texture.

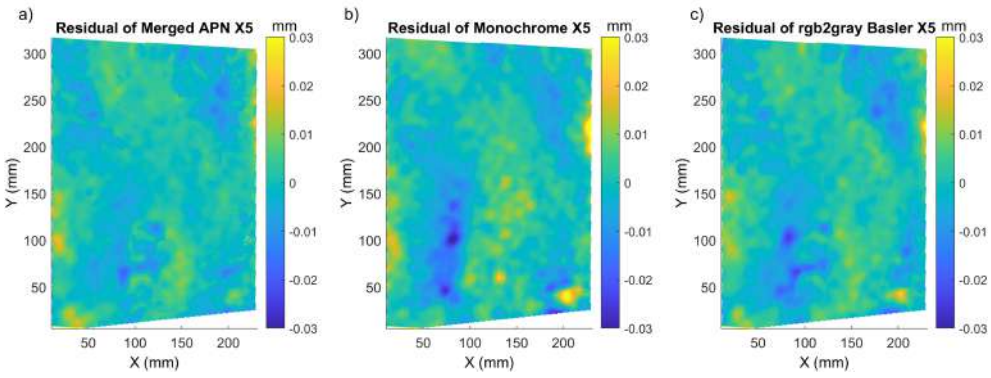

Figure 4.19: X5 residual displacement maps of *Flower*, for: (a) merged APN, (b) Monochrome and (c) Basler converted to monochrome.

Table 4.5: Demosaicking evaluation for *Flower*

Method and Shift	<Sigma> (NN)	RMSE Res. Disp. (mm)	<Res. Disp.> (mm)	P/V Res. Disp. (mm)
Merged APN X5	0.0060±0.0013	0.0117	0.00061 ±0.02405	0.019
Monochrome X5	0.0059±0.0012	0.0124	0.00048±0.02461	0.039
rgb2gray Basler X5	0.0057±0.0011	0.0121	0.00041±0.02430	0.035
Merged APN X10	0.0062±0.0013	0.0294	0.00477±0.20020	0.026
Monochrome X10	0.0064±0.0012	0.0299	0.00303±0.14069	0 .034
rgb2gray Basler X10	0.0060±0.0012	0.0296	0.00307±0.14033	0.031
Merged APN XZ5	0.0062±0.0013	0.0287	0.00331 ±0.14141	0.027
Monochrome XZ5	0.0065±0.0011	0.0291	0.00329 ±0.14147	0.046
rgb2gray Basler XZ5	0.0060 ±0.0011	0.0290	0.00317±0.14151	0.039

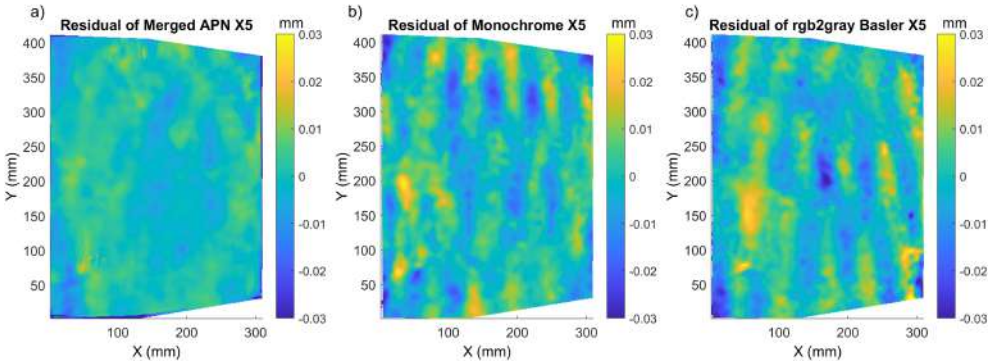

Figure 4.20: X5 residual displacement maps of *Street*, for: (a) merged APN, (b) Monochrome and (c) Basler converted to monochrome.

Table 4.6: Demosaicking evaluation for *Street*

Method and Shift	<Sigma> (NN)	RMSE Res. Disp. (mm)	<Res. Disp.> (mm)	P/V Res. Disp. (mm)
Merged APN X5	0.0047 ±0.0010	0.0208	-0.00014 ±0.00438	0.017
Mononochrome X5	0.0056±0.0013	0.0381	-0.00012 ±0.00773	0.039
rgb2gray RGB X5	0.0068±0.0011	0.0385	-0.00010 ±0.00820	0.049
Merged APN X10	0.0047±0.0010	0.0655	0.00051 ±0.02149	0.017
Mononochrome X10	0.0057±0.0012	0.0759	-0.00042 ±0.00893	0.041
rgb2gray RGB X10	0.0069±0.0011	0.075	-0.00062 ±0.00964	0.057
Merged APN XZ5	0.0047 ±0.0011	0.0541	0.00070 ±0.03299	0.027
Mononochrome XZ5	0.0058±0.0012	0.0617	-0.00043 ±0.01043	0.034
rgb2gray RGB XZ5	0.0069±0.0011	0.0634	-0.00071 ±0.01059	0.065

cDIC data processing flowchart

Considering the results from the metrological evaluation of demosaicking on cDIC, it is clear that the developed merged processing pipeline can improve the correlation quality and therefore the efficiency of the displacement calculation for objects with natural texture. The drawback of this methodology is that it requires higher processing time and it's computationally expensive in comparison to the typical approach. Before using the processing pipeline and

the demosaicking method with the optimum results both the objective of the measurement and the processing time need to be taken into consideration. To help the user make the decision as to which processing path should be followed, the flowchart shown in Fig. 4.21 has been created.

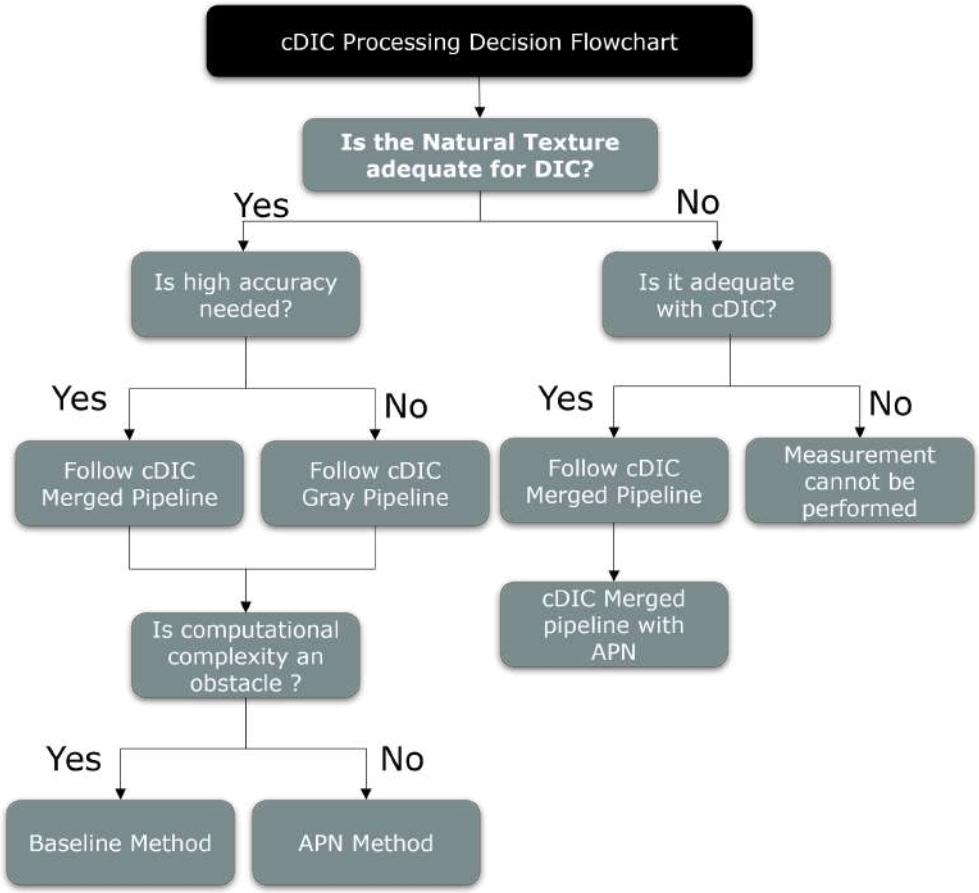

Figure 4.21: Data processing flowchart for cDIC.

4.1.3 Multispectral Imaging

This section is dedicated to the development of the Multispectral Imaging (MSI) modality of the MIS. The modality which offers a low-resolution multispectral imaging using five spectral bands within the visible range of the spectrum has been developed in collaboration with Prof. S. George, Prof. A. Suneel Sole and Dr. G. Trumpy at the Colourab of NTNU in Gjovik. The multispectral experimental setup was realized by utilizing the hardware described in Ch. 3.2. The main concept relies on the combination of the camera sensitivity functions and the spectral power distribution (SPD) of the light sources of digital projector. Of course, there are multiple commercial solutions that can offer much higher spectral data resolution, such as MSI and HSI cameras, but they were not considered for the MIS as they compromise the

mechanical stability of the system or significantly increase the cost. For this custom MSI implementation, the two cameras are recording a series of pair of images, while the object is sequentially illuminated with each of the projector LEDs. The CFA of the camera substitutes the bandpass filter that would be typically met in an MS camera setup, which combined with the narrow SPD of the LEDs results in images of well defined spectral bands, always assuming dark room conditions during the measurement.

Mathematical Description of Sensor Sensitivity and Spectral Reconstruction

Images captured using colour cameras record light information in digital values [0 225] for each of the individual camera channels (R, G and B). The response of the camera for every given pixel is defined as [169]:

$$C_k^j = \sum_i E(\lambda_i) R_j(\lambda_i) Q_i(\lambda_i) \Delta\lambda + n_k \tag{4.3}$$

where, C_k^j is the sensor response for thek^{th} channel (R, G, B) for j^{th} pixel,n_k is noise in channel k, Q_k is the spectral sensitivity function for the k sensor channel,$E(\lambda)$ is the spectral power distribution of the illuminant, $R_j(\lambda)$ is the spectral reflectance of pixel j, is the sampling step (in nm).

By measuring the SPD of monochromatic bands and the camera response it is possible to determine the sensitivity of the camera for each channel:

$$C_k(\lambda) = \sum_i Q_k(\lambda_i) L_k(\lambda_i) \Delta\lambda \tag{4.4}$$

where the k channel response is C_k , $Q_k(\lambda)$ is it's spectral sensitivity function,$L_k(\lambda)$ is the radiance. Assuming that $L_k(\lambda)$ has narrow spectral power distribution compared to the sensor sensitivity at the specific wavelength:

$$C_k(\lambda) = Q_k(\lambda) \sum_i L_k(\lambda_i) \Delta\lambda \Rightarrow Q_k(\lambda) = \frac{C_k(\lambda)}{\sum_i L_k(\lambda_i) \Delta\lambda} \tag{4.5}$$

The estimated reflectance R* is obtained for the corresponding original reflectance (R) from the camera responses for each channel (combination of channel and SPD), using an appropriate spectral estimation method [170]. If C_{train} and C are the camera responses of

the training and the test samples, then the estimated reflectance is given by:

$$R* = R_{train}C^{+}_{train}C \tag{4.6}$$

Therefore, the characterization of both the spectral emission of the illumination, as well as the camera sensitivity is the first step required for building the simplified multispectral modality. For simplicity purposes, each of the cameras is treated as a separate MS system.

Illumination SPD

The first step towards the development of the MSI modality was the measurement of the spectral power of the illumination source (projector). To achieve this, a CS-2000 Konica spectroradiometer was used, with wavelength range from 380 - 780 nm, along with a Spectralon White Diffuse Reflectance Standard (99%). The projector's LEDs were used in sequence to illuminate the Spectralon and the spectroradiometer was used to record the data. The measurement was performed under dark room conditions with spectroradiometer positioned above the projector (Fig. 4.22).

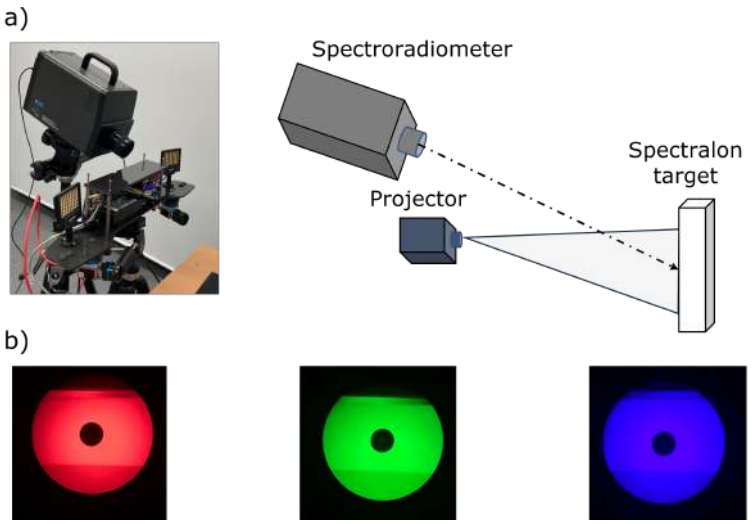

Figure 4.22: a) Measurement of projector SPD using spectroradiometer setup along with its schematic representation, b) spectroradiometer image during the SPD recording of red, green and blue LED.

The illumination spectrum recorded, shows peaks at 456 nm for the blue LED, 519 nm for the green and 624 nm for the red one. The SPDs of LEDs are presented in Fig. 4.23.

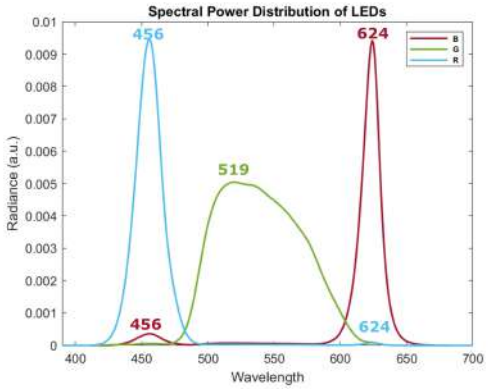

Figure 4.23: SPD of the projector LEDs.

Camera Sensitivity Functions

The next quantity needed for the development of the MSI modality is the spectral sensitivity functions of the camera. Data regarding the response of the separate channels within the visible wavelength region were not available from the manufacturer, and therefore they had to be experimentally determined. To achieve this a Bentham Monochromator (IS4c), equipped with Bentham Xe lamp (IL7 single) and a $BaSO_4$ coated sphere at the exit to have a uniform light output were used. The camera response was recorded for multiple wavelengths and the spectroradiometer (CS-2000 Konica) was utilized for the measurement of the spectral power distribution of the monochromators light.

The camera with the lens was positioned attached to the integration sphere and data acquisition was done in dark room conditions. Acquisition parameters for the camera were set once at the beginning of the experiment and kept constant throughout the measurement. Both raw and tiff data were recorded for comparison purposes. Gain and gamma corrections were disabled in the camera and the exposure time was determined experimentally at the wavelength of 550 nm, in order to prevent saturation. The acquisition setup is depicted in Fig. 4.24a-b.

Initially, data were recorded in the spectral region of 380 nm-700 nm with a step of 1 nm. The raw data were used to retrieve the cameras responses. Due to the CFA pattern, the raw data were separated into different colour channels and the intensity was averaged across a rectangular area at the center of the image (500 by 500 pixels) for each channel and wavelength. Then the monochromators spectral power distribution was measured, using the same configuration shown in Fig. 4.24 but replacing the camera with the spectroradiometer (dark room conditions, 380-700 nm with interval of 1 nm). The average bandwidth obtained

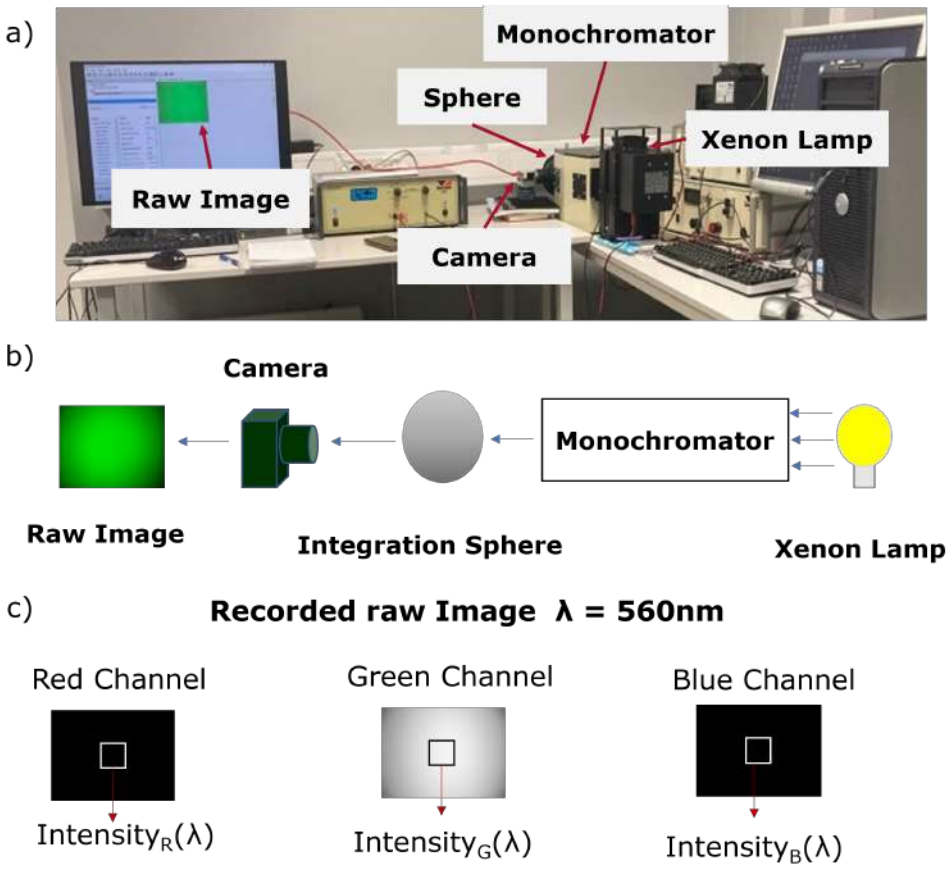

Figure 4.24: a) Acquisition set up for obtaining camera response along with b) its schematic representation. In c) exemplary image showing the intensity calculation for each channel is presented.

was 6.75 nm ±0.58 nm.

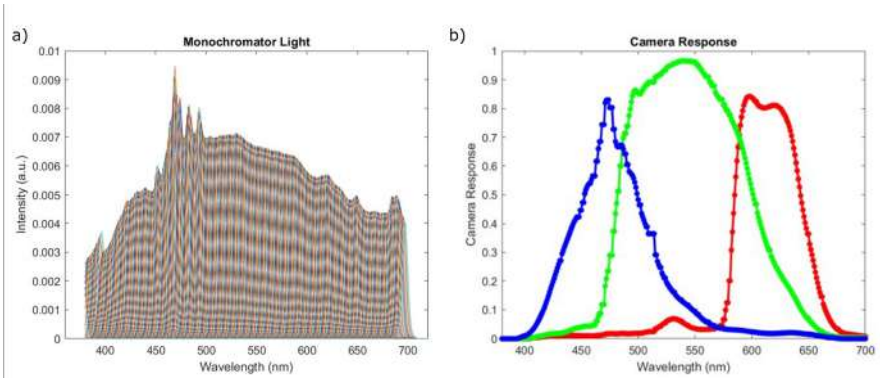

Figure 4.25: a) Monochromator SPD and b) camera response as measured with step of 1nm for the range of 380-700 nm

Combining the information from the monochromator's SPD and the camera response across this range of wavelengths, the camera sensitivity functions were calculated Fig. 4.26.

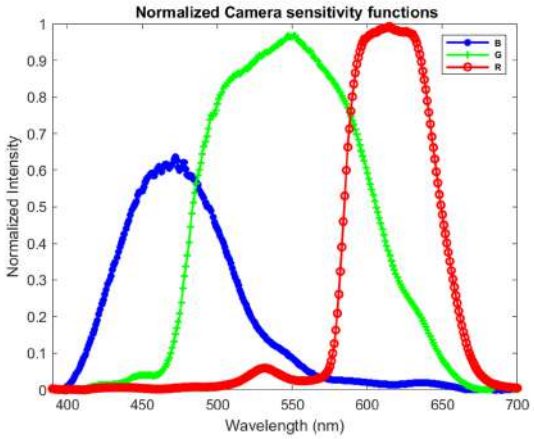

Figure 4.26: Camera sensitivity functions.

Simplified Spectral Modality

Finally, knowing the camera sensitivity functions and the LEDs SPD, the spectral bands of the system were calculated.The simplified system can record data theoretically in nine different regions of the spectrum, but some of them are overlapping and provide low quality data (i.e. band at 454 nm and 625 nm). Therefore out of the possible bands, the central wavelengths that are utilized for the simplified spectral reflectance measurements are: 456 nm with a bandpass of 20 nm, 502 nm with a bandpass of 35 nm, 537 nm with a bandpass of 83 nm, 590 nm with a bandpass of 21 nm and 624 nm with a bandpass of 14 nm (Fig. 4.27). The bands, with the exception of the one at 537 nm, have narrow bandpasses comparable to MSI commercial systems and are distributed across the visible electromagnetic spectrum.

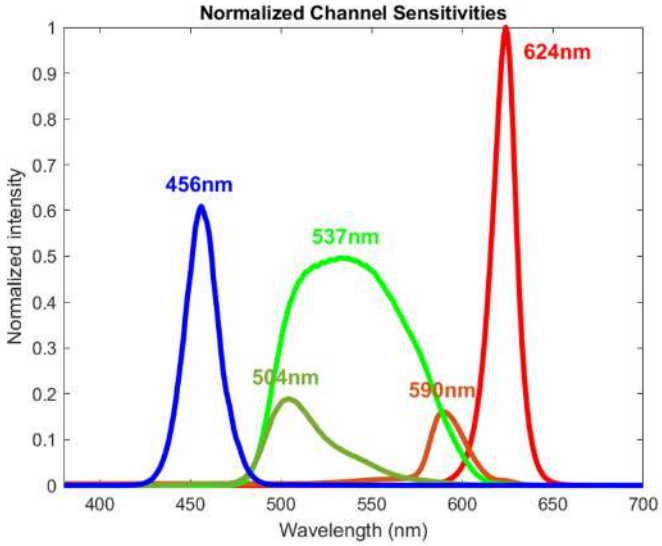

Figure 4.27: Spectral bands based on the combination of camera sensitivity functions and LEDs SPD. The graphs are normalized the red channel which has the highest intensity (624 nm).

MSI Calibration and Data Acquisition

The calibration and data acquisition processes are the same for both of the cameras, therefore in this chapter they are described only once. Prior to acquisition, the exposure time of the camera must be set in order to prevent saturation of both the object and the white calibration target images across all channels. Again, gain and gamma correction were disabled, and the same settings are used for both cameras. Calibration of MS comprises two main steps: flat field (FF) and dark current (DC) removal. FF correction is achieved using a white calibration target (typically a spectralon) and DC removal is done by recording a black image either by covering the camera lens or minimizing the exposure time. The data acquisition process for both the spectral calibration and the object involves sequential illumination of the target with the projector's primary LEDs. The number of images per measurement session is four in the case that the white target can be positioned within the object image, therefore combining measurement and calibration images. Otherwise, calibration and measurement data are recorded separately, resulting in eight images: four for the calibration and another four for the measurement. The recorded data (object, FF, DC) are separated into the three colour channels, and then FF and DC calibration processes are applied for each channel in order to produce the five spectral images. The dark image is subtracted in order to remove the dark current noise. Then, flat field correction is done by selecting the white reference area, averaging it, and dividing with that value the entire image. The process is repeated for each colour channel. For consistency purposes, the white area is selected once and the positions are maintained for all the channels (Fig. 4.28). For the FF correction, instead of spectralon, the reflectance values of passport colourckecker are used for the peak wavelength of every band, as they were experimentally determined using the SpecimIQ HSI camera. The SpecimIQ camera is a VNIR (400-1000 nm) with spatial resolution of 1280*960 pixels and spectral resolution of 7 nm [171]. The implementation is done in MATLAB, the selection of the white area is user input.

Spectral Reconstruction

Spectral Reconstruction (SR) is the process of estimating or recovering a complete spectrum from limited or incomplete spectral information. There are plenty of SR methods, but in this work, the Moore-Penrose pseudoinverse method was implemented [172]. The first step towards the SR is generating the MS cube using a reference target (in our case: the passport

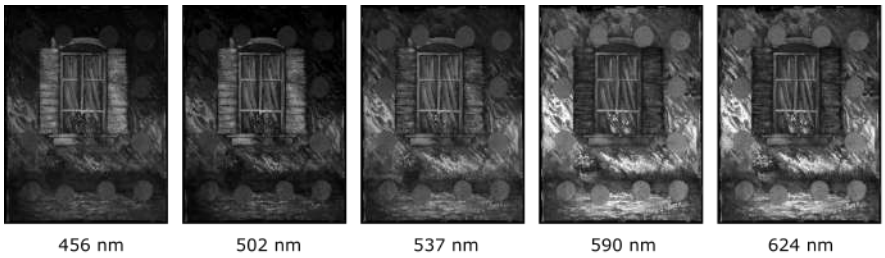

Figure 4.28: Exemplary MS Images.

colourchecker) and selecting the AOIs that will serve as training data (in this case, the colour patches). For the calculation of the SR matrix, reference data that correspond to the training are also required. Therefore, SpecimIQ HSI camera was utilized to retrieve the HS information of the patches. After extracting the data for each colourchecker patch for both the multispectral and the hyperspectral data cubes, the spectral reconstruction matrix can be calculated. For the calculation, the Moore-Penrose pseudoinverse method is implemented [172], and the SR matrix of the system can be used to reconstruct the spectrum of the unknown object.

Exemplary results are presented in Fig. 4.29. In this case one side of the passport has been used for the calculation of the SR matrix of the system, while the other side serves as the measured object. The reflectivity values of the spectral bands, along with the SR and reflectance data recorded with SpecimIQ for selected patches, are presented. The MSI data, as recorded with the MIS and the HSI data, are generally in agreement, with the recorded values following the same trend and only minor intensity differences for the different colour patches. The SR also provides acceptable results for all colour patches, with the RMSE value ranging from 0.056 to 0.124. The highest deviation among the SR and HS reflectance is recorded for a white colour patch.

MSI Processing Pipeline

The steps required for the MS modality, starting from data acquisition, to generation of the spectral images and spectral reconstruction are visualized in Fig.4.30. The user has to initiate the data acquisition process through the triggering described in Ch. 3.3 and repeat the acquisition both for the object and the white target data (in the case that the white target is not within the FoV). The black image for the DC correction needs to be captured manually. For the MS image generation, the user has to use a MATLAB script. The required input is the selection of the white area AOI. Finally, the SR is also implemented in Matlab script. The user

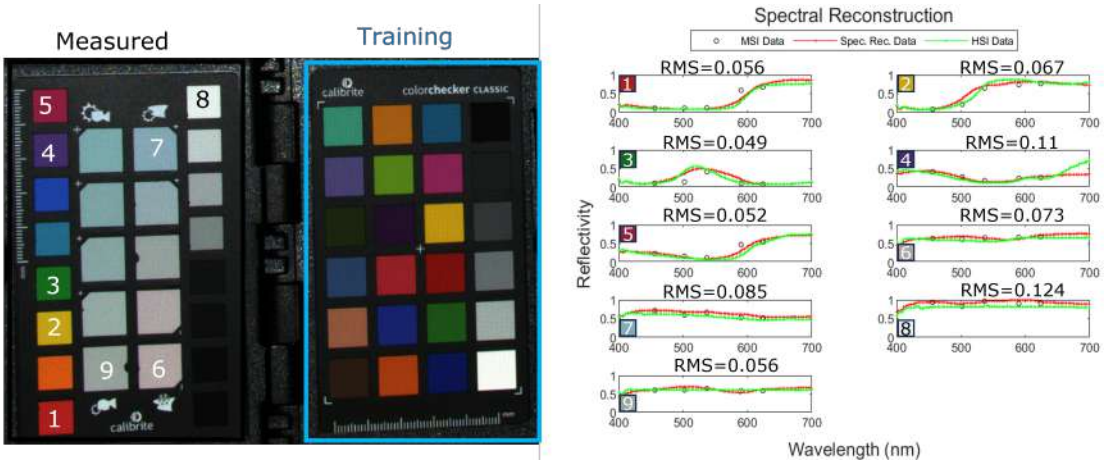

Figure 4.29: Spectral Reconstruction using parches from passport colour checker as training for the SR matrix calculation. The SR result along with HS data are shown for selected measured patches from the other side of the passport along with RMS error.

input is the path for the HS reference data cube, the MSI data cube for calibration and object. Finally the user has to select AOIs from the studied object for performing the SR.

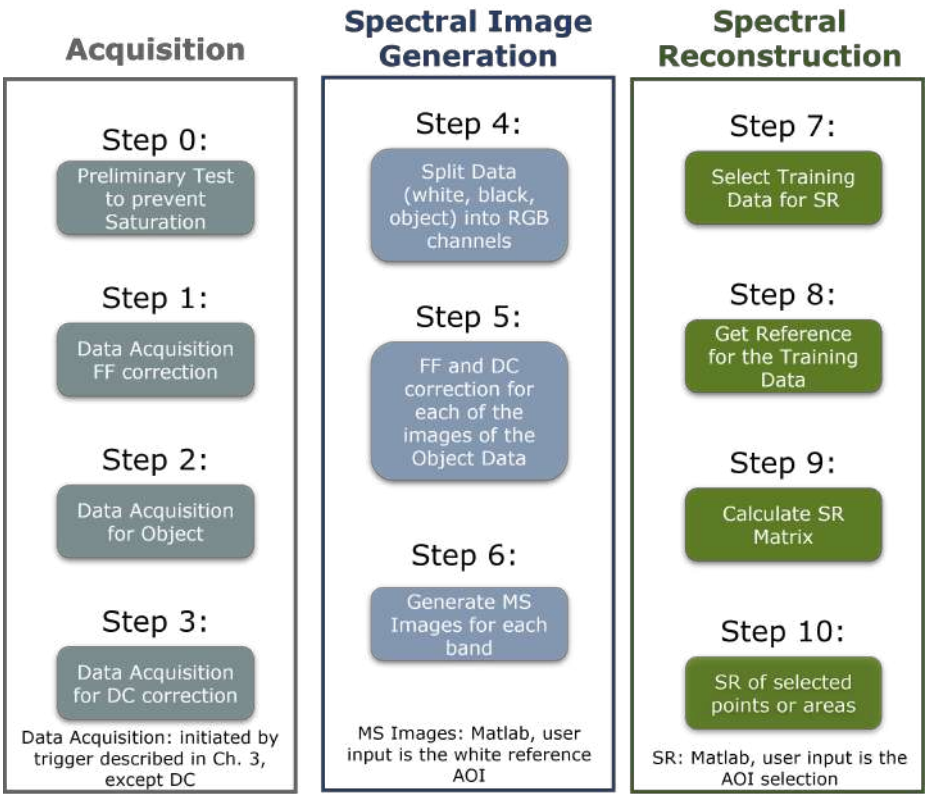

Figure 4.30: MSI data acquisition and processing pipeline.

4.2 Merging of Modalities

So far the distinct processing pipelines and methodologies utilized for the implementation of each modality has been provided in the previous chapters. Consequently, the next aspect that needs to be covered is the establishment of a systematic approach for merging the individual datasets into a unified coordinate system, and generating if desired a single output file for the three modalities. The primary modality employed in this system is the structured light method, specifically the gray code implementation. Reflectivity data, are not subjected to geometrical calibration, therefore their integration to the SL data is straightforward image mapping. In the case of cDIC a stereocalibration process, other than the one used for SL is required and therefore the process is more complicated.

SL and MSI data merging

The methodology will be explained starting from the MSI data, assuming that the processing until Step 6 of Fig. 4.30 is completed and the five spectral images have been already generated. The first step that needs to be taken is to apply the stereorecitifcation of the spectral images, in order to have per pixel correspondence with the SL data. Then, reflectivity value of each pixel is assigned to the CoP data during it's generation, the same is done for the RGB colour layer. The data are saved in both *mat* file format.

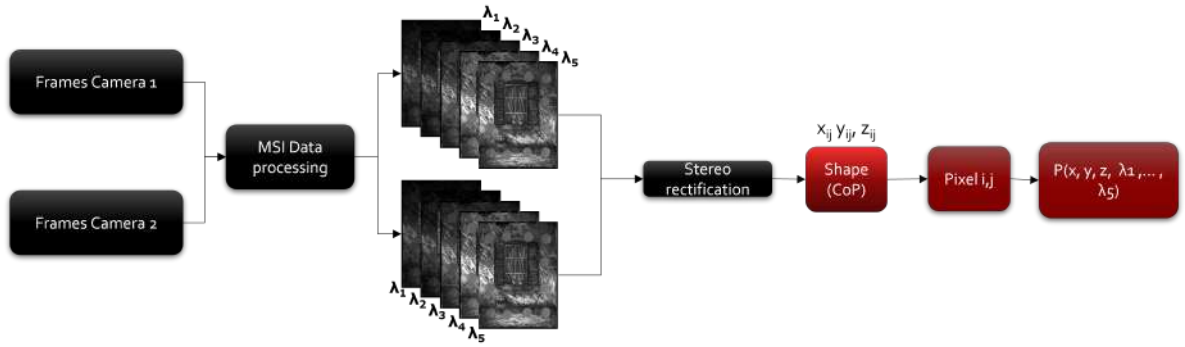

Figure 4.31: MSI data merging with SL pipeline.

SL and cDIC data merging

The merging of the cDIC dataset is more complicated as it involves merging data that are generated using two different calibrations. The system geometrical configuration is the same, but the VIC software used for the data processing has it's internal calibration algorithm which

does not allow access to the world points in order to reproduce it for the SL data generation. One way to approach this issue, would be to implement registration approaches combining manual preprocessing and/or ICP to align the data. This approach is implemented for hybrid SL method where the system records data into three coordinate systems from three separate calibrations (one for each of the two SL systems and one for DIC). This approach does not ensure elimination of registration/alignment errors, but it can still be accepted if no other option is available. Therefore, in order to minimize the errors emerging from the use of different calibrations a methodology for the data merging has been developed and implemented for the graycode SL (first calibration) and cDIC (second calibration). The aim was to accurately merge the data despite the different calibration processes while minimizing the error. To achieve this the first step, was the remapping of the DIC images, based on the stereocalibration results of SL and the respective rectification. This step has to be implemented prior to the analysis with VIC (or any other) software. This is to ensure that the pixel correspondence between the data will remain the same, and merging them accurately will be achievable. Exemplary pixel mapping of cDIC data (after processing with VIC) prior and after the remapping along with the respective SL pixel mapping can be seen in Figs.4.32a,d,g. The white lines are to help the reader identify the correspondence points across the images, while the area of the sample analysed using cDIC is denoted by the yellow colourmap Figs.4.32 b and c. The colourmap in Figs.4.32 d and f does not correspond to specific quantity, it has been added for easy identification of the analyzed area. The difference between the SL and DIC AoI will be discussed after the data merging implementation. From Figs.4.32 a and f it can already be observed that there is an offset in the pixel correspondence without the remapping procedure, which is resolved in Figs.4.32 g.

In addition to the correction of the image, the other issue that needs to be addressed is the sampling rate of the cDIC datasets. the maximum data sampling achieved outside the VIC processing software is two pixels. In principle pixel grid data extraction is foreseen in the VIC software, but the program crashes while attempting to export such files and the variable of disparity is not included in the extracted data. Therefore, prior to integrating the cDIC data with the other two modalities an interpolation step is required, to restore the per pixel resolution. The interpolation of the data is implemented via a MATLAB script in which cubic interpolation is used. The script for this preparation of the cDIC data requires as input the folder path of data needed for the interpolation. The interpolation is done for all of the cDIC

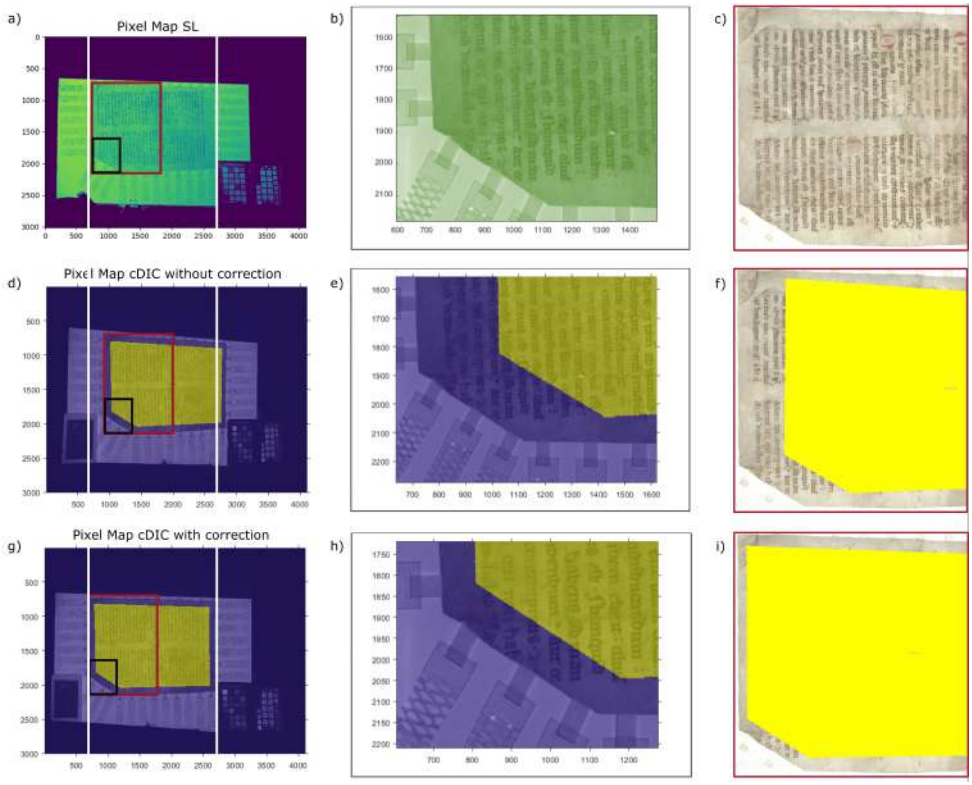

Figure 4.32: Pixel mapping of: a) SL, d) cDIC without correction g) cDIC after correction. The white lines are indicating the alignment of the data in the x axis. Detail of b) SL, e) cDIC without correction and h) cDIC with correction after point cloud generation with colourmap overlay. The yellow areas in e) and h) mark the cDIC data, the detail corresponds to the black box area. Area of the final c) CoP, f) and i) CoP and cDIC data merged before and after the correction. The area analysed with cDIC is denoted with yellow colour and the area shown corresponds to the red box of Figs. a), d) g).

quantities: disparity, U, V, W, sigma, e_{xx}, e_{yy}, e_{xy}.

Combining these two steps it is possible to minimize errors related to the use of two different calibrations and integrate the data into a single coordinate system. The origin pixel for each of the points included in the cDIC analysis is known. Therefore they can be directly mapped onto the point of the CoP based on it's pixel position. Since for each cDIC quantity value the origin pixel is known, it is possible to assign the corresponding point of SL calculated by mapping of the data, the same way as done for the colour and MSI bands layers. In Figs.4.32b,e,h a detail of the CoP data along with the merged SL and cDIC without and with the correction is presented (noted with black box). Again it is visible that the mapping of the cDIC data without the correction on the CoP results in failure. The efficiency of the proposed methodology can be confirmed by the exact correspondence of the letters for both the disparity map and the point cloud object 4.32h. For comparison purposes, a larger area of the sample is also presented in Figs.4.32f and i, along with the CoP area without the cDIC map

(Fig. 4.32c). This further confirms the inefficiency of the data merging without the corrective procedure.

For the realization of this process, the MATLAB file containing the interpolated data along with the disparity map is loaded in the python script used for the generation of the CoP. Then the mapping of the data is realised during the generation of the CoP based on the pixel position. This approach is summarized in a schematic representation in Fig. 4.33.

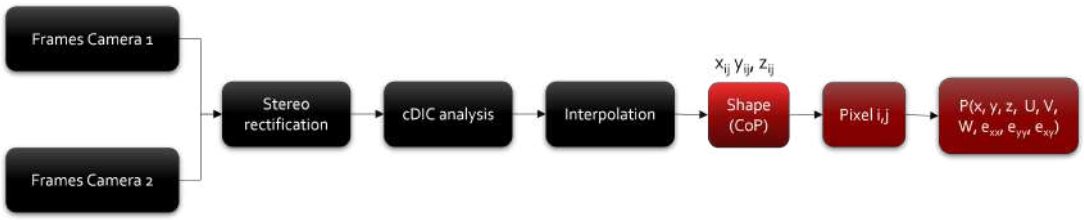

Figure 4.33: cDIC data merging with SL pipeline.

SL and cDIC shape comparison

As it can be noted in Fig. 4.32 the analysed area for the SL and cDIC modality is not an exact match. The reason behind this difference lies in the individual data modalities and their calculation principles. The SL modality can record data from all objects present in the measurement volume accurately as long as the object is not dark, and reflective. On the other hand, cDIC modality requires the presence of a speckle pattern, as already established in the previous chapters. Therefore, the area of interest has to be limited within the limits of the area of the parchment object, as the mounting system is white. In addition that, the cDIC analysis divides the AoI into smaller pixel blocks (subsets) and searched for correlation within them. The subsets that are located close to the border of the AoI but do not completely lie within it are eliminated from the search. Therefore, the resulting effective area of interest is slightly smaller than the actual area of the object. As 3D DIC is a stereoscopic method, it is also capable of calculating the shape of the analysed object Fig. 4.34c. Due to the correlation processes, the data are subjected to high frequency filtering, which results into a smoothed 3D shape in comparison to the physical object. The recorded 3D shape of a parchment object (Fig. 4.34a) using SL (Fig. 4.34b) and cDIC (Fig. 4.34c) methods vary due to presence, or absence, of local high frequency content respectively. While the global shape of the surface is captured with DIC, the local fluctuations are not distinguishable. In Fig. 4.34d the M3C2 distance [173] calculation between the two recorded shapes is also presented. The M3C2

distance is the local signed distance between two point clouds along the normal surface direction. This comparison demonstrates clearly the difference between the recorded shapes and the inaccuracy of the cDIC modality applied for 3D shape archiving purposes. Therefore, for the remaining of this work, shape refers to the data recorded using SL method, as this gives the most accurate depiction especially for objects with natural texture.

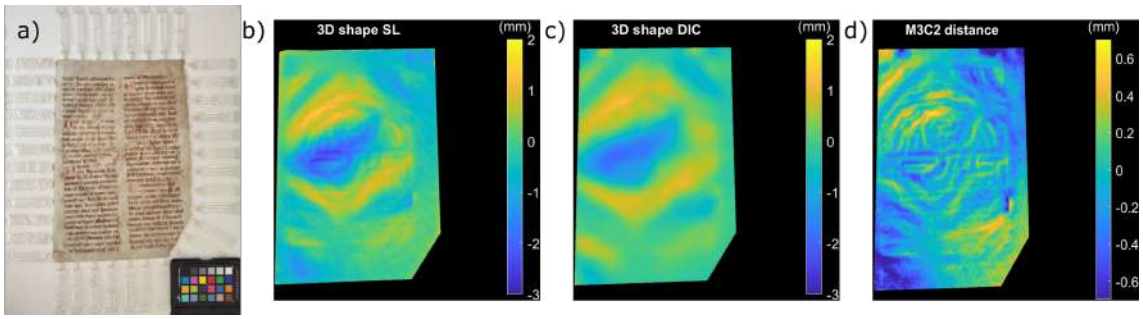

Figure 4.34: SL vs DIC Shape and M3C2 distance.

Conclusions

Taking all the above into account, the merging of the modalities can be summarized in the Fig. 4.35. MS and cDIC modalities are calculated separately, then they are integrated with the SL modality based on the pixel origin of each quantity. In this way, multimodal datasets are created, which have information regarding shape (x,y,z), reflectivity in five spectral bands, displacements and strains. The merging of the data can be further improved in the future if the same calibration target and procedures are used for SL and DIC, and in this way any residual error can be eliminated.

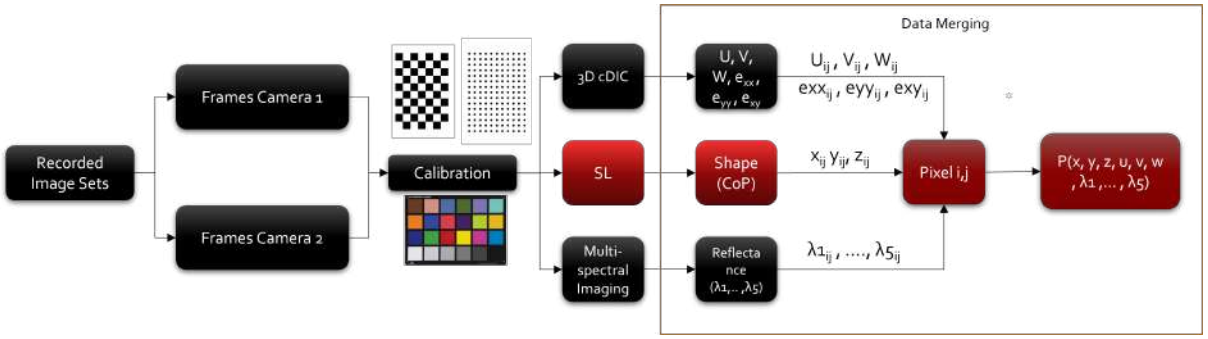

Figure 4.35: Data merging pipeline.

This chapter contains parts of the paper Spatio-temporal monitoring of humidity induced 3D displacements and strains in mounted and unmounted parchments published in Heritage Science 2022 [99] and the paper How to cope with a globe: conservation and restoration of a deformed globe published in Journal of Paper Conservation 2023 [69].

5

Measurement and Monitoring CH Objects

This chapter is dedicated to selected studies of measurement and monitoring of paper, parchment and painting CHOs and mock-ups using SL, cDIC and MSI individually. The results are organised based on the utilized modality and the analysed object. Specifically, the efficiency of SL modality is presented with respect to change detection before and after conservation of a paper globe, and change detection of an oil painting on canvas under environmental fluctuations. cDIC is implemented to the monitoring of parchment mock-ups and historical sample under relative humidity changes. Finally, MSI modality is used for the recording of reflectivity data on paintings and a case study of change detection of overpaint removal on a mock-up.

5.1 Change Detection with Structured Light

In this section two SL applications for the analysis of geometrical change are reviewed. The first example is related to the detection of deformations before and after a conservation treatment. The second is related to the detection of change on an oil painting on canvas (latter referred as *painting*) in cases where there is no intentional intervention and alteration comes as a result of fluctuations to the environmental conditions.

5.1.1 Globe Case Study: Deformation Analysis

The objective of this experiments was to measure the relative deformation detected on the bottom part of a globe, representing a school tool used for teaching purposes. The globe (Fig. 5.1a) is an untitled artefact and was created by "A. Nowosielski, Zakad Litograficzny (Lithographic Department) W. Gówczewski" a bit after 1920. Its dimensions are 17,2 cm sphere diameter of 172 mm and an overall height of 45 cm. The globe is made of cardboard covered in primer composed of gypsum and chalk. The lower supporting part of the globe has severely deformed over the years due to its own weight and extended use. Also, the great circle of the globe is torn apart from top and bottom and additional damages were shown on the surface over time. The damages along with parts of the object after the restoration are shown in Figs. 5.1 and 5.2. The restoration of the globe had been carried out by Lidia Małkowska, during the work for her MSc thesis at the Academy of Fine Arts in Warsaw, the under the supervision of Dr. Dorota Dzik-Kruszelnicka.

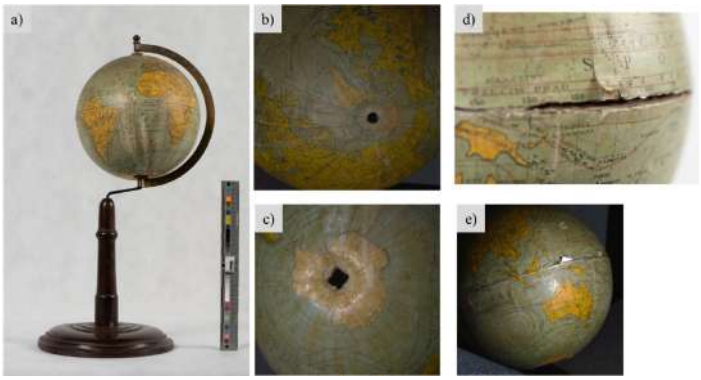

Figure 5.1: Globe object: a) its photo and the close-up image of b) the reference part at the top c) deformed part at the bottom and d,e) details with damage from its greater circle.

Using SL method the 3D model of the object was reconstructed in two phases: (phase 1) prior to any conservation intervention and (phase 2) after the conservation/restoration

treatment. The recorded model from phase 1 was used for the computation of differences among the shape of the upper and lower supporting structure as can be found in [174]. In this case the upper part was considered as a perfect reference and was utilized for the generation of a virtual mold model prior to the conservation. Potentially the 3D model could be 3D printed and used for the restoration of the object. During the phase 2, the shape of the object before and after the conservation was compared and geometrical changes between these two stages of conservation were quantified and detected.

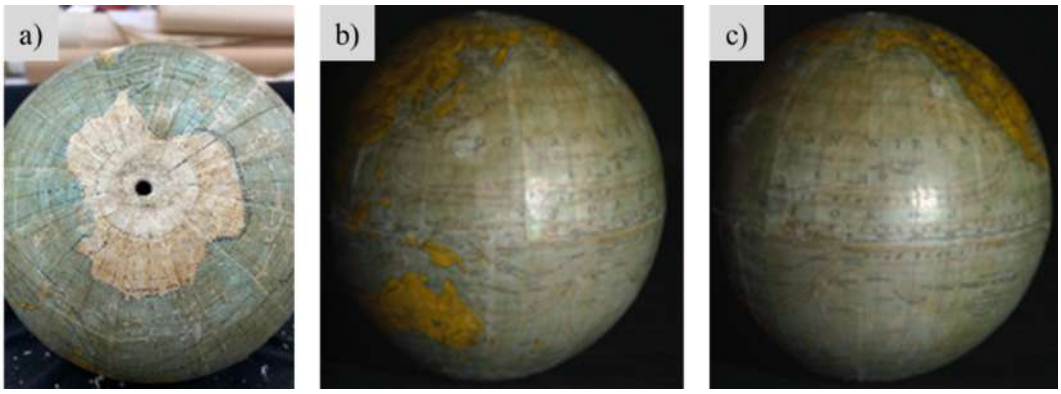

Figure 5.2: The Globe along with the areas of interest after conservation treatment: a) bottom and b, c) the greater circle of the globe.

For the purposes of this study, a hybrid SL scanner[156] designed and developed in the ZTRW laboratory at WUT was implemented. This measurement device has $E_{MPE} = 0.25mm$ and its measurement volume is 350 mm x 220 mm x 160 mm. The object was scanned multiple times in manual settings, meaning that the scanner was moved arbitrarily between acquisitions. Then noise was removed from the generated clouds of points and they were aligned into a 3D model using CloudCompare software [175]. Once both models were generated, manual and ICP algorithms were implemented once more in order to register the clouds into a common system.

The distance calculation algorithms available in CloudCompare were utilized in order to calculate the change in the shape of the object before and after the conservation. The results of this comparison for C2C (cloud to cloud) distance are visualized in Fig. (5.3 a, b). This was done by comparing the initial state (before conservation procedure) and the final state (after conservation). The results indicated a change equal to 7.38 mm at the bottom. This value is in agreement with the outcome of phase 1, where the shape comparison among the the upper and lower part of the object was performed [174]. This confirms the efficiency of the conservation intervention.

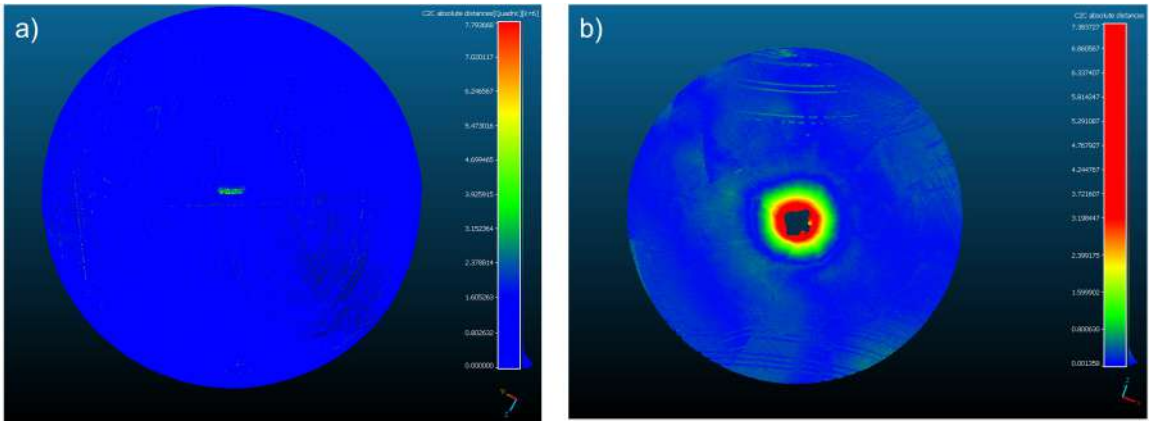

Figure 5.3: The C2C distance before and after conservation for a) the complete model of the globe and b) bottom part of the globe (in mm scale).

It has to be noted that C2C distance is an unsigned quantity and therefore we cannot obtain information regarding the direction of the change using it, as the value refers to the Euclidean distance between the closest neighbouring point of the clouds. In order to obtain the signed change values, the M3C2 distance was also calculated as shown in Fig. 5.4. The M3C2 distance takes into account an average area and calculates the signed distance between the best fitted normal plane [173]. The M3C2 and C2C distance have very similar values, confirming thus the accuracy of the calculation.

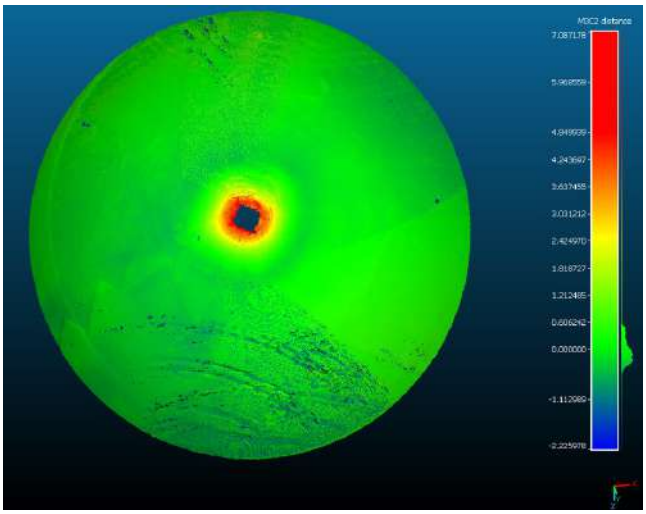

Figure 5.4: The M3C2C distance calculation depicting change at the bottom part of the globe (in mm scale).

The use of SL scanning in combination with traditional conservation approaches enabled conservators to decide on a course of treatment that would conserve the deformed part of the globe. The 3D model of the globe was created and compared to the model recorded prior the conservation. Apart from comparison purposes, the generated model can be used

for 3D printing and be incorporated to the objects' documentation. Thus enabling the creation of molds and replicas at the various stages of conservation both for documentation, conservation as well as for evaluation purposes. Advanced change detection algorithms have also been implemented within the context of this study, by Sunita Saha which can be found in [69].

5.1.2 Painting Case Study: Deformation Analysis

The aim of these experiments were to identify the changes in the geometrical shape over time on a painting. The object is a modern oil painting with linen canvas support, the artist is signing as WS and the age of the painting is more than 10 years. Paintings, similarly to parchments and papers are materials with high hygroscopicity, heavily influenced by changes in the surrounding environment. Transferring a painting between museum facilities or even moving it to an exhibition can sometimes be the cause of change, which can result into early deterioration especially for objects with structural weaknesses or pre-existing defects. Therefore regular recording of it's geometrical shape can assist conservators into identifying early degradation signs and take preventive actions. In this example we examine the influence of the environmental conditions in a framed painting over the duration of a year. Our aim is to assess and evaluate the magnitude of the deformation happening in the object while it remains in relatively stable environment. The data have been recorded using the hybrid SL method of the developed MIS.

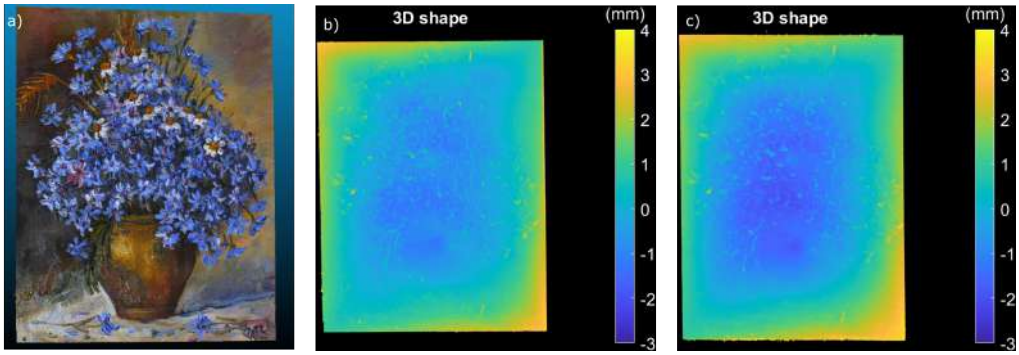

Figure 5.5: a)The painting under investigation, along with it's shape b) at time zero and c) one year later.

Using the SL method, the 3D model of the object was recorded in two instances, one year apart. In both cases, the object is dented around the center of the painting, which could be explained by the presence of a loose mounting system/stretcher. The shape distribution

could indicate a non-uniform force applied on the object by the stretcher, as positive shape values are mainly detected across two diagonal corners, top left and bottom right. The room in which it was stored had relatively stable conditions, with an average humidity of around 40 %±5 % and a temperature of 25 ±5 $^{\circ}C$ degrees, which is within the environmental conditions range provided in the Smithsonian guidelines [176]. The recorded models were not in the same coordinate system, as both the object and the scanner had been moved, and therefore registration of the data was required. This was achieved using manual and ICP registration algorithms from CloudCompare. After alignment, the geometrical difference between the two captures has been calculated using the C2C and M3C2 methods.

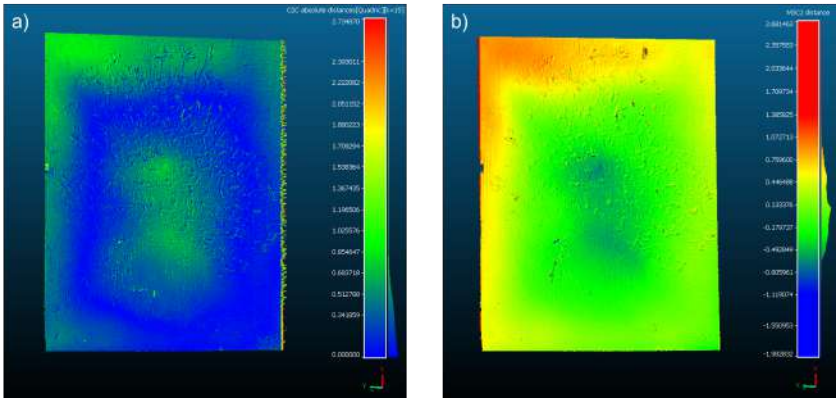

Figure 5.6: a) The C2C and b) M3C2 distance calculation (in mm scale) for the two scans of the painting, one year apart.

The object is framed, and despite the fact that it's loose, the supporting system is preventing it from deforming in comparison with a free-standing one. Both C2C and M3C2 distances are in the low range of values, P/V approx. 3 mm and 6 mm, respectively. The major change is detected towards the negative z axis in the middle of the object, while M3C2 reveals it has positive values at the upper left edge of it. This can be a further indication of the inhomogeneous effect of the stretcher. The lower part of the painting is presenting minimal/negligible changes, while the dent is again detected at the distance calculations. In principle, information regarding the object's natural shape and it's change over the years can assist conservators in making decisions related to preventive actions, such as re-framing and re-stretching the painting, once they evaluate that change is becoming threatening for the structural health of the object. Additionally, the 3D model recorded at the different stages can become part of the object's documentation archive or even be used in virtual exhibitions and museum actions.

5.2 Monitoring with 3D Digital Image Correlation

This section will provide an overview of two 3D DIC applications used for the structural monitoring of parchment under varying relative humidity (RH) conditions. The initial case study to be examined pertains to monitoring mock-up mounted and unmounted parchments. The second example involves monitoring a mounted historical manuscript in response to fluctuating RH.

5.2.1 Mock-up Parchment

This section presents examples of monitoring with 3D DIC mock-up parchments with artificial surface texture. The example involves displacements and strains computation of unmounted and mounted mock-up parchments with artificial speckle pattern using monochrome 3D DIC. The measurement idea is combined with the, crucial objective of evaluating the effectiveness of stabilizing a single sheet of parchment attached using elastic polyester strips (ES). Traditional methods only allow measurements at a given point in time and frequently necessitate the removal of samples from the climatic chamber; 3D DIC overcomes both of these constraints. The suggested methodology also has the advantage of being able to determine changes on both a global and local scale, allowing thus the conservator to fully evaluate the condition of the surface.

The natural texture of these parchments did not present enough contrast and features for correlation either with colour or monochrome cameras. Therefore, they were artificially textured using an ink pen. The resulting pattern is shown in Fig. 5.7. Application of speckle pattern was possible as the objects are mock-ups, and therefore 3D DIC was directly applied without the need to implement the developed cDIC processing path. The features of each sample is also presented (Figs. 5.7 c and d), with indication of their major fiber directionality, creases, and local thickness.

The samples were both subjected into a long humidity cycle, which represents fluctuations that could happen due to season change in uncontrolled storage room. The exposure of the samples to the varying humidity levels lasted a total of 216 hours and they are illustrated in Fig. 5.8. The response of the parchment mock-ups to the RH was monitored without interfering with the climatic chamber activities in situ, by positioning the 3D DIC system within the humidity chamber. The implementation of the parchment mounting system

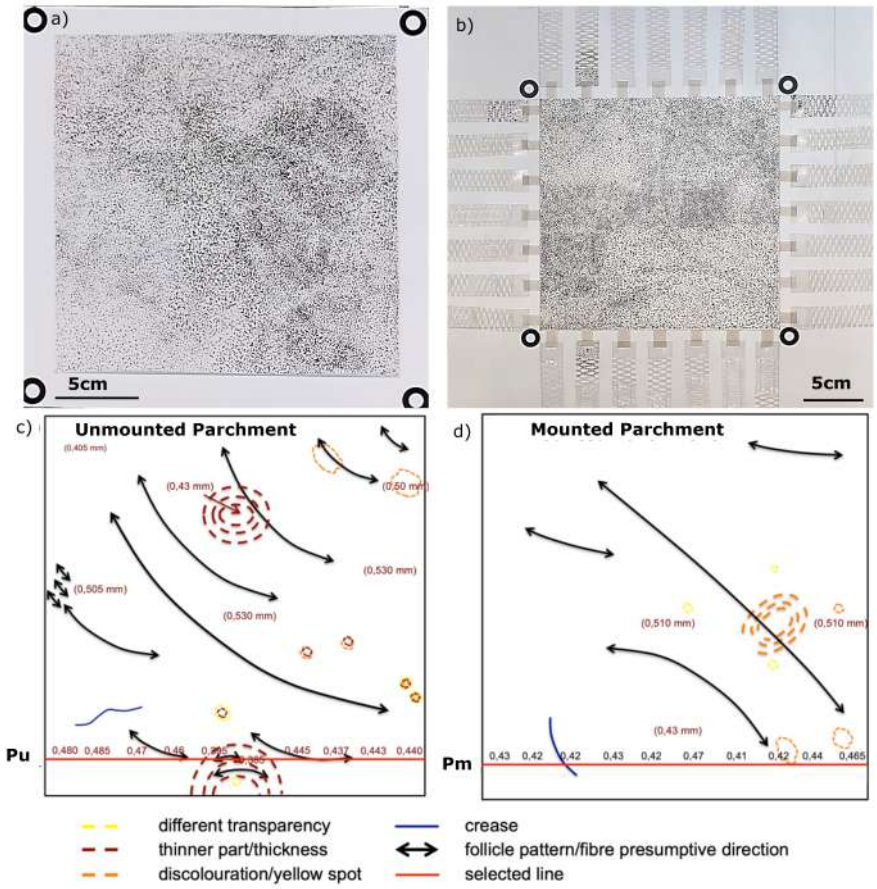

Figure 5.7: a) Unmounted (Pu) and b) mounted parchment (Pm) with artificial texture along with the mounting system. In c) and d) the main structural features of the parchments is shown.

involved the utilisation of elastic polyester strips, which were adapted from [177] and further improved based on research conducted at the Academy of Fine Arts in Warsaw [Aneta Kukuczka-Szarzec, unpublished observations]. The elastic strips (ES) were fabricated using a chemically neutral polyester foil and underwent laser cutting with a high precision to enable them to have flexibility and adjust to the varying dimensions of the object. The hinges connecting the ES and parchment were fabricated using Japanese kozo fibre paper (39 g/m2, Hosokawa). A coating of thermoplastic BEVA 371 Film was applied to the hinges. The attachment of the ES to the paper hinges was achieved through welding, wherein the applied glue was fused with a hot iron. The mounting system consists of a multi-layered cardboard panel (CP) with a honeycomb structure composed of -cellulose fibres. The paper hinges adhered to the polyester strips with a mixture of wheat starch paste (15 g/110 ml H2O) and isinglass (10%) in a 1:1 proportion. Symmetric stretching of 10 mm was applied to each ES, which were subsequently connected to the SP by welding the adhesive at their respective ends.

One crucial aspect of parchment monitoring pertains to assessing out of plane displace-

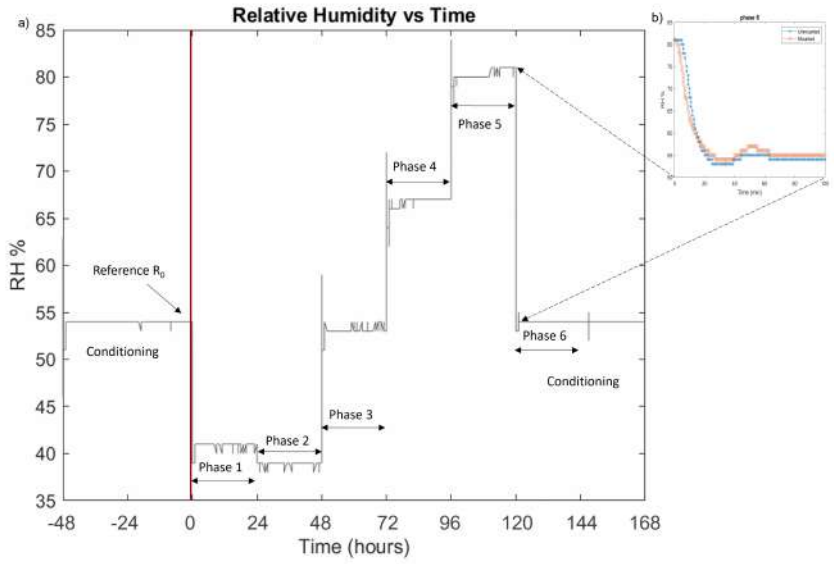

Figure 5.8: The RH changes as function of time for the a) total experimental duration and b) comparison of the transient RH(t) measured for the mounted and unmounted samples experiments).

ments exhibited by the samples during various RH phases. The most prominent change observed in parchment exposed to varying RH is the W displacement. These displacements are visually represented as a colourmap overlay, which is superimposed onto a 3D plot depicting the shape of the parchment in each phase. Refer to Figs. 5.9 and 5.10 for a visual representation of these findings. The illustrated examples correspond to the end time of each humidity phase after the sample reaches a state of equilibrium for approximately 23 hours.

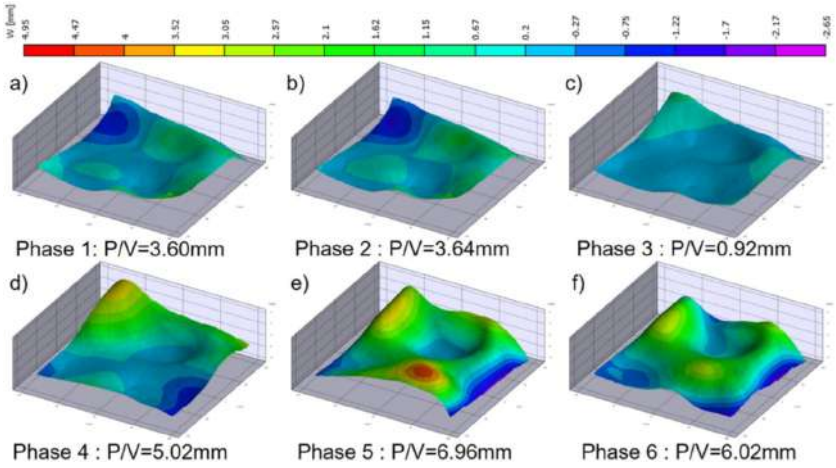

Figure 5.9: 3D shape of the unmounted sample with applied colourmap that corresponds to W displacement for the RH Phases 16).

Over the whole RH range, W displacement P/V ranges from 0.76 to 2.11 mm for Pm, while 0.92 to 6.96 mm for Pu. In Phase 3, Pu and Pm had minimal displacement values of 0.92 and

0.76 mm. In Phase 5, Pu and Pm samples had the highest displacement (Pu: 6.96 mm and Pm: 2.11 mm). The mount also affects the character of displacements; for Pu, the displacements change from concave through nearly flat (Phase 3) to convex (Fig. 5.9), while for Pm, the convex-like displacement at Phase 1 becomes convex at Phase 3 and stabilises with the quasi-convex displacement distribution at Phase 6 (Fig.5.10).

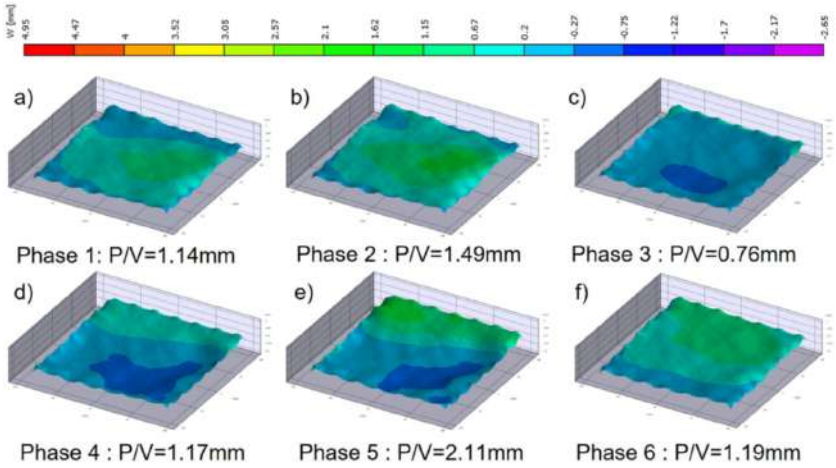

Figure 5.10: 3D shape of the mounted sample with applied colourmap that corresponds to W displacement for the RH Phases $R_1 - R_6$).

To further analyse the local behaviour of the object across the experiment duration and connect it with it's known local features, spatio-temporal maps of selected cross sections for W displacement have been generated. The spatio-temporal maps are composed of the W values along the selected horizontal cross section shown in Fig. 5.7c and d. The thickness of the objects is known for the location of the cross sections which are indicated in Figs. 5.7c and d, respectively. The thickness for L_{Pu} varied from 0.395 mm to 0.530 mm, while for L_{Pm} from 0.430 mm to 0.510 mm. The displacements observed in the cross section of P_m are at least three times smaller in magnitude compared to those observed in P_u. The maps in Figs. 5.11a and 5.12a are showing the entire experimental duration of 168hours while the maps in Figs. 5.11be and 5.12be present illustrate time spans of 120 minutes. These maps provide an insight into the complete evolution of displacements during changes between consecutive RH levels.

At the specified cross section, the Pm undergoes substantially lower W displacements than Pu (Figs. 5.12 and 5.11) and stabilizes faster. The displacement behaviour at the transition between Phase 3/4 and 4/5 for L_{Pu} varies significantly in comparison to the rest, which might be an indication for denaturation and gelatinisation processes occurring when RH reach high values (here 80 %) [178, 179, 180]. In addition, an inflection point can be observed

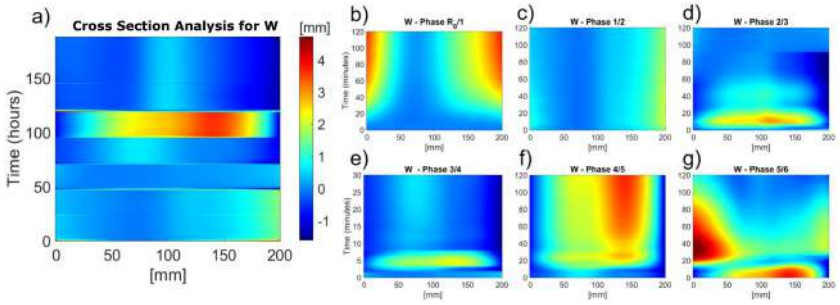

Figure 5.11: The spatio-temporal maps of W displacement in the crossection L_{Pu}. The maps W(x,t) representing a) the entire experiment duration, be detailed maps W(x,t) for the rapid RH changes between sequential Phases $R_0 - R_6$ for the time span of 120 min.

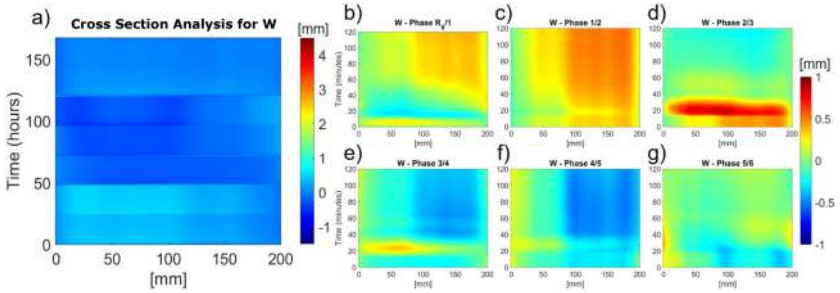

Figure 5.12: The spatio-temporal maps of W displacement in the crossection L_{Pm}. The maps W(x,t) representing a) the entire experiment duration, be) detailed maps W(x,t) for the rapid RH changes between sequential Phases R0- R6 for the time span of 120 min.

in the middle of L_{Pu} for phases $1-5$ while for Phase 6, a local maximum of displacement occurs (Fig. 5.11a). This behaviour is confirmed also in the transition maps (Fig. 5.11bg) and can be attributed to the local small thickness of the parchment combined with the local direction of the fibres. Regarding P_m the presence of the ES, creates a spatial modulation of W amplitude (approx. 0.15mm) across L_{Pm}, observed in Figs. 5.12b,c,e,f (and clearly visible in Fig. 5.10). Correspondence between the local thickness variations and W displacements cannot be noticed.

Following a similar approach, the full-field in plane displacement maps (U and V) of P_u and P_m have been calculated (Figs. $5.13-5.16$). The P/V values of U and V displacements for P_u and P_m exhibit a comparable range, spanning from 0.1 mm to 2.1 mm, with marginally diminished values observed for the mounted sample. Minimum values occur during Phase 3, while maximum values of P/V are observed during Phase 5.

The distribution of in plane displacements can be correlated with the directionality of the samples fibers, which predominantly exhibit diagonal orientation of the major fiber direction (Figs. 5.7 c and d). The most modulations of the fiber direction is observed in P_u, which results into variations of the in plane displacements. If the samples have a consistent

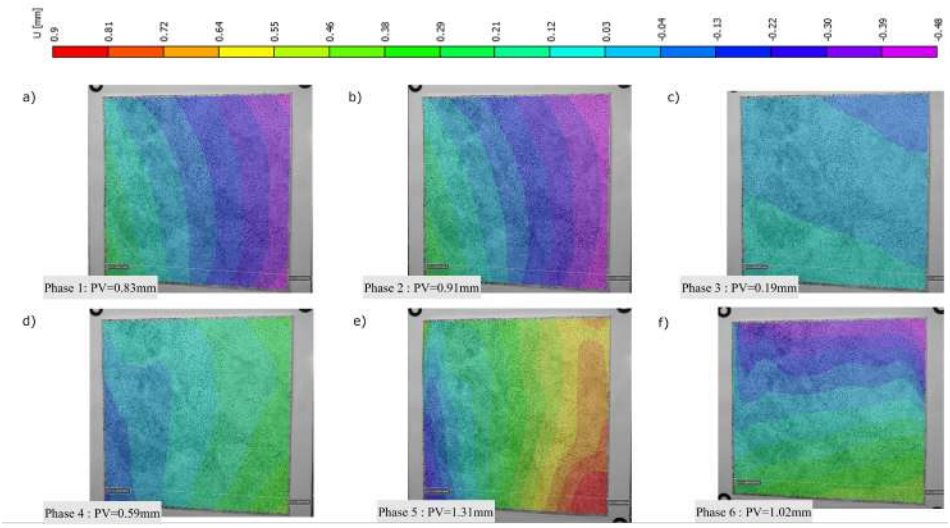

Figure 5.13: 2D colourmap of the U(x,y) in plane displacement of Pu at the end of Phases 16.

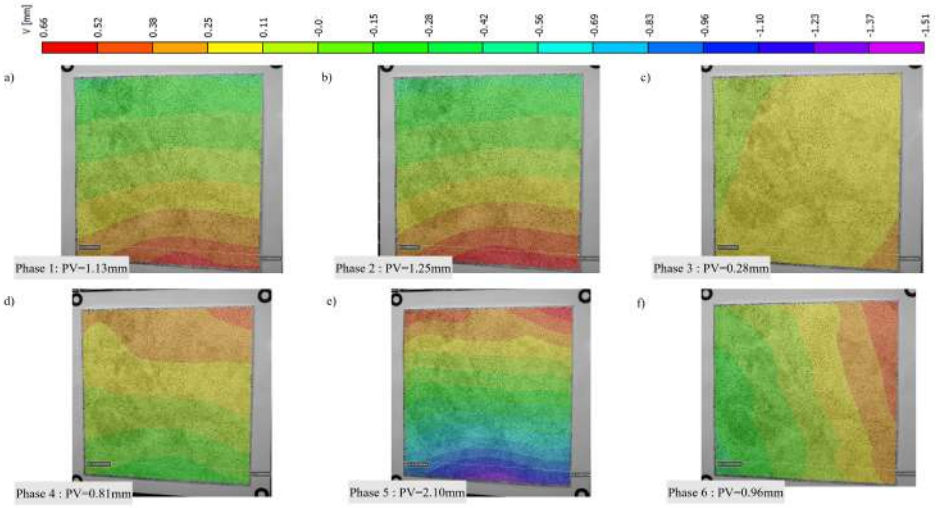

Figure 5.14: 2D colourmap of the V(x,y) in plane displacement of Pu at the end of Phases 16.

thickness and diagonal orientation of fibers, then U and V displacements should be linear, having equal magnitude in both the x and y directions. The results depicted in Figs. 5.13 and 5.14 have predominantly linear terms both for U and V, which are locally altered as a result of the change in fiber direction. This phenomenon is clearly visible in Figs. 5.14 where distinct nonlinear variations are observed in the lower regions of the V displacement maps. These nonlinear terms are associated with the direction of the fiber, which is changing from diagonal to horizontal, and the thickness of the sample is reduced at this location.

Upon analyzing the in plane displacement maps of P_m (Figs. 5.15 and 5.16), they exhibit a similar character to that of P_u, with the exception of the end of Phase 6. The displacement gradients (Figs. 5.16f and 5.16f) during this phase are smaller compared to those observed

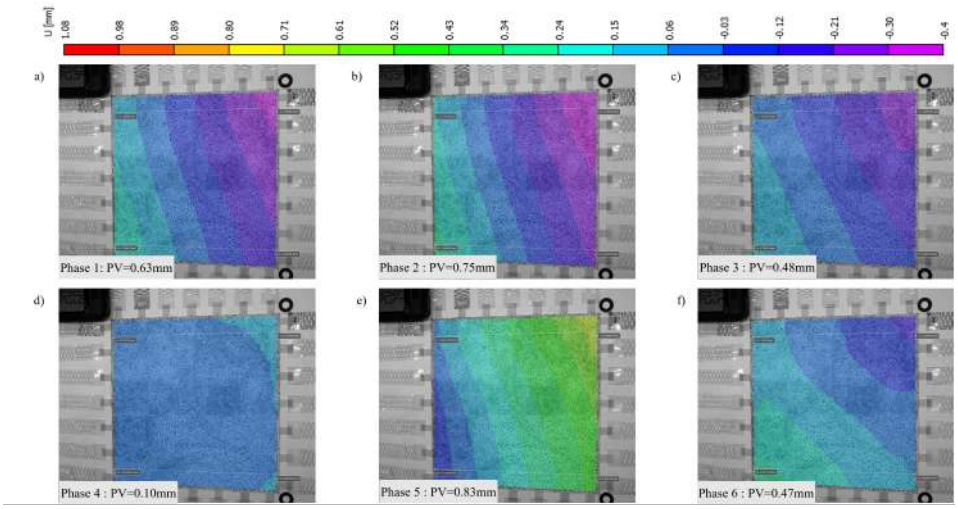

Figure 5.15: 2D colourmap of the U(x,y) in plane displacement of P_m at the end of Phases 16.

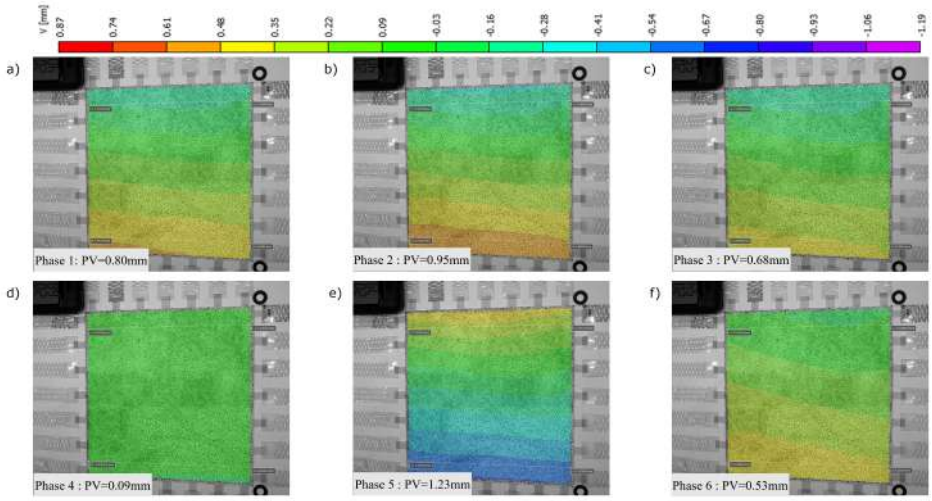

Figure 5.16: 2D colourmap of the V(x,y) in plane displacement of P_m at the end of Phases 16.

in P_u (shown in Figs. 5.13f and 5.14f). The magnitudes of U and V displacements for Phases 3 and 6 exhibit negligible values, indicating that they undergo minimal stretching or compression in comparison to their reference state. The U and V displacements have prominent linear characteristics, thus proving the efficiency of the mounting system.

The non linear behaviour of the P_u is expected to also be depicted in the strains, for this reason, the spatio-temporal maps of strains are presented. The spatio-temporal maps are for the same L_{Pu} and L_{Pm} as before and the presented maps are for the entire experiment duration (168 hours). The different values of the linear terms in displacements at the sequential Phases, result to different levels of ε_{xx}, ε_{yy} and ε_{xy} strains generated for each of the Phases (Figs. 5.17, and 5.18). The maps indicate the strong dependence of strains values from the

RH levels. They also show that the values after each RH step change significantly and are not released or notably changed during stabilisation periods. The strains ε_{xx} and ε_{yy} are compressive during Phases $1-2$, stretching during Phases $4-5$, and slightly stretching during Phase 6. The strains ε_{xx} and ε_{yy} have approx. $2-3$ times lower values for the unmounted parchment; however the character of the changes is similar. Both samples at this crossection undergo small shear strain. In the ε_{yy} map of the unmounted sample a local maximum is detected at the middle of the crossection (Fig. 5.17b), which confirms the influence of local variations in thickness combined with the local change of fibers directions on strain values. This is also confirmed through the modulation in ε_{xy} map (Fig. 5.17c). Such modulations are not clearly visible in the strain maps of P_m (Fig. 5.18). However the forces introduced through symmetrically located hinges and elastic stripes should have additional impact on the local strain distribution. The reason for the lack of information about the strains caused by the mount in Fig. 5.18 can be attributed to the use of a common colour scale for strains of L_{Pu} and L_{Pm} which may hide small strain modulations.

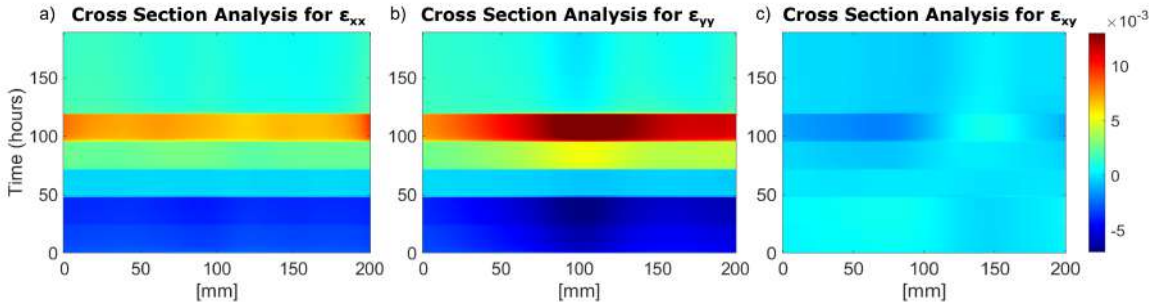

Figure 5.17: Spatio-temporal maps of the strains a) ε_{xx}, b) ε_{yy} and c) ε_{xy} of the horizontal cross section LPu.

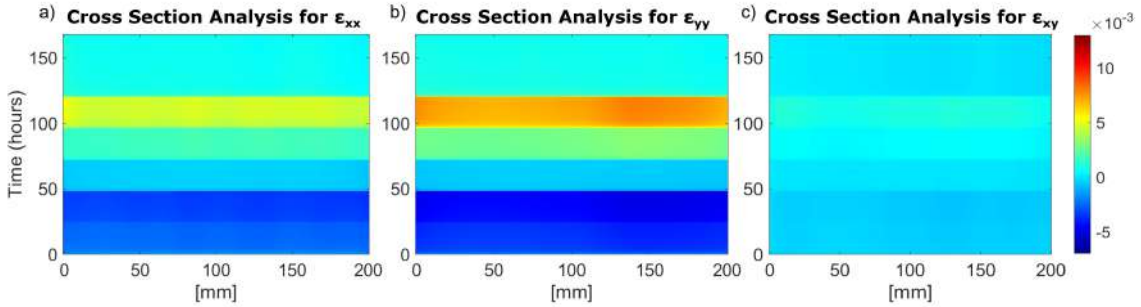

Figure 5.18: Spatio-temporal maps of the strains a) ε_{xx}, b) ε_{yy} and c) ε_{xy} of the horizontal cross section LPm.

Overall, the most significant change corresponded to the 80% of relative humidity, which lead to the maximum detected W displacements. The presence of the mounting system suppressed the displacements two folds, while allowing the sample to move similarly to the free-standing one, proving thus its effectiveness. In plane displacements and strains analysis in the selected time instances, as well as during constant monitoring (spatio temporal maps) enabled to correlate the inherent material properties (fibre directionality, and thickness) with the mechanical response of the sample. Although, each RH change deforms the object irreversibly, the proper mounting suppresses the displacements and assists on the safety of the artifact. It has been confirmed that the strains level at the mounted sample is kept lower than at the unmounted one and that the deformations and strains introduced locally by the hinges and elastic stripes are negligible.More information and results related to this topic can be found in [99].

5.2.2 Historical Parchment

Having gained extensive insights and knowledge from the study of the mock-ups the same methodology was applied to monitor the response of a mounted historical manuscript subjected to relative humidity fluctuations using 3D cDIC.

Mounted Historical Manuscript

As described in the previous chapter, applying DIC for objects with natural texture is possible, with some compromise in the calculation accuracy. Utilizing colour sensors and the unique texture of the individual colour channels can result into more intense texture features, which can allow for correlation to be achieved. Therefore, in this section, we have utilized the methodology described in Ch.4.1.2, and the pipeline of Fig. 4.8 and APN demosaicking for the monitoring of displacements and deformations of a mounted historical parchment manuscript without an artificial pattern.

The object of interest for the 3D cDIC measurement is the parchment manuscript shown in Fig. 5.19a. The hand-written parchment fragment, whose exact date remains uncertain but it is believed to originate from the fourteenth century. It was discovered within the confines of a book cover, where it was serving as a spine strap supporting material. The origin of this fragment, however, remains unknown. The manuscript had previously undergone conservation treatment. In order to investigate the impact of variations in RH on the historical

material, it was mounted using the system of ES and CP described described in the Ch. 5.2.1.

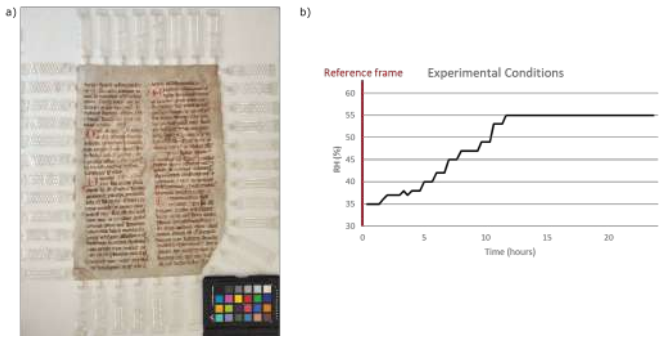

Figure 5.19: The photos of a) the historical manuscript and b) the RH graph for the experimental duration.

The historical material's response to naturally varying humidity levels, ranging from 35%-55%, during a day was monitored (Fig. 5.19b). The humidity cycle for this object was naturally occurring and not artificially induced by a humidity chamber. Therefore, monitoring it's response to extreme RH values are not included in this study. The reference frame was selected at the beginning of the experiment at which RH=35%. The displacements and strains recorded at the end of the experiment, when the RH=55% are presented in Fig. 5.20.

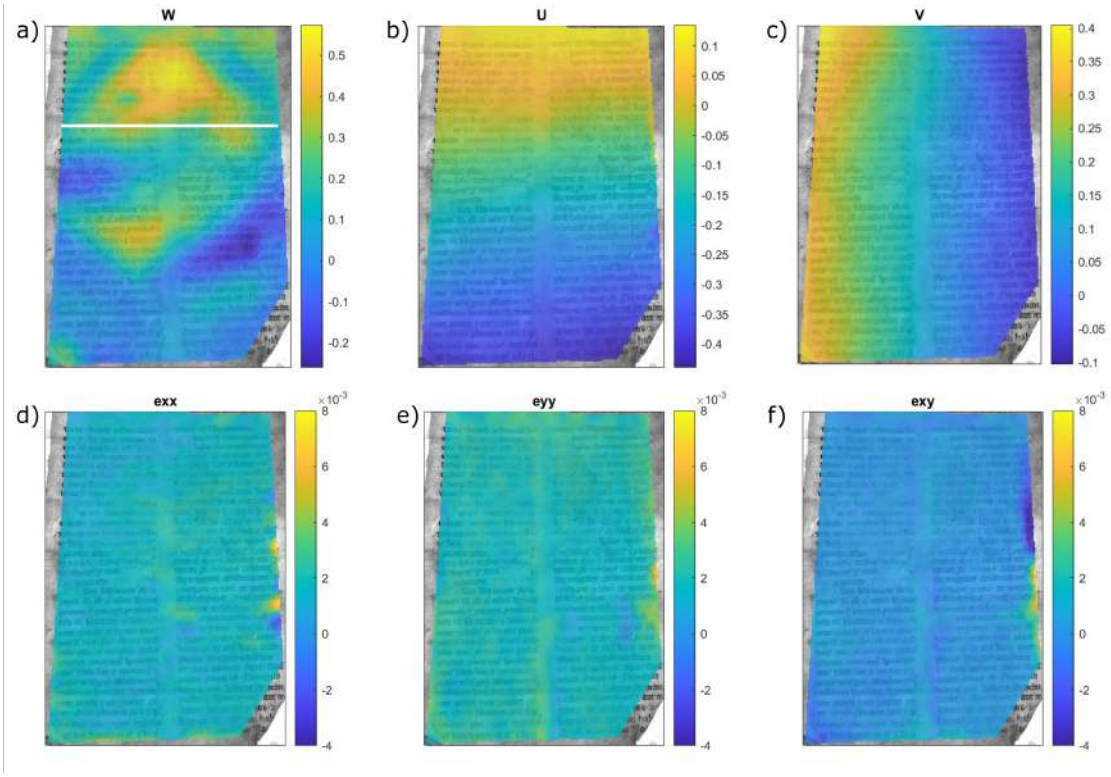

Figure 5.20: The colourmaps of displacements a) W, b) U, c) V and strains d) ϵ_{xx}, e) ϵ_{yy} and f) ϵ_{xy} of the historical manuscript for RH=55%. The white line in a) W map corresponds to a cross section selected for further analysis.

The values of the in and out of plane displacements lie within the range of a single millimeter (5.20). Both U and V in plane displacements show linear trends. This confirms the effectiveness of the mounting system, which prevents the curling and deformation of the material by symmetrically stretching the sample. The highest P/V value is detected for W displacement, equal to 0.84mm, while in plane are $P/V_U = 0.57mm$ and $P/V_V = 0.51mm$. The strains are homogeneously distributed, denoting the effectiveness of the mounting system quality, with exception being an area at the right edge of the sample. There are two possible reasons for the increased strains in that area, one being that the modulations are caused by the ES preventing the material from deforming. The other possible reason is the location of the strains, which is at the edge of the sample, and in some cases the correlation around edges is not locally good.

Following a similar approach as for the mock-up objects, a cross section of the manuscript was selected (indicated with a white line in Fig. 5.20a) for further spatiotemporal analysis (Fig. 5.21). The crosssectional analysis is performed by incorporating data from the entire duration of the experiment. Once the humidity reaches a stable state (after 12 hours), the system demonstrates a consistent behavior. The recording rate for the experiment is one pair of frames every half hour. On the other hand, within instances of fluctuating humidity levels, the analysis allows thorough examination of the ongoing processes. The occurrence of positive strains, which is linked with material stretching, has been observed in response to increases in humidity, and these strains exhibit stabilization once the humidity reaches a state of equilibrium. The observed pattern in strain behavior remains consistent throughout the dataset. Again, high strain values are recorded around the edge of the sample, but their generation cannot be clearly attributed to the presence of ES or the correlation processes.

The results of this experiment demonstrated that the modified 3D cDIC is extremely useful for conducting in depth, full field investigations of historical parchments. In addition, the efficiency of the mounting system is confirmed through the linear in plane displacements detected for the RH level of 55%. Similarly to the results from the mock-up parchments the strains were not released after the humidity stabilization, while modulations are observed which can be attributed to the presence of the mounting system.

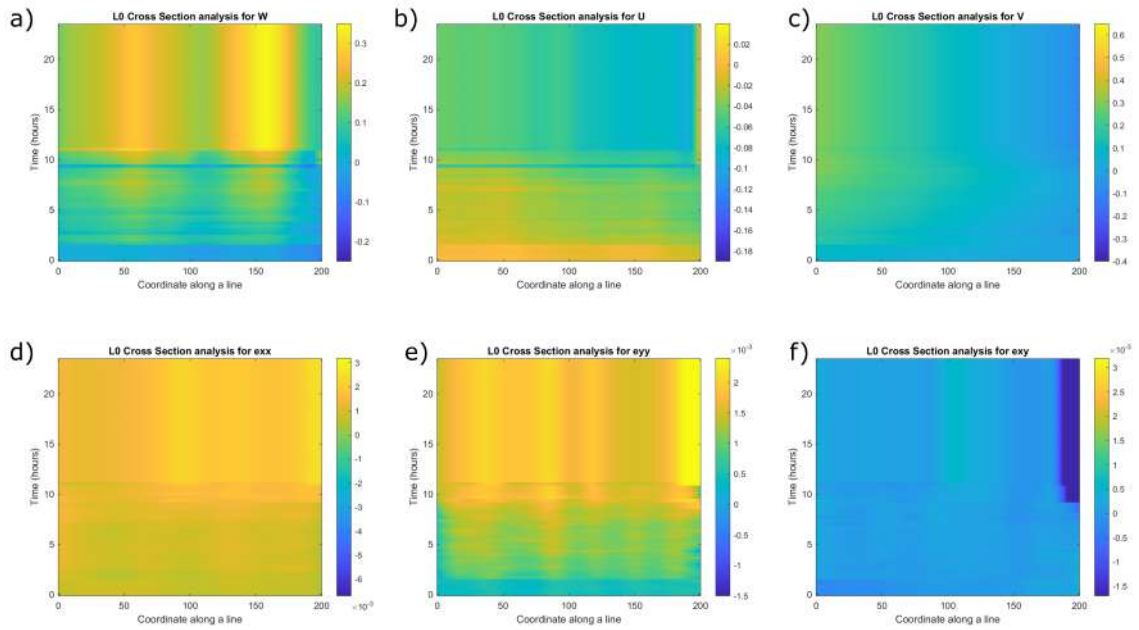

Figure 5.21: The spatiotermporal maps of a)W(x,y), b) U(x,y), c) V(x,y) displacements and d) ε_{xx}, e) ε_{yy} and f) ε_{xy} strains the horizontal cross section for time experimental duration.

5.3 Multispectral Imaging

This section provides an overview of two MSI applications used for the reflectivity measurements of paintings. Specifically, the focus is on the utilization of MSI modality of the MIS on modern oil paintings, and a comparative analysis is made with HSI measurements. Additionally, a case study is presented, showcasing the practicality and potential of the chosen modality in monitoring changes during the process of overpaint removal from a modern oil painting.

5.3.1 Reflectivity Measurements of Paintings

Two paintings have been selected for the comparison of reflectivity measurement, between the MSI of the MIS and HSI datasets, recorded using Hyspex and SpecimIQ cameras. The HSI measurements have been conducted at the ColourLab of NTNU, under the supervision of Prof. Sony George. The paintings are not of historical or cultural importance, they are modern oil paintings from a local Polish (signing as WS) and Norwegian (unknown name) artists. Finally, MIS was utilized to measure an unknown object - for which data were not recorded with any commercial system.

The painting has been measured using the MSI modality of the MIS system (Fig.5.22a)and the commercial push-broom HSI and SpectroCam MSI systems, within the same day. The HSI system comprised of Hyspex VNIR (visible and near-infrared portion of the electromagnetic spectrum) and SWIR (Short-wave infrared Short-wave infrared) cameras and was vertically mounted on motorized XY axis table equipped with halogen lights positioned at 45° for illumination (Fig. 5.22b) [181, 182]. The data recorded from SWIR camera will not be concerning us within the scope of this chapter. The VNIR camera has spectral range of 4001000 nm, spatial resolution of 1800 pixels and is recording data in 186 spectral channels with spectral sampling of 3.26 nm. The SpectroCam [1] is equipped with 8 band pass filters in the range of 375 nm up to 930 nm and CCD sensor with resolution 2456 x 2058 pixels [183]. The registration of SpectroCam data has been performed using the the Rigid transformation of Register Virtual Stack Slices plugin from Fiji [184]. The MS camera, mounted on a tripod, was positioned vertical to the sample and halogen lamps were utilized for the illumination at an angle of 45° (Fig.5.22c). FF and DC correction was performed for all the methods in order to calculate the reflectance factor.

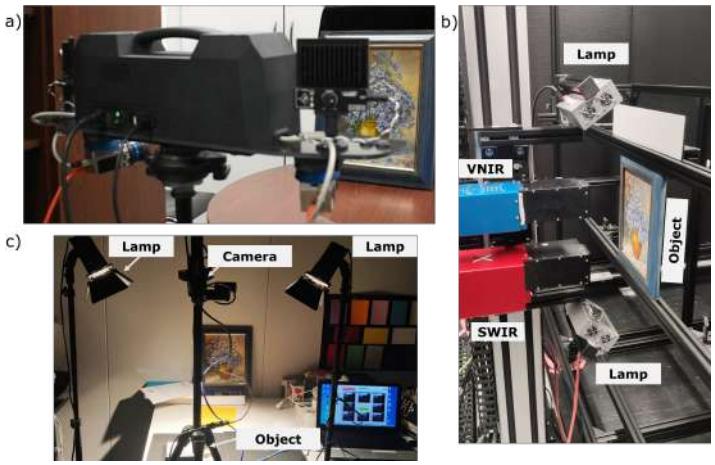

Figure 5.22: The systems used for reflectivity measurements: a) MIS, b) HySpex c) SpectroCam.

Regarding the MSI modality of the MIS the data have been recorded following the protocol described in Ch. 4.1.3 (and summarized in Fig. 4.30). As explained in Ch. 4.1.3 the object images are recorded under the red, green and blue illumination (Figs. 5.23a-c), out of which the images corresponding to the five spectral bands are generated. The data of the MIS after the FF and DC correction are shown in Figs. 5.23d-h. Visual observation of the images corresponding to the spectral bands, can already show the different spectral response of areas

[1] https://www.oceaninsight.com/

corresponding to different pigments. For example the main part of the blue flowers is fading towards the images corresponding to the mid/end part of the spectrum.

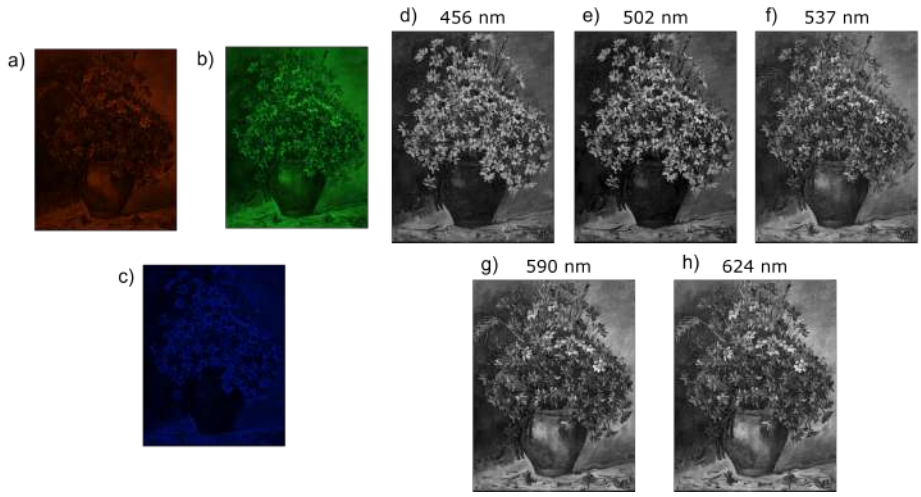

Figure 5.23: Flower painting under a) red, b) green and c) blue illumination from the projector along with the spectral images corresponding to the bands of d) 456nm, e)502nm f)537nm g) 590nm h) 624nm recorded with the MSI modality of the MIS.

To further investigate the variation to the reflectivity of the sample across the recorded wavelength range, and also compare it with the data recorded using the HySpex HSI and SpectroCam MSI systems, a few areas of the sample were selected. The areas analysed are marked with green colour numbers in Fig. 5.24a, along with their detailed view in Figs. 5.24b-j. The areas were selected in random positions of the sample and with the aim to correspond to different colours (1-blue, 2-yellow, 3-green, 4- reddish, 5-yellowish/brownish, 6-black). It has to be noted that the data recorded using the different systems have different resolution, therefore making the analysis of single points a challenging task, as exact one to one correspondence cannot be established. Thus, to overcome this challenge and minimize the error it was chosen to perform the analysis and spectral reconstruction using areas, and average the reflectance factor within them. The selection of the areas has been performed manually with custom made script in MATLAB.

The Fig. 5.25 presents the reflectance factor of the Hyspex HSI, MSI MIS, and MSI SpectroCam datasets for the designated areas, along with their SR. The datasets exhibit a consistent response across the two MSI recording systems, with the primary discrepancies observed in the magnitude of the reflectance. The RMS error is computed between the MIS SR and HySpex datasets, and the SpectroCam SR and HySpex. The two MSI systems perform comparably in terms of the quality of SR, with the RMS error being lower for the MIS data for

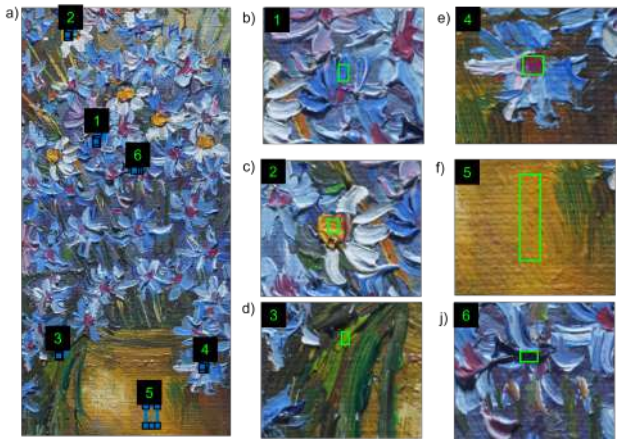

Figure 5.24: a) Analysed areas of the *Flower*, along with their detailed view b-j. The green box indicates the area selected for analysis.

areas 1,4,5 and 6 of the object and the SpectroCam data for the rest. It can also be observed that the data in the reflectance recorded for the wavelength of 625 nm is approximately the same in all cases, proving thus the quality of the MSI modality of the MIS.

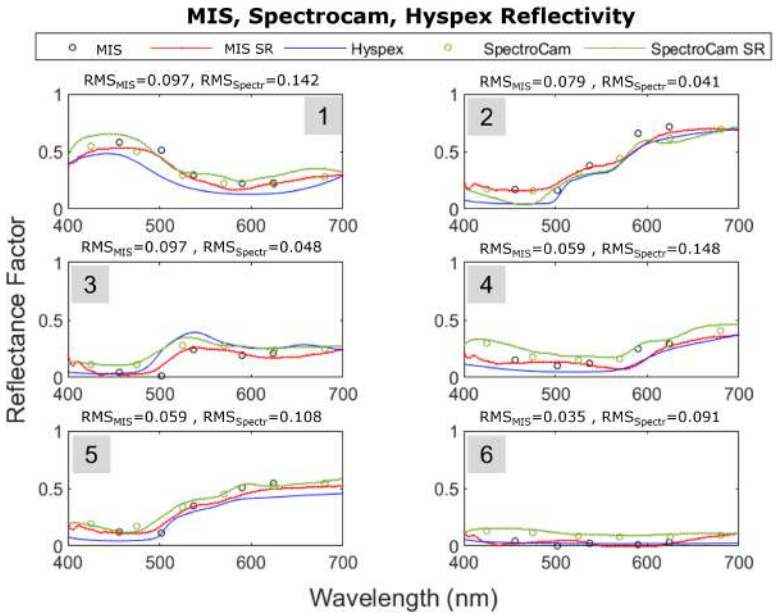

Figure 5.25: Resulting spectra of the selected areas for the MIS, SpectroCam and HySpex datasets. The RMS error has been calculated both for the MIS and SpectroCam SR with respect to the HySpex dataset.

Following a similar approach, but in this case only using the MSI modality of the MIS and the SpecimIQ HSI camera one more painting has been analysed. The object is depicted in Fig. 5.26a, and shall be referred to as *Vase* for the remainder of the text. The data for this object have been recorded using SpecimIQ camera mounted on a tripod. SpecimIQ is a VNIR portable camera with range 400 nm up to 1000 nm, with spectral resolution of 7 nm and

CMOS sensor reaching spatial sampling of 512 pixels. This camera has integrated software performing FF and DC corrections automatically, again data beyond 700 nm are not considered herein. The slightly higher RMS error values detected in this case can be the result of the low resolution of SpecimIQ in comparison with HySpex. Overall, the selected areas are in agreement in terms of spectral response for the MIS and the HSI datasets.

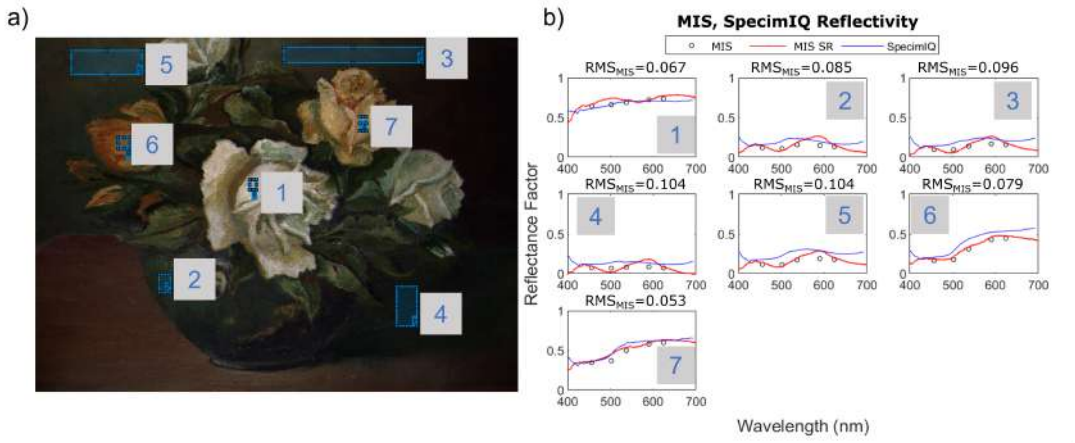

Figure 5.26: The analysis of the *Vase* painting: a) the painting with indicated areas of interest and b) the resulting spectra of selected areas for the MIS, and SpecimIQ datasets.

Overall, the MSI modality of the MIS performs reasonably well for the case of complex painting objects. Of course, the results recorded with commercial systems are more accurate to the actual reflectance factor of the object. In all cases, the trend of the data is consistent with the commercial systems, while main variations are detected in their magnitude. Therefore, the MIS can be utilized for initial object documentation and archiving purposes, with further systems being employed for accurate measurement reflectance.

5.3.2 Mock-up Painting: removal of overpaint

Now that the correspondence and single instance measurement using the MSI modality of MIS and commercial systems has been established, next step is to test the capabilities of the developed modality at the detection of change in reflectivity. For this purpose a proof-of-concept experiment was conducted on an oil painting with an overpaint layer. The overpaint layer, was created using multiple Penart matte water-based varnish layers and white acrylic spray paint (Fig. 5.27a). It was applied to a small area on the painting marked by semi-transparent tape, the average thickness of this multilayer structure is approximately 0.5mm, as measured at ten random positions across the layer after it's removal. The overpaint was

removed mechanically, by pulling the edges of the tape, thus resulting in small shift of the sample between the recorded data. For this reason, registration of the data was performed (using Fiji, as described in the previous section) and areas of interest were selected instead of pixels.

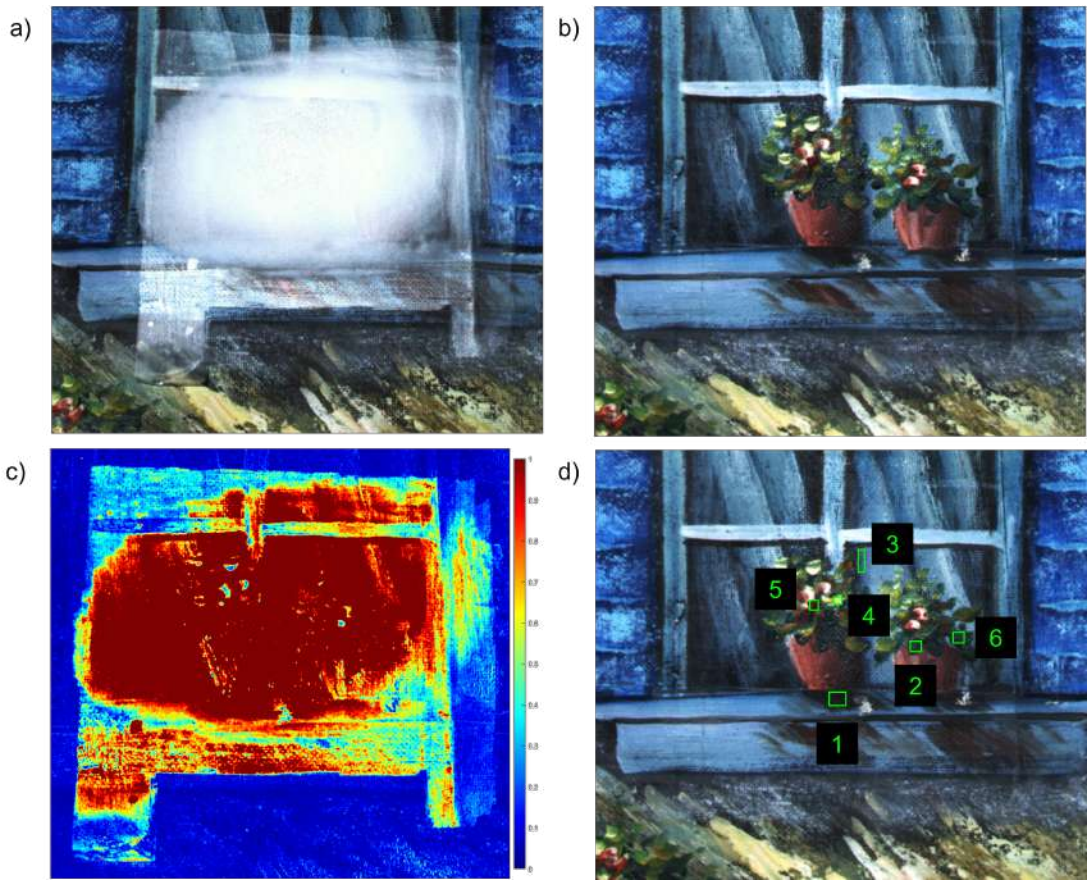

Figure 5.27: The area of the painting with a) the overpaint and b) same area after the removal. In c) the normalized Euclidean difference map of the spectral cubes before and after the removal is shown and in d) the selected AOIs for spectral reconstruction.

Following the MSI data processing methodology described in the previous sections the spectral cubes for the object were calculated prior and after the overpaint removal. In Fig.5.27c the normalized Euclidean difference between the two spectral cubes is shown, after thresholding values less than 0.1. As expected, the major differences between the reflectance before and after the removal are detected on the area of the overpaint, while minor differences are detected also in the surrounding area covered with the tape.

Several areas, corresponding to different colours were selected for further analysis and spectral reconstruction (Fig. 5.27d and 5.28). The RMS difference between the SR before and after the overpaint removal is also shown. It is evident, that the reflectivity of the areas is changing significantly once the overpaint is removed and the true colours of the object are

revealed. Also, the white spray layer does not have constant reflectivity through the spectrum, with higher values detected at the bands of 590 and 624nm. The small fluctuations to it's magnitude can be attributed to the inhomogeneity of the applied spray paint.

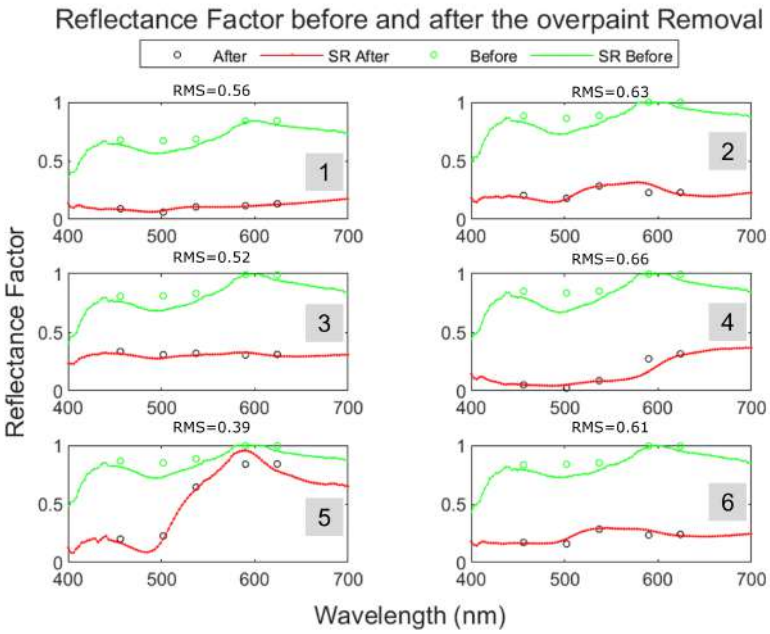

Figure 5.28: Resulting spectra of the selected areas before (green) and after (red) the overpaint removal, along with their spectral reconstruction.

Overall, monitoring change in the spectral content of an object using MSI can be critical to the successful and informed removal of overpaint from a painting. This proof of concept experiment, confirms that with the developed modality monitoring such changes can be possible, as confirmed by the results of Figs. 5.27c and 5.28. It can provide conservators with valuable insights into the composition, condition, and original appearance of the artwork, allowing for a scientifically supported restoration process.

5.4 Summary of the single modalities applicability of MIS

To summarize, in this chapter individual measurement and monitoring sessions using the MIS have been presented. The SL modality has been utilized for change detection in an oil painting after it's storage in a room with uncontrolled environmental conditions. The applicability of the developed cDIC processing path has been presented through a monitoring session performed on historical parchment during relative humidity changes. The MIS modality has been compared with the performance of commercial systems though measure-

ments of oil paintings and, finally, utilized in a monitoring session of overpaint removal. Using the MIS modalities individually it has been possible to record data for the documentation of an object's condition, determine the scale of changes in displacement and strains within monitoring sessions, as well as monitor their global and local spatio temporal responses.

6

Multimodal Measurement and Monitoring

6.1 Multimodal measurement of Painting with defects

In this chapter, the results from multimodal measurement and monitoring of a painting with known defects is presented. The object under investigation is a modern oil painting on synthetic canvas. Several defects, representing conservation methods used in paintings, currently and in the past, were created on the painting. The aim of the study was to evaluate the conservation methods and their effect to the sample following the multimodal approach provided by the MIS functionalities. This study has been conducted in collaboration with Diana Kułakowska, M.Sc from the Faculty of Conservation and Restoration of Works of Art, of the Academy of Fine Arts in Warsaw, Poland.

6.1.1 Object Description

The object under investigation is a modern oil painting from an unknown artist in Greece. It holds no significant cultural value; therefore, it was possible to create known defects in order to evaluate methods commonly applied in painting conservation. The substrate is made of synthetic canvas, and the object was framed on a wooden stretcher for the purposes of this experiment. The defects were created utilizing methods that are representative of commonly used conservation methods in the present as well as in the past. In Fig. 6.1 the front and back sides of the object, along with the schematic representation of the patches, are shown.

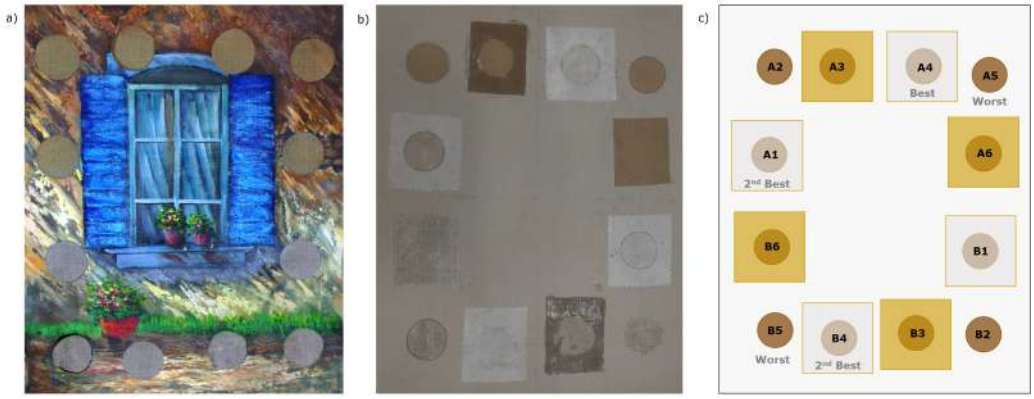

Figure 6.1: Image of the a) frond and b) back of the painting along with the c) schematic representation of the patches.

The methods and materials used for the patches are listed in Table 6.1. Among the studied painting conservation techniques is the application of slightly oversized patches with excess threads thinned with a scalpel, which are attached to the canvas using a heat-activated adhesive. This type of patching was done in two slightly different ways, with an additional layer of non-woven fabric attached to the back of the support and without it. This process ensures that the patch adheres firmly to the canvas, providing enough support. The selection of the heat-activated adhesive utilized is another essential aspect of painting restoration. For this reason, within this study, both Beva D-8-S and Akrylkeber 498 HV have been used. These adhesives provide strong bonds, allowing conservators to attach patches securely while still being able to remove them if necessary. The investigated methods represent commonly used, current day and past, approaches for painting filling the gaps in textile supports. The technique of attaching patches with a wax-resin binder is also being investigated. In this case, the heat application ensures a strong and long-lasting connection between the patch and the original surface. This method is reversible to some extent, as the patches are

easy to detach, but the excess of wax-resin binder difficult to be entirely removed. The left-over wax-resin binder render the paintings stiffer and often severely deformed after some years and therefore, this method is avoided nowadays.

The type of canvas combined with the patch method provides representative examples of modern and ancient methods (wax-resin binder), allowing for a thorough evaluation through multimodal measurement and monitoring. Generally, the aim is to use canvas of exactly the same type when it comes to density, thickness and fiber type, but in this experiment only in half of the patches were created this way. The other half were made with canvas differing from the original in fiber type, linen instead of synthetic (but not in density and thickness). The linen patches were created as it's most likely for an average restorer to use it in case finding a perfectly matching canvas would be impossible. In principle, if exactly the same type of canvas is used for patching, then patches should react to humidity changes and have the same mechanical properties as the original support. Of course, this is impossible to achieve in practice, since between support and patches there is always a layer of glue that behaves differently than them. Therefore, one of the aims of this study was to investigate the impact of the fiber type to the structural condition of the painting. From the conservator's perspective, optimum results (minimal strains and deformations) are expected for patches A4, A1 and B4, while the worst is expected at the A5 and B5 patches. It has to be noted that by carefully selecting and attaching a compatible canvas patch with the appropriate adhesive, conservators can stabilize damaged areas with minimal impact on the artwork's structural properties. The maximum duration of the stabilization period depends strongly on the patching method as well as the storage conditions of the object.

Table 6.1: Painting Defects Methods

	Type of textile used for patching
A	synthetic canvas sized with animal glue (7% wt) - canvas woven comparably to original support
B	linen canvas sized with animal glue (7% wt) - canvas woven comparably to original support
	Patching Technique

Continued on next page

Table 6.1: Painting Defects Methods (Continued)

1	patch cut to size, attached with Beva D-8-S and heated to 95 °C; non- woven polyester fabric (Hollytex 34 g/m^2) attached with Akrylkeber 498 HV (2 layers) and heated to 115 °C
2	slightly oversize patch with excess threads thinned with scalpel and attached with Beva D-8-S and heated to 95 °C
3	oversize patch attached with a wax-resin binder and heated to 115 °C
4	slightly oversize patch with excess threads thinned with scalpel and attached with Beva D-8-S and heated to 95 °C; non-woven polyester fabric (Hollytex 34 g/m2) attached with Akrylkeber 498 HV (2 layers) and heated to 115 °C
5	patch cut to size, attached with Beva D-8-S and heated to 95 °C
6	oversize patch attached with Akrylkeber 498 HV (2 layers) and heated to 115 °C

6.1.2 Experimental Conditions

The object was stabilized in a dark room, prior to the initiation of the measurement using the MIS. The back surface of the object was wetted and the monitoring of the drying was ongoing for 80 minutes while the room and humidity temperature were constant at T=23 °C and RH= 23%. The multimodal (MM) measurement scenario included :

1. *Initial Measurement (t=0):* Shape recording (SL), Reflectivity measurement (MSI), cDIC recording (reference images)

2. *Monitoring Phase (t=0 to t=79 minutes):* Recording with cDIC every 1 min

3. *Final Measurement (t=80 minutes):* Shape recording (SL), Reflectivity measurement (MSI), cDIC final pair of images recording

For each modality data the recording and processing protocols, along with data merging, as described in Ch. 4 and shown for the individual modalities in Ch. 5 are utilized.

6.1.3 Results

Shape Measurement

The shape of the object was recorded at the initial and final stages of the experiment (Fig. 6.2). It can be noted that the areas corresponding to patches A4 and A1 show minimal shape change, unlike B4 where visible shape change is detected. The maximum shape change is located at the bottom right of the sample corresponding to the area of patches B2 and B3, as well as around patch A5. Overall, most visible changes are detected around the bottom left area of the sample. To better visualize and quantify the changes in the 3D shape between the two time instances the M3C2 distance between the two clouds of points was calculated (Fig. 6.2c).

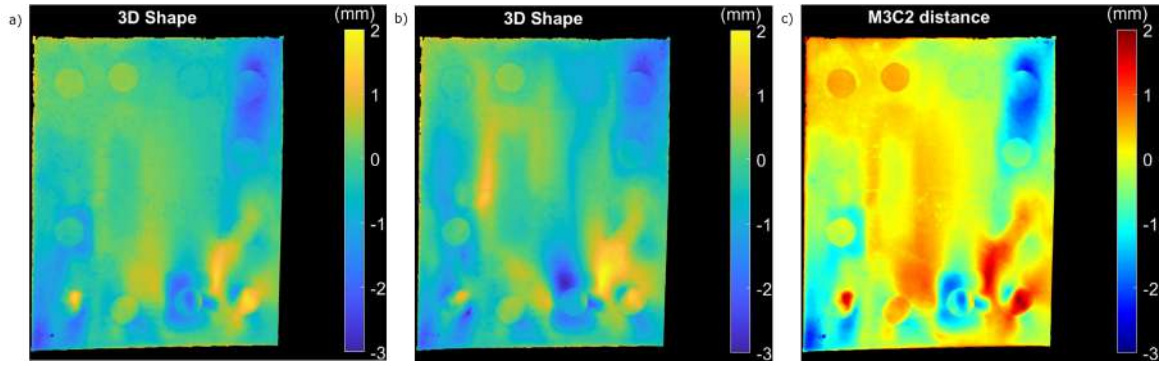

Figure 6.2: 3D Shape of the object at the a) initial state (t=0 min) and b) final state (t=80 mins), along with the c) M3C2 distance calculation between the two conditions.

The M3C2 distance, confirms the initial observations regarding the change in the shape, while it also reveals change in the areas located around A2 and A3 patches. Minimal change is detected for parches A1 and A4 (among best methods according to conservators), while maximum is observed for A5, B2, B3, B5. Overall the patches without the additional layer behave the worst, and present more change to their shape. Among the two investigated fabric type, the synthetic one presents the smaller shape changes, in line to what would be expected. In order to further asses the effect of the patching method to the object, the calculation of the strains and displacements using the cDIC modality is required. This will reveal if the shape change is the result of the natural fluctuation of the object, which poses no threat towards the object's condition, or whether it creates high strain values that can compromise the structural stability of the painting.

Reflectivity

The reflectivity measurements are performed at the beginning and the end of the experiment, but the object does not change in terms of spectral content within the conditions of the measurement. Therefore, only one time instance will be presented herein, as repeating them will not give further insights regarding the structural condition of the painting. Nevertheless, the reflectivity data can serve for documentation purposes, or as a reference in the case that the object is subjected to extreme conditions. The recorded data after FF and DC correction that correspond to the spectral bands of the MSI modality of MIS are shown in Fig. 6.3.

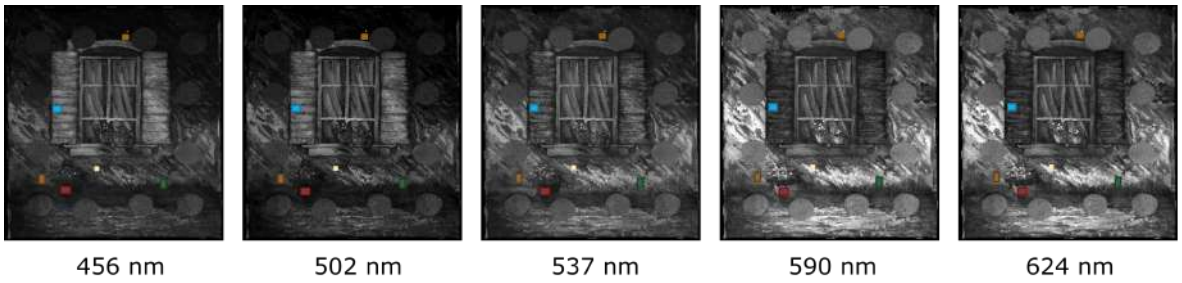

Figure 6.3: Spectral bands recorded using the MSI modality of MID, with colour the areas selected for further analysis are noted.

Following the same methodology described in previous chapters, six areas of the object were selected and SR was performed. The areas selected are representing distinct colours of the object as shown in Fig. 6.4. The recorded spectra is in line with the colour of the selected area.

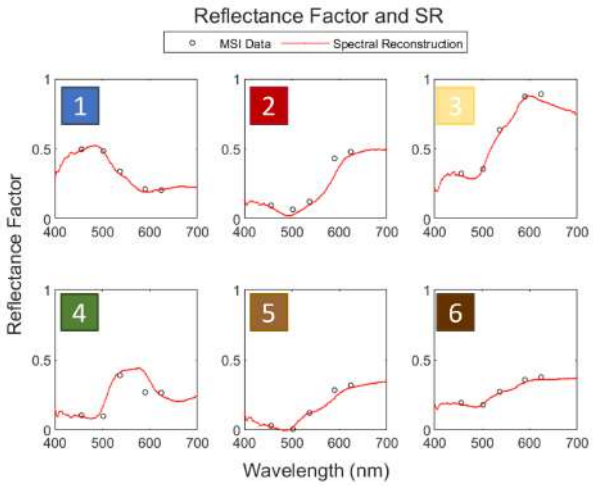

Figure 6.4: Reflectance factor and SR for the selected areas of the object.

Displacements and Strains

The results of 3D cDIC measurements are presented in this section. These results, along with the shape measurement, will provide insights regarding the structural condition of the object, specifically focusing on the development of strains and displacements and strains induced by the patches realized with different conservation methods. The cDIC methodology applied has been described in Ch. 4.1.2, the demosaicking method used herein is APN.

The displacements and strains shown in Fig. 6.5 are calculated with respect to the initial measurement (at t=0 min) and correspond to the final measurement (t=80 mins). In order to evaluate the conservation methods used for the patches we need to investigate the combined effect of displacements and strains. Canvas, is a hygroscopic material which can naturally fluctuate depending of the environmental conditions. Therefore, our interest is focused on the displacements that induce the highest strains magnitude (tensile or compressing), as they can indicate the patches that will eventually compromise the structural health of the object in the long term. From the global maps, it can be observed that the lowest out of plane displacement is detected around the area of patches A3 and A4, while highest for patches A5, B5 and B3. The in plane displacement maps show linear trends, due to the symmetrical effect of the stretcher, with local inhomogeneities especially located around patches (i.e. B3 and B5) which can be attributed to the effect of the patching method. Especially for the patch B3, which is done using the wax-resin method, the displacements can be attributed to the hardening of the material which subsequently affects the surrounding area. Overall, lower displacement values are detected for the synthetic patches, which is closer to the original support, in comparison to the linen ones. Additionally, the strain maps indicate strong alternating compressive and tensile ϵ_{yy}strains for the patches B3, B5 and B6. Strong non-linear strain terms are also detected for ϵ_{xx} and ϵ_{xy} around the same patches. For the synthetic type patches highest strains are detected around patch A2, while lowest for patch A4.

To further understand the displacement and strain development, cross sections were selected approximately, as shown in Fig. 6.6. The cross sections were selected in the middle of each patch, and their direction is parallel to the main directionality of the canvas. For the oversized patches and the ones covered with polyester fabric the cross section exceeds the limits of their total area.

In this way, the spatio temporal response of all the cross sections that correspond to the conservation patches can be investigated (Fig. 6.7). The scales used in the spatiotemporal

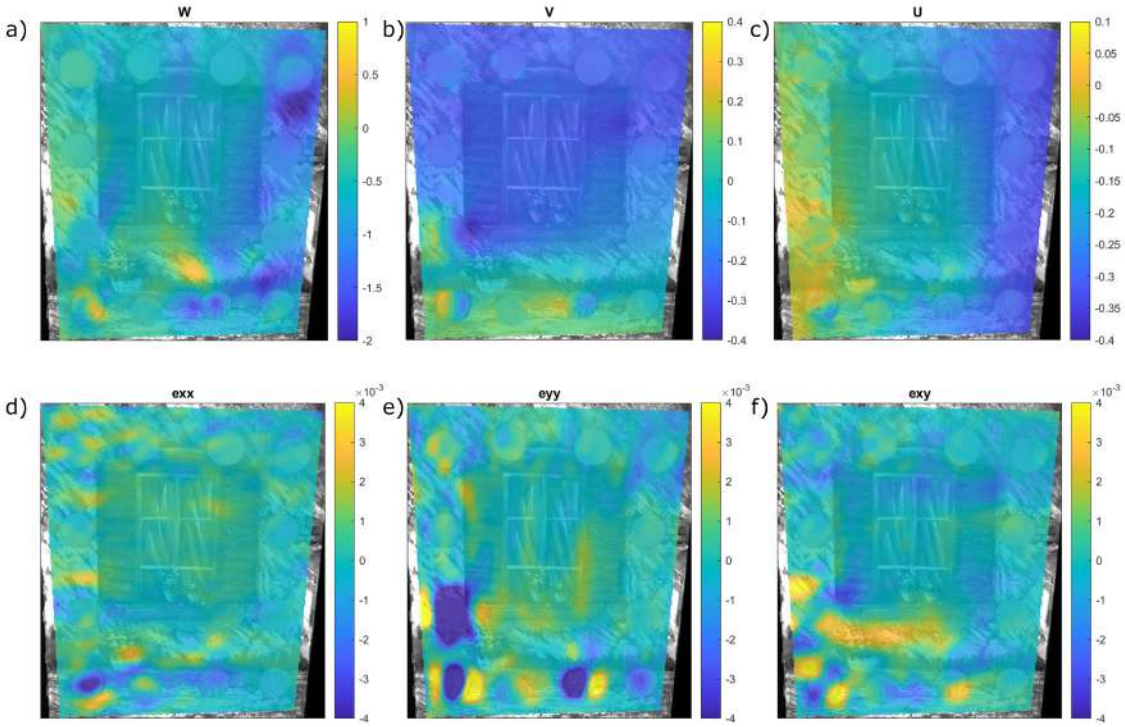

Figure 6.5: Final a-c) displacement maps and d-f) strain maps induced by the patches.

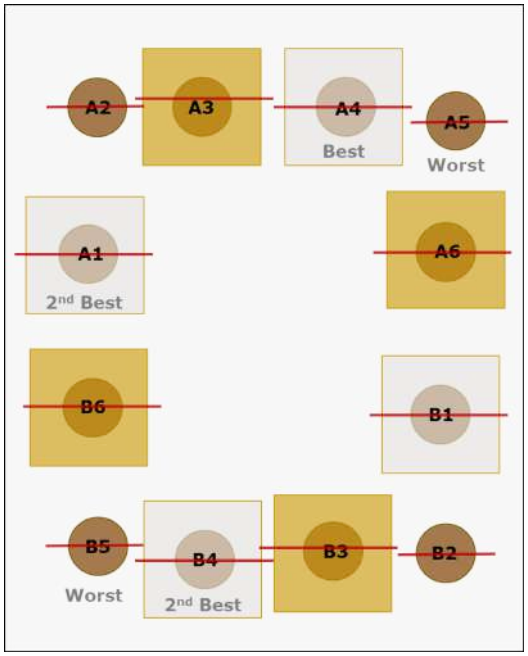

Figure 6.6: Schematic representation of the object along with the analysed cross sections.

maps vary depending on the analysed quantity (in specific W(-1.5 up to 0.5)mm, U(-0.4 up to 0)mm, V(-0.4 up to 0.2)mm, ε_{xx} $(-8 * 10^{-3}$ up to $8 * 10^{-3})$strains, ε_{yy} $(-0.025$ up to 0.02)strains, ε_{xy} up to $(-4 * 10^{-3}$ $4 * 10^{-3})$strains). Patches with type A textile yield the best overall results, with B presenting acceptable response only for patching technique number 1. The patches with the lowest strains, are in line with the conservators expectations for the

best method. Patches A1 and A4 both produce minimal strains with slightly less shear strain variations detected in A1. Unexpected results are recorded for patch B4, which despite being considered among the best methods, has significant displacements and strains. A possible explanation, can be it's proximity to patches B5 and B3, which are among the worst methods for filling the gaps in textile supports. It has to be noted that patch B5 was already partially detached at the beginning of the experiment and finalized with the complete detachment after the monitoring period of the experiment. In addition, patch B3 has induced significant modulations in large areas of the object detected at both the shape (Fig. 6.2) and displacements maps (Fig. 6.5), probably due to the wax-resin binder that makes the painting stiffer. Despite that, it did not present the highest recorded strains at the spatio temporal maps. B2 also exhibits similar behaviour, therefore it is also considered as a method to be avoided. In the case of A2 and A3, the edges of the patch can be clearly distinguished in the strain maps (red/orange vertical lines), contrary to patches A5 and A6 which induce lower strains. The patches with highest strains have high potential of detaching, while lower strains indicate higher potential for the patches to be stable and not detach in the future. Similar response, with higher magnitude is recorded also for patch B5. Overall worst results are detected for patches B2, B4 and B5. The displacements and strains analysis supports that the best patching methods corresponds to the synthetic fabric, and also confirm the expectations for the best and worst methods. Additionally, it quantifies the differences between the linen and synthetic patches and provides numerical data both locally and globally.

Conclusions

To summarize, a variety of patching methods have been tested with respect to their effectiveness towards the repair of defects in a synthetic canvas oil painting. Using the multimodal approach, by implementing the developed MIS, it was possible to monitor the response of the object both locally and globally during it's drying in the timespan of 80 minutes. The structural integrity of the painting is evaluated through the shape, displacements and strains, while the reflectivity serves for documentation purposes (along with shape). From these experiments, best results are achieved using synthetic patches, which is the same material as the original support woven closely to it in terms of density, along with patches either cut to size or slightly oversized supported by an additional layer of non- woven polyester fabric.

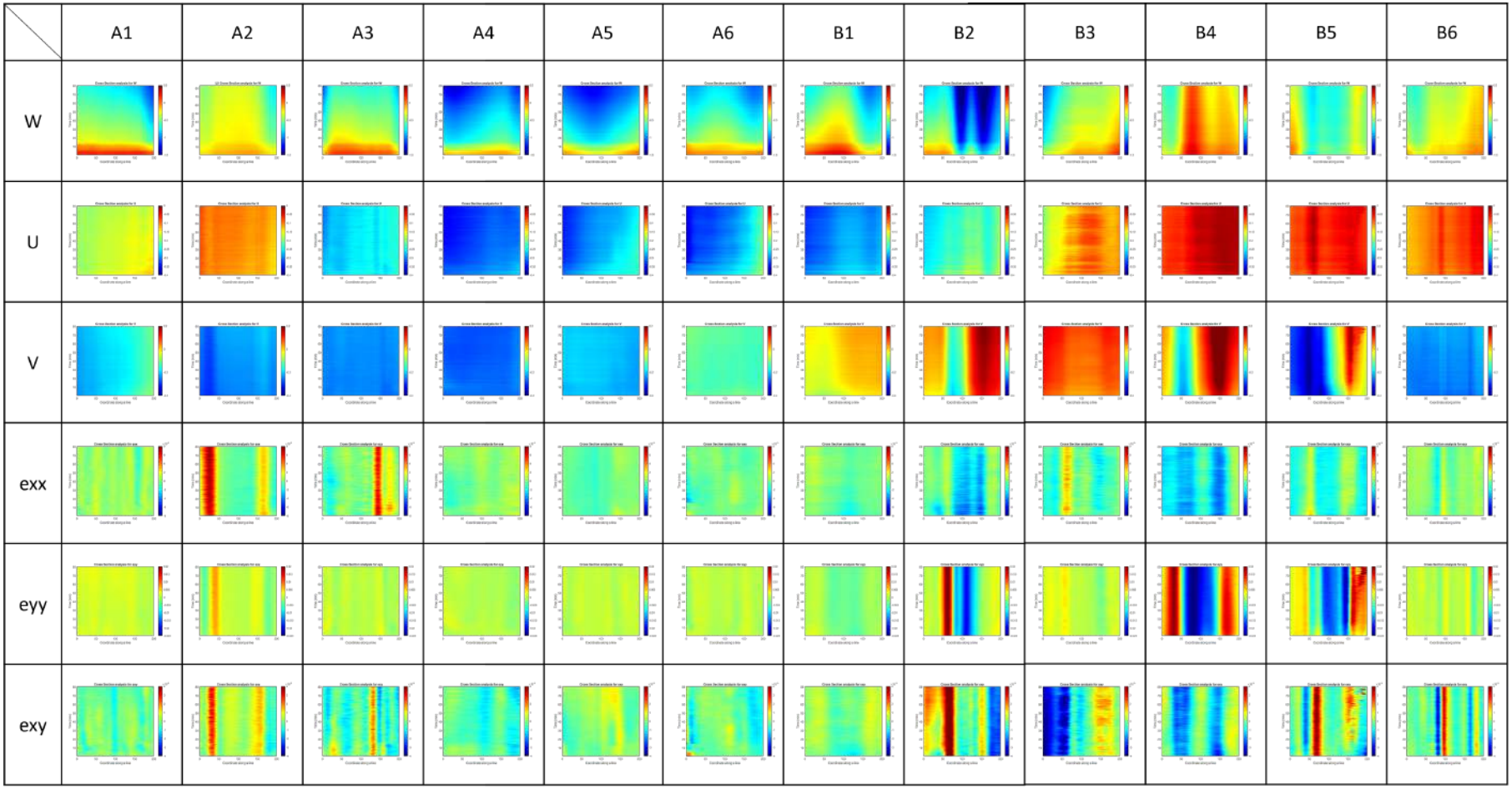

Figure 6.7: Spatiotemporal maps of the conservation patches. The scale bars correspond to W(-1.5 up to 0.5)mm, U(-0.4 up to 0)mm, V(-0.4 up to 0.2)mm, ε_{xx} $(-8 * 10^{-3}$ up to $8 * 10^{-3})$strains, ε_{yy} $(-0.025$ up to $0.02)$strains, ε_{xy} up to $(-4 * 10^{-3}$ $4 * 10^{-3})$strains

7

Conclusion and Final Remarks

The development of a portable multimodal system for surface measurement and monitoring of CH objects required considering various factors to achieve accurate and comprehensive results. This research task involved taking into account multiple surface attributes and exploiting high-resolution data for optimal results. The process includes the integration of different measurement techniques to capture diverse aspects of the objects under multiple scenarios. However, due to the intricate nature of CH objects and their preservation requirements, there is no one-size-fits-all solution for this complex task. However it was shown that the developed portable multimodal imaging system is a valuable tool which can support a variety of activities and cover several measurement needs articulated by conservation scientists and conservators.

7.1 Research Contributions

This researchs main contribution is the development of a multimodal quantitative imaging system for documenting actual state, evaluating, quantifying, and visualizing changes of

CHOs surfaces (shape, displacements, and spectral reflectance) caused by external conditions. The system presented is, to the best author's knowledge, the first instrumental offer which combines the three important imaging modalities, namely structured light, colour digital image correlation and multispectral imaging, into a single portable system capable of full-field measurement and monitoring of mid-sized CH object. Data capturing and processing pipelines have been developed for the involved modalities, which can be applied separately or combined including merging of the results into a single coordinate system. Two of the modalities, cDIC and MSI were significantly modified in order to meet the requirements related to CHOs (cDIC) and the portability and low cost of hardware (MSI). What is more, the special attention was paid to determination of metrological correctness of the results delivered by the novel implementation of cDIC and MSI as well as the combined modalities. Finally the system's functionality was checked through multiplicity of measurement and monitoring scenarios involving mock-ups of parchments and paintings as well as historical artefacts.

7.2 Fulfillment of the Objectives

The detailed research objectives formulated in Ch. 1.3 are repeated in this section, along with comments on their fulfillment.

Obj. 1: Development of portable multimodal imaging system

A prototype MIS capable of recording 3D shape, reflectivity, displacements and strains in a non contact and non invasive manner has been developed. It consists of two colour cameras and digital light projector only and therefore the demonstrator cost is very low (the hardware cost is below 10k euro), considering its multimodal functionality. The data generated are spatially and temporally coherent for every captured instance, while it is also possible to utilize each modality separately. Data processing paths have been developed for the successful merging of the data into a single coordinate system, by utilizing the pixel origin position of the recorded information. In this way, the SL, cDIC and MSI datasets are saved into a Matlab structure that contains matrices with the shape, displacement, strains, and spectral reflectivity information of the object. Finally, the accuracy of the developed modalities has been retrieved through the measurement of standard and well known targets.

Obj. 2: Modification of 3D DIC method to assure measurement of objects with natural texture and its metrological assessment

A modified 3D colour digital image correlation method (3D cDIC) was proposed for efficient displacement measurements of colour objects with natural texture. The method is using a separate analysis of correlation coefficient (sigma) value in the RGB channels of CCD cameras by utilizing local information from the channel with the minimum sigma. In this way, merged U,V,W displacement maps are generated based on the local correlation quality. Such approach allows to extend the range of objects with natural texture which fulfill DIC requirements and can be analysed with cDIC. The proposed method applies for colour filter array cameras, so the images in RGB channels have to undergo demosaicking procedure which directly influences the accuracy of displacement measurements. Several demosaicking methods were tested in order to identify the best performing one. Among the tested methods the best results were retrieved using APN method. To the author's best knowledge, this is the first time that the influence of demosaicking procedures (including the deep learning based demosaicking method) is studied in reference to the resultant accuracy of displacements for samples with natural texture. The novel processing method combined with APN demosaicking leads to increased accuracy of determined displacements and strains, in comparison to the commonly used cDIC approaches. The metrological comparison of the results obtained by unmodified and modified 3D cDIC processing was presented for a colour mock-up and canvas paintings exposed to in plane and out of plane displacements.

Obj. 3: Development of simplified measurement method of CHOs' spectral reflectance in MIS

The simple hardware configuration of the proposed MIS influenced the development of the MS imaging approach. The modality incorporates reflectance for five spectral bands within the visible range of the spectrum determined through a combination of the camera sensitivity functions and the spectral power distribution (SPD) of the digital projector. In the proposed solution the CFA of the camera substitutes the bandpass filter that would be typically met in an multispectral camera setup. Merging it with the narrow SPD of the LEDs results into surface

reflectance of well defined spectral bands. This solution was confirmed metrologically through comparing reflectance data recorded using the MSI modality of the MIS and HSI data. What is important, this simple, but innovative solution allows for spatiotemporal comparison of an object reflectance for well defined spectral bands.

Obj. 4: Measurement and monitoring of Cultural Heritage Objects

For the fulfilment of the last objective, measurement and monitoring sessions have been carried out with the individual modalities of mock-ups and real objects. In specific, the SL modality has been successfully implemented for the detection of change in the shape of a globe before and after conservation treatment, as well as, on a painting under the influence of environmental conditions. 3D DIC has been utilized for the monitoring of mock-up parchments under varying humidity and the evaluation of the utilized mounting system. The innovative measurement protocol implemented inside a climatic chamber allow for the first time to confirm the high functionality of a parchment mounting with elastic stripes and gain extensive knowledge about parchments behaviour exposed to changes of relative humidity [99]. A historical parchment sample had been also studied using 3D cDIC and it's response to small relative humidity changes has been investigated. The MSI modality had been utilized for reflectivity measurements on paintings and the results were compared with commercial MSI and HSI systems. Finally, a proof of concept experiment has demonstrated the potentiality of the method into detecting changes of the object's reflectivity. Through the studies of mock-ups and CH artefacts performed with single modalities the author and co-operating conservation researchers gain extended knowledge about the usability of the methods for CHOs investigations. The novel measurement scenarios were developed and novel ways of analyzing and presenting the results were proposed. Among them one of the most impressive and useful was the spatiotemporal imaging of changes (in shape, displacements, strains) in a selected crossection. All these experiences gained with single modalities was used during the final functional tests of the MIS involving all modalities. The measurements and monitoring of an oil painting with several intentional repairs were conducted. In this case, for the first time it was shown that several conservation

methods may be in detailed evaluated with respect to their effect on the sample's structural integrity. Additionally, the information recorded served for future reference and documentation purposes. The multimodal measurements sessions had been also performed for the mounted historical parchment [Papanikolaou et.al. accepted in Archiving, IS&T, 2023], proving in quantitative way its positive influence on the structural health of the CHO.

7.3 Achievements

The articles presenting the achievements reached during realization of this doctoral thesis that have been published or submitted for publication are listed below:

Journal Articles:

1. L. Małkowska, S. Saha, **A. Papanikolaou**, and D. Dzik-Kruszelnicka, How to cope with a globe: conservation and restoration of a deformed globe, Journal of Paper Conservation, pp. 1 – 12,2023

2. **A. Papanikolaou**, P. Garbat, and M. Kujawinska, Metrological evaluation of the demosaicking effect on colour digital image correlation with application in monitoring of paintings, Sensors, vol. 22, no. 19, 2022

3. **A. Papanikolaou**, D. Dzik-Kruszelnicka, and M. Kujawinska, Spatio-temporal monitoring of humidity induced 3d displacements and strains in mounted and unmounted parchments, Heritage Science, vol. 10, no. 1, pp. 125, 2022

Book Chapter:

1. **A. Papanikolaou**, D. Dzik-Kruszelnicka, P. Garbat, and M. Kujawinska, Parchment and 3d digital image correlation for spatio-temporal monitoring, Chapter under review in the CHANGE projects Final Book: Cultural Heritage Analysis for New GEnerations (CHANGE)

Articles in Conference Proceedings:

1. **A. Papanikolaou**, S. George, A. S. Suneel, G. Trumpy, and M. Kujawinska, Multimodal measurement of parchment using a custom 3D scanner, pp. 711, Society for Imaging Science and Technology (IS&T), 2023

2. A. Siatou, **A. Papanikolaou**, and E. Saiti, Adaption of imaging techniques for monitoring cultural heritage objects, in Advanced Nondestructive and Structural Techniques for Diagnosis, Redesign and Health Monitoring for the Preservation of Cultural Heritage (A. Osman and A. Moropoulou, eds.), pp. 3847, Springer International Publishing, 2022

3. **A. Papanikolaou**, P. Garbat, and M. Kujawinska, Colour digital image correlation method for monitoring of cultural heritage objects with natural texture, in Optics for Arts, Architecture, and Archaeology VIII (H. Liang and R. Groves, eds.), vol. 11784, pp. 166177, International Society for Optics and Photonics, SPIE, 2021

4. **A. Papanikolaou**, D. Dzik-Kruszelnicka, S. Saha, and M. Kujawinska, 3d digital image correlation system for monitoring of changes induced by RH fluctuations on parchment, Electronic Imaging, vol. 2021, no. 18, pp. 651657, 2021

5. S. Saha, A. Duda-Maczuga, **A. Papanikolaou**, and R. Sitnik, Approach for identification of geometry change on cultural heritage surface, Electronic Imaging, vol. 2021, no. 18, pp. 641647, 2021

6. S. Saha, **A. Papanikolaou**, J. Martusewicz, and R. Sitnik, Augmented reality in tracking the surface geometry change of cultural heritage objects, in 2020 International Conference on Computational Performance Evaluation (ComPE), pp. 537542, 2020

7.4 Future Perspectives

The multimodal imaging system for measurements and monitoring of CHOs had been developed and several useful measurement scenarios were proposed and implemented. However still not all problems have been solved or can be improved. In this section, the emphasis is put on describing the future direction of the multimodal imaging methods and system improvements and developments. Further improvement of the actual MIS:

- Improve the SL modality by implementing the gray code phase shifting method in the stereosystem. This will further improve the accuracy of the shape calculations and minimize the recorded data size.

- Unify the SL and DIC calibration, by incorporating open source DIC solutions. Current solutions have limitations with respect to their data load, which can be lifted by upgrade the source code and adapting it to better handle big data loads. This can also allow the total unification of the calibration between SL and 3D DIC, as the source code of both can be switched to be compatible for the same target. Therefore allowing for a single calibration session to be utilized in both modalities.

- Work towards the development of a GUI based software which will include data capturing and processing. Part of the analysing tasks and methods described in this thesis, can be standardized and incorporated as well. Working in this direction will enable personnel without extensive technical training to utilize the system. Implementation of new approaches:

- Incorporate higher complexity spectral reconstruction methodologies, such as models based on CNNs, which can enable more accurate reconstruction of the spectrum. An alternative, would be to upgrade the hardware and exchange the white light LED's with tunable wavelength sources for the acquisition of more spectral bands.

- Incorporate BRDF to the data processing pipeline, using the white LED data recorded sequentially and simultaneously to create a 3 angle model, with the aim to record the appearance of the object with good accuracy.

- Support an user with automated multimodal change detection method based on segmentation of the surface information [33]. This would allow the user to automatically evaluate the changes happening to the object without the need for specialized knowledge of post processing methods.

List of Figures

List of Tables

List of Abbreviations

The following abbreviations are used in this document:

AHD ..... Adaptive Homogeneity- Directed

AHD ..... Adaptive Homogeneity- Directed

AoI ..... Area of Interest

APN ..... Attention Pyramid Network

BRDF ..... Bidirectional Reflectance Distribution Function

C2C ..... Cloud to Cloud

cDIC ..... colour Digital Image Correlation

CFA ..... Colour Filter Array

CH ..... Cultural Heritage

CHO(s) ..... Cultural Heritage Object(s)

CoP ..... Cloud of Points

CP ..... Cardboard Panel

DC ..... Dark Current

DIC ..... Digital Image Correlation

DLP ..... Digital Light Processing

E_{MPE} ..... Estimated Maximum Permissible Error

EA ..... Edge Aware

ES ..... Elastic Stripes

FF ..... Flat Field

FoV ..... Field of View

HP ..... Hybrid Projection

HS(I) ..... Hyperspectral (Imaging)

ICA ..... Independent Component Analysis

ICP ..... Iterative Closest Points

ILM(s) ..... Incoherent Light method(s)

LT ..... Laser Triangulation

MIS ..... Multimodal Imaging System

MS(I) ..... Multispectral (Imaging)

NDT ..... Non Destructive Testing

P/V ..... Peak to Valley

PCA ..... Principal Components Analysis

PMS ..... Portable Measurement System

RMSE ..... Root Mean Square Error

SfM ..... Structure from Motion

SL ..... Structured Light

SPD ..... Spectral Power Distribution

SR ..... Spectral Reconstruction

sSL ..... stereo Structured Light

ToF ..... Time of Flight

VNIR ..... Visible Near Infrared

VNG ..... Variable Number of Gradients

ZNSSD ..... Zero Normalised Sum of Squared Differences

ZTRM ..... Division of Virtual Reality Technologies

Bibliography

[1] M. Moore, "Conservation Documentation and the Implications of Digitisation," *Journal of Conservation and Museum Studies*, Nov 2001.

[2] A. Bentkowska-Kafel and L. Macdonald, *Digital Techniques for Documenting and Preserving Cultural Heritage*. Arc Humanities Press, 2017.

[3] L. MacDonald, *Digital heritage: Applying Digital Imaging to Cultural Heritage*. Routledge, 2006.

[4] M. Santana Quintero, R. Eppich, M. Silver, A. Osello, F. Rinaudo, E. Verhoeven, Geertand Stylianidis, A. Georgopoulos, F. Remondino, P. Grussenmeyer, T. Landes, M. Doneus, and J. L. Lerma, *3D Recording, Documentation and Management of Cultural Heritage*. Whittles Publishing, 2017.

[5] K. Kosma, M. Andrianakis, and V. Tornari, "Laser-based, non-invasive monitoring and exponential analysis of the mechanical behaviour of materials with structural inhomogeneities in heat transfer, towards thermal equilibrium," *Applied Physics A*, vol. 128, no. 10, pp. 1–16, 2022.

[6] J. Auber-Le Saux, V. Detalle, X. Bai, M. Andrianakis, N. Wilkie-Chancellier, and V. Tornari, "Surface displacement measurements of artworks: New data processing for speckle pattern interferometry," *Applied Sciences*, vol. 12, no. 23, 2022.

[7] C. Seco-Martorell, V. Lopez-Dominguez, G. Arauz-Garofalo, A. Redo-Sanchez, J. Palacios, and J. Tejada, "Goya's artwork imaging with terahertz waves," *Opt. Express*, vol. 21, pp. 17800–17805, Jul 2013.

[8] P. Targowski, M. Kowalska, M. Sylwestrzak, and M. Iwanicka, *OCT for Examination of Cultural Heritage Objects*. Rijeka: IntechOpen, 2020.

[9] H. Liang, M. G. Cid, R. G. Cucu, G. M. Dobre, A. G. Podoleanu, J. Pedro, and D. Saunders, "En-face optical coherence tomography - a novel application of non-invasive imaging to art conservation," *Opt. Express*, vol. 13, pp. 6133–6144, Aug 2005.

[10] P. Targowski, M. Pronobis-Gajdzis, A. Surmak, M. Iwanicka, E. A. Kaszewska, and M. Sylwestrzak, "The application of macro-x-ray fluorescence and optical coherence tomography for examination of parchment manuscripts," *Studies in Conservation*, vol. 60, no. sup1, pp. S167–S177, 2015.

[11] S. Paoloni, F. Mercuri, N. Orazi, G. Caruso, and U. Zammit, "Photothermal approach for cultural heritage research," *Journal of Applied Physics*, vol. 128, p. 180904, 11 2020.

[12] A. D. Fovo, G. J. Tserevelakis, A. Papanikolaou, G. Zacharakis, and R. Fontana, "Combined photoacoustic imaging to delineate the internal structure of paintings," *Opt. Lett.*, vol. 44, pp. 919–922, Feb 2019.

[13] G. J. Tserevelakis, P. Siozos, A. Papanikolaou, K. Melessanaki, and G. Zacharakis, "Non-invasive photoacoustic detection of hidden underdrawings in paintings using air-coupled transducers," *Ultrasonics*, vol. 98, pp. 94–98, 2019.

[14] S. Ceccarelli, M. Guarneri, M. Ferri de Collibus, M. Francucci, M. Ciaffi, and A. Danielis, "Laser scanners for high-quality 3d and ir imaging in cultural heritage monitoring and documentation," *Journal of Imaging*, vol. 4, no. 11, 2018.

[15] V. Barrile, A. Nunnari, and R. C. Ponterio, "Laser Scanner for the Architectural and Cultural Heritage and Applications for the Dissemination of the 3D Model," *Procedia - Social and Behavioral Sciences*, vol. 223, pp. 555–560, 2016. 2nd International Symposium "New Metropolitan Perspectives" - Strategic planning, spatial planning, economic programs and decision support tools, through the implementation of Horizon/Europe2020. ISTH2020, Reggio Calabria (Italy), 18-20 May 2016.

[16] C. Fotakis, D. Anglos, V. Zafiropulos, S. Georgiou, and V. Tornari, *Lasers in the Preservation of Cultural Heritage: Principles and Applications*. Taylor and Francis, New York, 2007.

[17] Verhoeven, Geert, "Basics of photography for cultural heritage imaging," in *3D recording, documentation and management of cultural heritage* (Stylianidis, Efstratios and Remondino, Fabio, ed.), pp. 127–251, Whittles Publishing, 2016.

[18] M. Picollo, C. Cucci, A. Casini, and L. Stefani, "Hyper-spectral imaging technique in the cultural heritage field: New possible scenarios," *Sensors*, vol. 20, no. 10, 2020.

[19] H. Liang, "Advances in multispectral and hyperspectral imaging for archaeology and art conservation," *Applied Physics A*, vol. 106, pp. 309–323, 2012.

[20] H. Yilmaz, M. Yakar, S. Gulec, and O. Dulgerler, "Importance of digital close-range photogrammetry in documentation of cultural heritage," *Journal of Cultural Heritage*, vol. 8, no. 4, pp. 428–433, 2007.

[21] N. Yastikli, "Documentation of cultural heritage using digital photogrammetry and laser scanning," *Journal of Cultural Heritage*, vol. 8, no. 4, pp. 423–427, 2007.

[22] J. McCarthy, "Multi-image photogrammetry as a practical tool for cultural heritage survey and community engagement," *Journal of Archaeological Science*, vol. 43, pp. 175–185, 2014.

[23] C. Rocchini, P. Cignoni, C. Montani, P. Pingi, and R. Scopigno, "A low cost 3D scanner based on structured light," *Computer Graphics Forum*, vol. 20, no. 3, pp. 299–308, 2001.

[24] G. Bianco, F. Bruno, A. Tonazzini, E. Salerno, P. Savino, B. Zitova, F. Sroubek, and E. Console, "A Framework for Virtual Restoration of Ancient Documents by Combination of Multispectral and 3D Imaging," in *Eurographics Italian Chapter Conference 2010* (E. Puppo, A. Brogni, and L. D. Floriani, eds.), The Eurographics Association, 2010.

[25] J. Montusiewicz, M. Miłosz, J. Kęsik, and K. Żyła, "Structured-light 3D scanning of exhibited historical clothinga first-ever methodical trial and its results," *Heritage Science*, vol. 9, 2021.

[26] A. Kantaros, T. Ganetsos, and F. I. T. Petrescu, "Three-Dimensional printing and 3D Scanning: Emerging Technologies Exhibiting High Potential in the Field of Cultural Heritage," *Applied Sciences*, vol. 13, no. 8, 2023.

[27] J. Taylor, G. Forester, F. Livingstone, and R. Baribeau, "AMUSE: 3D Colour Imaging, Remote Access and Display," *Electronic Imaging and the Visual Arts, EVA*, vol. 96, pp. 9–1, 1996.

[28] A. Giachetti, I. M. Ciortan, C. Daffara, R. Pintus, and E. Gobbetti, "Multispectral RTI Analysis of Heterogeneous Artworks," in *Eurographics Workshop on Graphics and Cultural Heritage* (T. Schreck, T. Weyrich, R. Sablatnig, and B. Stular, eds.), The Eurographics Association, 2017.

[29] M. I. Ciortan, G. T. Dulecha, A. Giachetti, R. Pintus, A. Jaspe-Villanueva, and E. Gobbetti, "Artworks in the spotlight: characterization with a multispectral LED dome," *IOP Conference Series: Materials Science and Engineering*, vol. 364, p. 012025, jun 2018.

[30] T. Nöll, J. Köhler, G. Reis, and D. Stricker, "Fully automatic, omnidirectional acquisition of geometry and appearance in the context of cultural heritage preservation," *Journal on Computing and Cultural Heritage (JOCCH)*, vol. 8, no. 1, pp. 1–28, 2015.

[31] M. Malesa and et al, "Application of digital image correlation for tracking deformations of paintings on canvas," in *O3A: Optics for Arts, Architecture, and Archaeology III* (L. Pezzati and R. Salimbeni, eds.), vol. 8084, pp. 157 – 164, International Society for Optics and Photonics, SPIE, 2011.

[32] G. Leucci, *Nondestructive Testing Technologies for Cultural Heritage: Overview: A Practical Guide and New Perspectives*, pp. 15–73. Springer, 01 2019.

[33] S. Saha, *Automated Identification of Changes from Cultural Heritage Surfaces*. PhD thesis, Warsaw University of Technology, 2023.

[34] E. Saiti, *Deep Learning based frameworks for 3D registration of differential and multimodal data*. PhD thesis, Norwegian University of Science and Technology, 2023.

[35] A. Pamart, R. Roussel, E. Hubert, A. Colombini, R. Saleri, E. M. Mouaddib, Y. Castro, G. Le Goïc, and A. Mansouri, "A semantically enriched multimodal imaging approach dedicated to conservation and restoration studies," in *9th Intl. Workshop 3D-ARCH "3D Virtual Reconstruction and Visualization of Complex Architectures"*, vol. XLVI-2/W1-2022 of *International Archives of the Photogrammetry, Remote Sensing and Spatial Information Sciences*, (Mantua, Italy), Mar. 2022.

[36] M. Hess, V. Petrovic, D. Meyer, D. Rissolo, and F. Kuester, "Fusion of multimodal three-dimensional data for comprehensive digital documentation of cultural heritage sites," in *2015 Digital Heritage*, vol. 2, pp. 595–602, 2015.

[37] A. Pamart, F. Morlet, L. De Luca, and P. Veron, "A robust and versatile pipeline for automatic photogrammetric-based registration of multimodal cultural heritage documentation," *Remote Sensing*, vol. 12, no. 12, 2020.

[38] F. Tombari and F. Remondino, "Feature-based automatic 3D registration for cultural heritage applications," in *Digital Heritage International Congress*, The Eurographics Association, 2013.

[39] R. Pierdicca, E. Frontoni, E. S. Malinverni, F. Colosi, and R. Orazi, "Virtual reconstruction of archaeological heritage using a combination of photogrammetric techniques: Huaca Arco Iris, Chan Chan, Peru," *Digital Applications in Archaeology and Cultural Heritage*, vol. 3, no. 3, pp. 80–90, 2016.

[40] M. M. Ramos and F. Remondino, "Data fusion in cultural heritage - a review," *The International Archives of the Photogrammetry, Remote Sensing and Spatial Information Sciences*, vol. XL-5/W7, pp. 359–363, 2015.

[41] M. A. Sutton, J.-J. Orteu, and H. W. Schreier, *Image correlation for shape, motion and deformation measurements : basic concepts, theory and applications*. Springer, 2009.

[42] Z. Zhang, "A flexible new technique for camera calibration," *IEEE Transactions on Pattern Analysis and Machine Intelligence*, vol. 22, no. 11, pp. 1330–1334, 2000.

[43] Y. Abdel-Aziz, H. Karara, and M. Hauck, "Direct linear transformation from comparator coordinates into object space coordinates in close-range photogrammetry*," *Photogrammetric Engineering & Remote Sensing*, vol. 81, no. 2, pp. 103–107, 2015.

[44] R. Tsai, "A versatile camera calibration technique for high-accuracy 3D machine vision metrology using off-the-shelf TV cameras and lenses," *IEEE Journal on Robotics and Automation*, vol. 3, no. 4, pp. 323–344, 1987.

[45] K. Herakleous and C. Poullis, "3DUNDERWORLD-SLS: An Open-Source Structured-Light Scanning System for Rapid Geometry Acquisition," *arXiv preprint arXiv:1406.6595*, 2014.

[46] S. Verykokou and C. Ioannidis, "An Overview on Image-Based and Scanner-Based 3D Modeling Technologies," *Sensors*, vol. 23, no. 2, 2023.

[47] T. Luhmann, S. Robson, S. Kyle, and J. Boehm, *Close-Range Photogrammetry and 3D Imaging*. Berlin, Boston: De Gruyter, 2020.

[48] I. Aicardi, F. Chiabrando, M. Andrea, and F. Noardo, "Recent trends in cultural heritage 3D survey: The photogrammetric computer vision approach," *Journal of Cultural Heritage*, vol. 32, pp. 257–266, 2018.

[49] M. von Ubel, "The best photogrammetry software of 2023." https://all3dp.com/1/best-photogrammetry-software/. Accessed: 2023-05-30.

[50] T. D. Lillotte, P. Bebernik, J. Keck, M. Bommer, D. Schröder, and K. G. Wagner, "Laser triangulation as a fast and reliable method for determining ribbon solid fraction; focus on accuracy, precision, and measurement time," *International Journal of Pharmaceutics*, vol. 610, p. 121241, 2021.

[51] P. Puerto, B. Estala, and A. Mendikute, "A study on the uncertainty of a laser triangulator considering system covariances," *Sensors*, vol. 20, no. 6, 2020.

[52] C. Bamji, J. Godbaz, M. Oh, S. Mehta, A. Payne, S. Ortiz, S. Nagaraja, T. Perry, and B. Thompson, "A Review of Indirect Time-of-Flight Technologies," *IEEE Transactions on Electron Devices*, vol. 69, no. 6, pp. 2779–2793, 2022.

[53] T. Hoegg, C. Baiz, and A. Kolb, "Online improvement of time-of-flight camera accuracy by automatic integration time adaption," in *2015 IEEE International Symposium on Signal Processing and Information Technology (ISSPIT)*, pp. 613–618, 2015.

[54] S. Zhang, "High-speed 3D shape measurement with structured light methods: A review," *Optics and Lasers in Engineering*, vol. 106, pp. 119–131, 2018.

[55] F. Boochs, A. Bentkowska-Kafel, C. Degrigny, M. Karaszewski, A. Karmacharya, Z. Kato, M. Picollo, R. Sitnik, A. Trémeau, D. Tsiafaki, and L. Tamas, "Colour and Space in Cultural Heritage: Key Questions in 3D Optical Documentation of Material Culture for Conservation, Study and Preservation," in *Digital Heritage. Progress in Cultural*

Heritage: Documentation, Preservation, and Protection (M. Ioannides, N. Magnenat-Thalmann, E. Fink, R. Žarnić, A.-Y. Yen, and E. Quak, eds.), (Cham), pp. 11–24, Springer International Publishing, 2014.

[56] E. Bunsch, R. Sitnik, E. Holowko, M. Karaszewski, K. Lech, and W. Zaluski, "In search for the perfect method of 3D documentation of cultural heritage," in *Electronic Media and Visual Arts* (A. Bienert, A. Börner, E. Emenlauer-Blömers, and J. Hemsley, eds.), pp. 66–75, 2016.

[57] J. Geng, "Structured-light 3D surface imaging: a tutorial," *Adv. Opt. Photon.*, vol. 3, pp. 128–160, Jun 2011.

[58] G. Gayton, M. Isa, and R. K. Leach, "Evaluating parametric uncertainty using non-linear regression in fringe projection," *Optics and Lasers in Engineering*, vol. 162, p. 107377, 2023.

[59] S. Zhang and S.-T. Yau, "High-resolution, real-time 3D absolute coordinate measurement based on a phase-shifting method," *Opt. Express*, vol. 14, pp. 2644–2649, Apr 2006.

[60] M. Schreiner, M. Strlič, R. Salimbeni, E. C. in the Field of Scientific, T. R. (Organization), and C. G. (Project), *Handbook of the Use of Lasers in Conservation and Conservation Science*. COST, 2008.

[61] N. Doulamis, A. Doulamis, C. Ioannidis, M. Klein, and M. Ioannides, *Modelling of Static and Moving Objects: Digitizing Tangible and Intangible Cultural Heritage*, pp. 567–589. Springer International Publishing, 2017.

[62] S. P. McPherron, T. Gernat, and J.-J. Hublin, "Structured light scanning for high-resolution documentation of in situ archaeological finds," *Journal of Archaeological Science*, vol. 36, no. 1, pp. 19–24, 2009.

[63] S. Saha, J. Martusewicz, N. L. W. Streeton, and R. Sitnik, "Segmentation of change in surface geometry analysis for cultural heritage applications," *Sensors*, vol. 21, no. 14, 2021.

[64] S. Barone, A. Paoli, and A. V. Razionale, "3D Reconstruction and Restoration Monitoring of Sculptural Artworks by a Multi-Sensor Framework," *Sensors*, vol. 12, no. 12, pp. 16785–16801, 2012.

[65] M. Rahrig and M. Torge, "3D Inspection Of The Restoration And Conservation Of Stained Glass Windows Using High Resolution Structured Light Scanning," *The International Archives of the Photogrammetry, Remote Sensing and Spatial Information Sciences*, vol. XLII-2/W15, pp. 965–972, 2019.

[66] R. Sitnik, K. Lech, E. Bunsch, and J. Michoski, "Monitoring surface degradation process by 3D structured light scanning," in *Optics for Arts, Architecture, and Archaeology VII* (H. Liang, R. Groves, and P. Targowski, eds.), vol. 11058, p. 1105811, International Society for Optics and Photonics, SPIE, 2019.

[67] S. Saha, A. Tomkowska, J. Martusewicz, and R. Sitnik, "Manufacturing of ceramic venus figurine replica from a mold by combining traditional and digital technologies," *Heritage Science*, vol. 11, 2023.

[68] M. Wachowiak, B. V. Karas, and R. Baltrusch, "Reconstruction of a Nineteenth Century Plaster Piece Mold and Recreation of a Casting," in *Computer Applications to Archaeology*, 2009.

[69] L. Malkowska, S. Saha, A. Papanikolaou, and D. Dzik Kruszelnicka, "How to cope with a globe: Conservation and restoration of a deformed globe," *Journal of Paper Conservation*, pp. 1–12, 2023.

[70] E. Bunsch, R. Sitnik, and J. Michonski, "Tracking the aging process by multiple 3D scans analysis," in *Human Vision and Electronic Imaging XVII* (B. E. Rogowitz, T. N. Pappas, and H. de Ridder, eds.), vol. 8291, p. 82911G, International Society for Optics and Photonics, SPIE, 2012.

[71] L. Song, X. Li, Y.-g. Yang, X. Zhu, Q. Guo, and H. Liu, "Structured-Light Based 3D Reconstruction System for Cultural Relic Packaging," *Sensors*, vol. 18, no. 9, 2018.

[72] C. Kiourt, A. Koutsoudis, F. Arnaoutoglou, G. Petsa, S. Markantonatou, and G. Pavlidis, "A dynamic web-based 3D virtual museum framework based on open data," in *2015 Digital Heritage*, vol. 2, pp. 647–650, 2015.

[73] D. A. Loaiza Carvajal, M. M. Morita, and G. M. Bilmes, "Virtual museums. Captured reality and 3D modeling," *Journal of Cultural Heritage*, vol. 45, pp. 234–239, 2020.

[74] C. Meier, I. S. Berriel, and F. P. Nava, "Creation of a Virtual Museum for the Dissemination of 3D Models of Historical Clothing," *Sustainability*, vol. 13, no. 22, 2021.

[75] M. Shehade and T. Stylianou-Lambert, "Virtual Reality in Museums: Exploring the Experiences of Museum Professionals," *Applied Sciences*, vol. 10, no. 11, 2020.

[76] V. Tornari, "Optical and digital holographic interferometry applied in art conservation structural diagnosis," *e-Preservation Science*, vol. 3, 01 2006.

[77] A. S. Kobayashi, *Handbook on Experimental Mechanics.* SEM, 1993.

[78] B. Pan, "Recent Progress in Digital Image Correlation," *Experimental Mechanics*, vol. 51, 2011.

[79] B. Pan and B. Wang, "Digital image correlation with enhanced accuracy and efficiency: A comparison of two subpixel registration algorithms," *Experimental Mechanics*, vol. 56, no. 8, p. 13951409, 2016.

[80] B. Pan, H. Xie, and Z. Wang, "Equivalence of digital image correlation criteria for pattern matching," *Appl. Opt.*, vol. 49, pp. 5501–5509, Oct 2010.

[81] H. W. Schreier, J. R. Braasch, and M. A. Sutton, "Systematic errors in digital image correlation caused by intensity interpolation," *Optical Engineering*, vol. 39, no. 11, pp. 2915 – 2921, 2000.

[82] Y. Su, Q. Zhang, Z. Fang, Y. Wang, Y. Liu, and S. Wu, "Elimination of systematic error in digital image correlation caused by intensity interpolation by introducing position randomness to subset points," *Optics and Lasers in Engineering*, vol. 114, pp. 60–75, 2019.

[83] Z. Gao, Q. Zhang, Y. Su, and S. Wu, "Accuracy evaluation of optical distortion calibration by digital image correlation," *Optics and Lasers in Engineering*, vol. 98, pp. 143–152, 2017.

[84] T. Chu, W. F. Ranson, and M. Sutton, "Applications of digital-image-correlation techniques to experimental mechanics," *Experimental Mechanics*, vol. 25, pp. 232–244, 1985.

[85] *Vic-3D v7 Reference Manual*, Accessed: 2022-06-27.

[86] D. Solav and AsafSilver, "DuoDIC: 3D Digital Image Correlation in MATLAB," June 2022.

[87] D. Solav and A. Silverstein, "DuoDIC: 3D Digital Image Correlation in MATLAB," *Journal of Open Source Software*, vol. 7, no. 74, p. 4279, 2022.

[88] D. Turner, P. Crozier, and P. Reu, "Digital Image Correlation Engine, Version 00," 10 2015.

[89] J. Filho, L. Nunes, and J. Xavier, "iCorrVision-3D: An integrated python-based open-source Digital Image Correlation Software for in-plane and out-of-plane measurements (Part 2)," *SoftwareX*, vol. 19, p. 101132, 2022.

[90] A. Baldi, "Digital image correlation and color cameras," *Experimental Mechanics*, vol. 58, pp. 315 – 333, 2017.

[91] J. Curt, M. Capaldo, F. Hild, and S. Roux, "Optimal digital color image correlation," *Optics and Lasers in Engineering*, vol. 127, p. 105896, 2020.

[92] A. Papanikolaou, P. Garbat, and M. Kujawinska, "Metrological Evaluation of the Demosaicking Effect on Colour Digital Image Correlation with Application in Monitoring of Paintings," *Sensors*, vol. 22, no. 19, 2022.

[93] J. Stoffels, A. Ambosius, J. Bluekens, M. Peters, and P. Jacobus, "Color splitting prism assembly," April 1978,US patent 4084180.

[94] T. Slagle, R. Lyon, M. Ruda, and S. TW, "Color separation prism with adjustable path lengths," December 11 2001. US patent 6,330,113.

[95] B. Bayer, "Color imaging array," July 1976. US patent 3,971,065.

[96] A. Papanikolaou, P. Garbat, and M. Kujawinska, "Colour digital image correlation method for monitoring of cultural heritage objects with natural texture," in *Optics*

for Arts, Architecture, and Archaeology VIII (H. Liang and R. Groves, eds.), vol. 11784, pp. 166 – 177, International Society for Optics and Photonics, SPIE, 2021.

[97] A. Forsey and S. Gungor, "Demosaicing images from colour cameras for digital image correlation," *Optics and Lasers in Engineering*, vol. 86, pp. 20–28, 2016.

[98] A. Papanikolaou, D. Dzik-Kruszelnicka, S. Saha, and M. Kujawinska, "3D digital image correlation system for monitoring of changes induced by RH fluctuations on parchment," *Electronic Imaging*, vol. 2021, no. 18, pp. 65–1–65–7, 2021.

[99] A. Papanikolaou, D. Dzik-Kruszelnicka, and M. Kujawinska, "Spatio-temporal monitoring of humidity induced 3D displacements and strains in mounted and unmounted parchments," *Heritage Science*, vol. 10, no. 1, pp. 1–25, 2022.

[100] J. Alsayednoor, P. Harrison, M. Dobbie, R. Costantini, and F. Lennard, "Evaluating the use of digital image correlation for strain measurement in historic tapestries using representative deformation fields," *Strain*, vol. 55, no. 2, p. e12308, 2019. e12308 STRAIN-1433.R1.

[101] R. Costantini, F. Lennard, J. Alsayednoor, and P. Harrison, "Investigating mechanical damage mechanisms of tapestries displayed at different angles using 2d dic," *The European Physical Journal Plus*, vol. 135, no. 6, 2020.

[102] Z. Wang, J. Zhao, L. Fei, Y. Jin, and D. Zhao, "Deformation Monitoring System Based on 2D-DIC for Cultural Relics Protection in Museum Environment with Low and Varying Illumination," *Mathematical Problems in Engineering*, 2018.

[103] M. Kujawinska, M. Malesa, K. Malowany, A. Piekarczuk, L. Tyminska-Widmer, and P. Targowski, "Digital image correlation method: a versatile tool for engineering and art structures investigations," in *22nd Congress of the International Commission for Optics: Light for the Development of the World* (R. Rodríguez-Vera and et al, eds.), vol. 8011, pp. 2599 – 2606, SPIE, 2011.

[104] K. Malowany, L. Tymińska-Widmer, M. Malesa, M. Kujawińska, P. Targowski, and B. J. Rouba, "Application of 3d digital image correlation to track displacements and strains of canvas paintings exposed to relative humidity changes," *Appl. Opt.*, vol. 53, pp. 1739–1749, Mar 2014.

[105] F. Mugnai, G. Tucci, and A. Da Re, "Digital Image Correlation In Assessing Structured-Light 3D Scanners Gantry Stability: Performing Davids (Michelangelo) High-Accuracy 3D Survey," *The International Archives of the Photogrammetry, Remote Sensing and Spatial Information Sciences*, vol. XLVI-M-1-2021, pp. 463–469, 2021.

[106] C. Jones, C. Duffy, A. Gibson, and M. Terras, "Understanding multispectral imaging of cultural heritage: Determining best practice in msi analysis of historical artefacts," *Journal of Cultural Heritage*, vol. 45, pp. 339–350, 2020.

[107] E. Marengo, M. Manfredi, O. Zerbinati, E. Robotti, E. Mazzucco, F. Gosetti, G. Bearman, F. France, and P. Shor, "Development of a technique based on multi-spectral imaging for monitoring the conservation of cultural heritage objects," *Analytica Chimica Acta*, vol. 706, no. 2, pp. 229–237, 2011.

[108] H. Liang, "Advances in multispectral and hyperspectral imaging for archaeology and art conservation," *Applied Physics A*, vol. 106, pp. 309–323, 2012.

[109] R. Qureshi, M. Uzair, K. Khurshid, and H. Yan, "Hyperspectral document image processing: Applications, challenges and future prospects," *Pattern Recognition*, vol. 90, pp. 12–22, 2019.

[110] V. Papadakis, Y. Orphanos, S. Kogou, K. Melessanaki, P. Pouli, and C. Fotakis, "IRIS; a novel spectral imaging system for the analysis of Cultural Heritage objects," *Proceedings of SPIE - The International Society for Optical Engineering*, vol. 8084, p. 80840W, 2011.

[111] A. Zacharopoulos, K. Hatzigiannakis, P. Karamaoynas, V. M. Papadakis, M. Andrianakis, K. Melessanaki, and X. Zabulis, "A method for the registration of spectral images of paintings and its evaluation," *Journal of Cultural Heritage*, vol. 29, pp. 10–18, 2018.

[112] J. Yoon, "Hyperspectral imaging for clinical applications," *BioChip Journal*, vol. 16, 2022.

[113] H. Li, G. Li, Y. Ye, and L. Lin, "A high-efficiency acquisition method of led-multispectral images based on frequency-division modulation and rgb camera," *Optics Communications*, vol. 480, p. 126492, 2021.

[114] R. Shrestha and J. Y. Hardeberg, "Multispectral imaging using LED illumination and an RGB camera," in *Color Imaging Conference*, 2013.

[115] H. Liu, J. Sticklus, K. Köser, H.-J. T. Hoving, H. Song, Y. Chen, J. Greinert, and T. Schoening, "TuLUMIS - a tunable LED-based underwater multispectral imaging system," *Opt. Express*, vol. 26, pp. 7811–7828, Mar 2018.

[116] C. Daffara and R. Fontana, "Multispectral Infrared Reflectography to Differentiate Features in Paintings," *Microscopy and Microanalysis*, vol. 17, pp. 691–695, 04 2011.

[117] C. Balas, V. Papadakis, N. Papadakis, A. Papadakis, E. Vazgiouraki, and G. Themelis, "A novel hyper-spectral imaging apparatus for the non-destructive analysis of objects of artistic and historic value," *Journal of Cultural Heritage*, vol. 4, pp. 330–337, 2003. Lases in the Conservation of Artworks - LACONA IV.

[118] S. Baronti, A. Casini, F. Lotti, and S. Porcinai, "Multispectral imaging system for the mapping of pigments in works of art by use of principal-component analysis," *Appl. Opt.*, vol. 37, pp. 1299–1309, Mar 1998.

[119] A. Cosentino, "Panoramic, macro and micro multispectral imaging: An affordable system for mapping pigments on artworks," *Journal of Conservation and Museum Studies*, 2015.

[120] J. A. Toque, Y. Sakatoku, and A. Ide-Ektessabi, "Pigment identification by analytical imaging using multispectral images," in *2009 16th IEEE International Conference on Image Processing (ICIP)*, pp. 2861–2864, 2009.

[121] C. Cucci, J. K. Delaney, and M. Picollo, "Reflectance hyperspectral imaging for investigation of works of art: Old master paintings and illuminated manuscripts," *Accounts of Chemical Research*, vol. 49, no. 10, pp. 2070–2079, 2016. PMID: 27677864.

[122] A. Casini, F. Lotti, M. Picollo, L. Stefani, and E. Buzzegoli, "Image spectroscopy mapping technique for noninvasive analysis of paintings," *Studies in Conservation*, vol. 44, no. 1, pp. 39–48, 1999.

[123] K. Melessanaki, V. Papadakis, C. Balas, and D. Anglos, "Laser induced breakdown spectroscopy and hyper-spectral imaging analysis of pigments on an illuminated

manuscript," *Spectrochimica Acta Part B: Atomic Spectroscopy*, vol. 56, no. 12, pp. 2337–2346, 2001.

[124] E. Marengo, M. Manfredi, O. Zerbinati, E. Robotti, E. Mazzucco, F. Gosetti, G. Bearman, F. France, and P. Shor, "Technique Based on LED Multispectral Imaging and Multivariate Analysis for Monitoring the Conservation State of the Dead Sea Scrolls," *Analytical Chemistry*, vol. 83, no. 17, pp. 6609–6618, 2011.

[125] A. Giacometti, A. Campagnolo, L. W. MacDonald, S. Mahony, M. M. Terras, S. Robson, T. Weyrich, and A. P. Gibson, "Cultural heritage destruction: Documenting parchment degradation via multispectral imaging," in *EVA*, 2012.

[126] F. Daniel, A. Mounier, J. Pérez-Arantegui, C. Pardos, N. Prieto-Taboada, S. Fdez-Ortiz de Vallejuelo, and K. Castro, "Hyperspectral imaging applied to the analysis of Goya paintings in the Museum of Zaragoza (Spain)," *Microchemical Journal*, vol. 126, pp. 113–120, 2016.

[127] R. Easton, K. Knox, and W. Christens-Barry, "Multispectral imaging of the Archimedes palimpsest," in *32nd Applied Imagery Pattern Recognition Workshop, 2003. Proceedings.*, pp. 111–116, 2003.

[128] R. Hedjam and M. Cheriet, "Historical document image restoration using multispectral imaging system," *Pattern Recognition*, vol. 46, no. 8, pp. 2297–2312, 2013.

[129] A. Polak, T. Kelman, P. Murray, S. Marshall, D. J. Stothard, N. Eastaugh, and F. Eastaugh, "Hyperspectral imaging combined with data classification techniques as an aid for artwork authentication," *Journal of Cultural Heritage*, vol. 26, pp. 1–11, 2017.

[130] Z. Wang, D. Lu, D. Zhang, M. Sun, and Y. Zhou, "Fake modern Chinese painting identification based on spectral–spatial feature fusion on hyperspectral image," *Multidimensional Systems and Signal Processing*, vol. 27, no. 4, pp. 1031–1044, 2016.

[131] A. Walter, P. Paul-Gilloteaux, B. Plochberger, L. Sefc, P. Verkade, J. G. Mannheim, P. Slezak, A. Unterhuber, M. Marchetti-Deschmann, M. Ogris, K. Bühler, D. Fixler, S. H. Geyer, W. J. Weninger, M. Glösmann, S. Handschuh, and T. Wanek, "Correlated Multimodal Imaging in Life Sciences: Expanding the Biomedical Horizon," *Frontiers in Physics*, vol. 8, 2020.

[132] M. F. Shirazi, J. Andilla, N. Lefaudeux, C. Valdes, F. Schwarzhans, M. Durand, K. Ntatsis, D. A. De Jesus, L. Sanchez Brea, K. Gocho, *et al.*, "Multi-modal and multi-scale clinical retinal imaging system with pupil and retinal tracking," *Scientific Reports*, vol. 12, no. 1, pp. 1–12, 2022.

[133] F. Nadon, A. J. Valencia, and P. Payeur, "Multi-modal sensing and robotic manipulation of non-rigid objects: A survey," *Robotics*, vol. 7, no. 4, 2018.

[134] M. Perttunen, V. Kostakos, J. Riekki, and T. Ojala, "Urban traffic analysis through multi-modal sensing," *Personal and Ubiquitous Computing*, vol. 19, no. 3, pp. 709–721, 2015.

[135] H. Xu, Z. Yang, Z. Zhou, L. Shangguan, K. Yi, and Y. Liu, "Indoor localization via multi-modal sensing on smartphones," in *Proceedings of the 2016 ACM International Joint Conference on Pervasive and Ubiquitous Computing*, UbiComp '16, (New York, NY, USA), p. 208219, Association for Computing Machinery, 2016.

[136] K. W. Bowyer, K. Chang, and P. Flynn, "A survey of approaches and challenges in 3D and multi-modal 3D+2D face recognition," *Computer Vision and Image Understanding*, vol. 101, no. 1, pp. 1–15, 2006.

[137] J. Petrich, Z. Snow, D. Corbin, and E. W. Reutzel, "Multi-modal sensor fusion with machine learning for data-driven process monitoring for additive manufacturing," *Additive Manufacturing*, vol. 48, p. 102364, 2021.

[138] J. W. Andreasen, " MUltiscale, Multimodal and Multidimensional imaging for EngineeRING (MUMMERING)." Funding Period (Jan. 2018 - June 2022). Marie Skodowska-Curie Actions Project No. 765604.

[139] D. Tzovaras, " MUltiscale, Multimodal and Multidimensional imaging for EngineeRINGMultimodal Scanning of Cultural Heritage Assets for their multilayered digitization and preventive conservation via spatiotemporal 4D Reconstruction and 3D Printing (Scan4Reco)." Funding Period (Oct. 2015 - Sept. 2018). Europe In A Changing World - Inclusive, Innovative And Reflective Societies Project No. 665091.

[140] M. Hess, V. Petrovic, D. Meyer, D. Rissolo, and F. Kuester, "Fusion of multimodal three-dimensional data for comprehensive digital documentation of cultural heritage sites," in *2015 Digital Heritage*, vol. 2, pp. 595–602, 2015.

[141] L. W. MacDonald and J. Valach, "Application of multi-modal 2D and 3D imaging and analytical techniques to document and examine coins on the example of two Roman silver denarii," *Heritage Science*, vol. 6, no. 5, 2018.

[142] S. D. Santos, N. Poirot, and M. Brochard, "Ultrasound-based multimodal imaging for cultural heritage: Aging of the weathered Tuffeau stone," in *2016 15th Biennial Baltic Electronics Conference (BEC)*, pp. 147–150, 2016.

[143] J. K. Delaney, K. A. Dooley, R. Radpour, and I. Kakoulli, " Macroscale multimodal imaging reveals ancient painting production technology and the vogue in Greco-Roman Egypt," *Scientific Reports*, vol. 7, no. 1, 2017.

[144] C. L. K. Dandolo, M. Lopez, K. Fukunaga, Y. Ueno, R. Pillay, D. Giovannacci, Y. L. Du, X. Bai, M. Menu, and V. Detalle, "Toward a multimodal fusion of layered cultural object images: complementarity of optical coherence tomography and terahertz time-domain imaging in the heritage field," *Appl. Opt.*, vol. 58, pp. 1281–1290, Feb 2019.

[145] B. Fransen, F. Temmermans, and C. Currie, "Imaging techniques and methodologies for acquisition, processing and distribution of multimodal image data from the oeuvre of Jan van Eyck," in *Optics, Photonics and Digital Technologies for Imaging Applications VI* (P. Schelkens and T. Kozacki, eds.), vol. 11353, p. 113530C, International Society for Optics and Photonics, SPIE, 2020.

[146] E. Stylianidis, K. Evangelidis, R. Vital, P. Dafiotis, and S. Sylaiou, "3D Documentation and Visualization of Cultural Heritage Buildings through the Application of Geospatial Technologies," *Heritage*, vol. 5, pp. 2818–2832, 2022.

[147] K. Tonsho, Y. Akao, N. Tsumura, and Y. Miyake, "Development of goniophotometric imaging system for recording reflectance spectra of 3D objects," in *IS&T/SPIE Electronic Imaging*, 2001.

[148] A. Mansouri, A. Lathuiliere, F. S. Marzani, Y. Voisin, and P. Gouton, "Toward a 3D Multispectral Scanner: An Application to Multimedia," *IEEE MultiMedia*, vol. 14, p. 4047, jan 2007.

[149] R. Sitnik, J. F. Krzeslowski, and G. Maczkowski, "Archiving shape and appearance of cultural heritage objects using structured light projection and multispectral imaging," *Optical Engineering*, vol. 51, no. 2, p. 021115, 2012.

[150] L. Felipe-Sese, A. J. Molina-Viedma, E. Lopez-Alba, and F. A. Diaz, "RGB Colour Encoding Improvement for Three-Dimensional Shapes and Displacement Measurement Using the Integration of Fringe Projection and Digital Image Correlation," *Sensors*, vol. 18, no. 9, 2018.

[151] X. Zhang, C. Li, L. Yu, and B. Pan, "Heatwave distortion correction using an improved reference sample compensation method and multispectral digital image correlation," *Appl. Opt.*, vol. 60, pp. 3716–3723, May 2021.

[152] Y. Dong, J. Zhao, and B. Pan, "Ultraviolet 3D digital image correlation applied for deformation measurement in thermal testing with infrared quartz lamps," *Chinese Journal of Aeronautics*, vol. 33, no. 3, pp. 1085–1092, 2020.

[153] R. B. Berke and J. Lambros, "Ultraviolet digital image correlation (UV-DIC) for high temperature applications," *Review of Scientific Instruments*, vol. 85, no. 4, p. 045121, 2014.

[154] R. Sitnik, M. Kujawinska, and J. M. Woznicki, "Digital fringe projection system for large-volume 360-deg shape measurement," *Optical Engineering*, vol. 41, no. 2, pp. 443 – 449, 2002.

[155] J. Lenar, M. Witkowski, V. Carbone, S. Kolk, M. Adamczyk, R. Sitnik, M. van der Krogt, and N. Verdonschot, "Lower body kinematics evaluation based on a multidirectional four-dimensional structured light measurement," *Journal of Biomedical Optics*, vol. 18, no. 5, p. 056014, 2013.

[156] A. Marcin, S. Maciej, S. Robert, and W. Adam, "Hierarchical, Three-Dimensional Measurement System for Crime Scene Scanning," *Journal of Forensic Sciences*, vol. 62, no. 4, pp. 889–899, 2017.

[157] G. Bradski, "The OpenCV Library," *Dr. Dobb's Journal of Software Tools*, 2000.

[158] R. Ravanelli and A. Moreau, "Structured light tutorials." https://docs.opencv.org/4.x/d3/d81/tutorial_structured_light.html. Accessed: 2023-06-30.

[159] "Optical 3D measuring systems - Optical systems based on area scanning," standard, Verein Deutscher Ingenieure e.V., Düsseldorf, GE, August 2012.

[160] J. Li, X. Dan, W. Xu, Y. Wang, G. Yang, and L. Yang, "3D digital image correlation using single color camera pseudo-stereo system," *Optics & Laser Technology*, vol. 95, pp. 1–7, 2017.

[161] X. Li, B. Gunturk, and L. Zhang, "Image demosaicing: a systematic survey," in *Visual Communications and Image Processing 2008* (W. A. Pearlman, J. W. Woods, and L. Lu, eds.), vol. 6822, pp. 489 – 503, International Society for Optics and Photonics, SPIE, 2008.

[162] "Basler pixel format." https://docs.baslerweb.com/pixel-format.html?filter=Camera:acA4112-8gc, Accessed: 2022-06-21.

[163] "PGI Basler White Paper kernel description." https://www.baslerweb.com/en/downloads/document-downloads/pgi-feature-set/, Accessed: 2022-05-15.

[164] A. N. A. Rahim, S. N. Yaakob, R. Ngadiran, and M. W. Nasruddin, "An analysis of interpolation methods for super resolution images," in *2015 IEEE Student Conference on Research and Development (SCOReD)*, pp. 72–77, 2015.

[165] K. Hirakawa and T. W. Parks, "Adaptive homogeneity-directed demosaicing algorithm," *IEEE Transactions on Image Processing*, vol. 14, pp. 360–369, 2005.

[166] Y. Monno, D. Kiku, M. Tanaka, and M. Okutomi, "Adaptive Residual Interpolation for Color and Multispectral Image Demosaicking," *Sensors*, vol. 17, no. 12, 2017.

[167] "Libraw project," url: https://www.libraw.org/ , Accessed: 2022-06-30.

[168] Y. Mei, Y. Fan, Y. Zhang, J. Yu, Y. Zhou, D. Liu, Y. Fu, T. S. Huang, and H. Shi, "Pyramid Attention Networks for Image Restoration," *arXiv preprint, arXiv:2004.13824*, 2020.

[169] A. Sole, I. Farup, and S. Tominaga, "Image based reflectance measurement based on camera spectral sensitivities," *Electronic Imaging*, no. 9, pp. 1–8, 2016.

[170] R. Shrestha, A. Mansouri, and J. Y. Hardeberg, "Multispectral imaging using a stereo camera: concept, design and assessment," *EURASIP Journal on Advances in Signal Processing*, vol. 57, no. 1, 2011.

[171] "Specim iq technical specifications." https://www.specim.com/iq/tech-specs/. Accessed: 2023-08.

[172] A. J. Laub, *Matrix Analysis for Scientists and Engineers* . SIAM: Society for Industrial and Applied Mathematics, 2004.

[173] D. Lague, N. Brodu, and J. Leroux, "Accurate 3D comparison of complex topography with terrestrial laser scanner: Application to the Rangitikei canyon (N-Z)," *ISPRS Journal of Photogrammetry and Remote Sensing*, vol. 82, pp. 10–26, 2013.

[174] S. Saha and R. Sitnik, "Segmentation in application to deformation analysis of cultural heritage surfaces," in *Proc. IS&T Intl. Symp. on Electronic Imaging: 3D Imaging and Applications*, vol. 34, pp. 213–1–213–1, 2022.

[175] M. LLC, "Cloudcompare (version 2.13) [gpl software]. (2.12.4 kyiv (7/14/2022))."

[176] M. F. Mecklenburg, "Determining the acceptable ranges of relative humidity and temperature in museums and galleries: Part 1, structural response to relative humidity," guidelines, Smithsonian Museum Conservation Institute, Maryland, US, 2007.

[177] N. Duqueyroix, L. Robinet, and C. Barbe, "Expandable polyester hinges for parchment mounting performance in fluctuating environmental conditions," *Journal of Paper Conservation*, vol. 16, no. 1, pp. 18–28, 2015.

[178] B. Haines and L. C. Centre, *Parchment: The Physical and Chemical Characteristics of Parchment and the Materials Used in Its Conservation.* Leather Conservation Centre, 1999.

[179] W. Liszewska, *New Methods of Leafcasting in the Conservation of Historic Parchments.* Technologia - Sztuka - Konserwacja, Polski Instytut Studiów na Sztuką Świata, 2017.

[180] E. Badea, W. Vetter, I. Petroviciu, C. Carsote, L. Miu, M. Schreiner, and G. Della Gatta, "How parchment responds to temperature and relative humidity: a combined micro

DSC, MHT, SEM and ATR-FTIR study," in *Proceedings of the 4th International Conference on Advanced Materials and Systems, ICAMS 2012*, 09 2012.

[181] F. Grillini, J.-B. Thomas, and S. George, "Comparison of Imaging Models for Spectral Unmixing in Oil Painting," *Sensors*, vol. 21, no. 7, 2021.

[182] H. Deborah, S. George, and J. Y. Hardeberg, "Spectral-divergence based pigment discrimination and mapping: A case study on The Scream (1893) by Edvard Munch," *Journal of the American Institute for Conservation*, vol. 58, no. 1-2, pp. 90–107, 2019.

[183] "SpectroCam Multispectral Cameras." https://www.oceaninsight.com/globalassets/catalog-blocks-and-images/pdfs/spectrocam_product-sheet_new_final.pdf. Accessed: 2023-08.

[184] J. Schindelin, I. Arganda-Carreras, E. Frise, V. Kaynig, M. Longair, T. Pietzsch, S. Preibisch, C. Rueden, S. Saalfeld, B. Schmid, J.-Y. Tinevez, D. J. White, V. Hartenstein, K. Eliceiri, P. Tomancak, and A. Cardona, "Fiji: an open-source platform for biological-image analysis," *Nature Methods*, vol. 9, pp. 18–28, 2015.